FRACTURE TOUGHNESS STUDY ON BULK METALLIC GLASSES

AND

NOVEL JOINING METHOD USING BULK METALLIC GLASS SOLDER

Thesis by

Jin-Yoo Suh

In Partial Fulfillment of the Requirements

for the Degree of

Doctor of Philosophy

California Institute of Technology

Pasadena, California

2009

(Defended December 18, 2008)

Acknowledgements

God gives me more than I deserve.

I am so much grateful to Prof. William L. Johnson, my advisor, for his guidance and support. His passion and optimism are inspiring and his deep insight is enlightening.

It has been my great pleasure to work together and form friendship with the former and current members of the Johnson group. Prof. R. Dale Conner of California State University, Northridge has been a good friend and mentor since the beginning of my bumpy life in Caltech. Dr. Paul Kim provided materials for the fracture experiments on monolithic BMG's. He also gave me a lot of advices and encouragements. Dr. Marios D. Demetriou is a specialist of almost all research arenas of bulk metallic glasses. He helped me not only with many experimental skills, but also with invaluable ideas. Dr. Douglas C. Hoffman is my officemate. It has been my honor to work on the outstanding composites he invented, which are introduced in Chapter 5. I have enjoyed being his officemate. His hard work always makes a breakthrough. Prof. Boonrat Lohwongwatana is now a professor of the Chulalongkorn University in Thailand. He came up with the idea of the novel thermoplastic soldering process, which is the basis for the experimental works described in Chapter 6. Prof. Haein Choi-Yim of Sookmyung Woman's University in Korea influenced a lot for my graduate study. Dr. Mary Laura Lind did sound velocity measurement for me. She responded quickly with whatever questions I asked. Annelen Kahl kindly taught me how to measure sound velocity. Georg Kaltenboeck helped me make thin foils of metallic glasses using the splat quencher. Aaron Wiest is very smart and passionate. He is full of joy. He always listens to me carefully. He was kind enough to do the DSC calibration for me. Warm-hearted Joe Schramm and Glenn Garett often closed the gas valve for DSC whenever I had to run during a measurement. I also got many helps from them for the details of experiments. Chris Veazey took me to the freezing Manhattan beach at dawn, for which I am grateful. Scott Roberts showed me how to use image-J software. Dr. Won-Kyu Lim and John Li warmly

welcomed me whenever I stopped by. Dr. Seung-Yub Lee taught me how to use Instron testing machine. Dr. Gang Duan and Dr. Donghua Xu taught me a lot at the beginning of my graduate study. Pam Albertson helped me get through any office business. Tara Scott did shopping for me quickly.

I also like to thank people of GALCIT solid mechanics group. Christian Franck showed me how to use AFM. Dr. Min Tao, Dr. Benny Poon, Dr. Jianheng Zhao, Dr. Arjun and Petros Arakelian helped me utilize the MTS testing machine.

Dr. Daewoong Suh, a researcher of the INTEL corporation with a creative mind, sometimes pushed me hard, but mostly inspired me harder. Thanks to the INTEL research fund that his creativity initiated and brought to us, I could keep myself as a graduate student.

Carol Garland took marvelous TEM pictures for me. I am so grateful for the discussions we had in the middle of her busy schedule. Dr. Chi Ma keeps the SEM facility in good condition so that I could use SEM as often as I wanted. Mike Vondrus is a great machinist who always responded to my rushed request. I'm really grateful to him and his wife for their care on me and my family. Ji Hun Kim, Young Shik Shin and Dr. Ju-Young Kim helped my experiments.

I thank my thesis committee: Prof. William L. Johnson, Prof. Brent Fultz, Prof. Guruswami Ravichandran, Prof. Julia R. Greer and Prof. R. Dale Conner. I also thank the professors who let me pass the candidacy exam: Prof. William L. Johnson, Prof. Brent Fultz, Prof. Marc W. Bockrath and Prof. Wolfgang G. Knauss.

Dr. Sang Lee is the best friend of my father, who lives in Michigan. He and his wife visited my family every year and showed us their love and care.

I thank my lovely wife, Sung-Eun, and my son, Ji-Seok, for being with me. I also would like to express my appreciation to those who made good friends with my wife.

Finally, I give my deepest love to my parents, brother and sisters, in Korea. Their endless and unconditional love has encouraged and supported me ever since I was born.

Abstract

The fracture toughness of three new compositional variants of the Zr-Ti-Be-LTM (Late Transition Metal) family of bulk metallic glasses (BMG's) are studied in the as-cast and annealed condition. Quaternary Zr-Ti-Cu-Be alloys consistently had linear elastic fracture toughness values greater than 80 MPa·$m^{1/2}$, while Vitreloy 1, a Zr-Ti-Cu-Ni-Be alloy, had an average fracture toughness of 48.5 MPa·$m^{1/2}$ with a large amount of scatter. The addition of iron to Vitreloy 1 reduced the fracture toughness to 25 MPa·$m^{1/2}$. The Zr-Ti-Cu-Be alloy, having fracture toughness K_Q = 85 MPa·$m^{1/2}$ as cast, was annealed at various time/temperature combinations. When the alloy was annealed 50^{o}C below T_g, the fracture toughness dropped to 6 MPa·$m^{1/2}$, while DSC and X-ray showed the alloy to still be amorphous. Fracture surfaces were analyzed using scanning electron microscopy. The tougher samples have shown evidence of highly jagged patterns at the beginning stage of crack propagation, and the length scale and roughness of this jagged pattern correlate well with the measured fracture toughness values. These jagged patterns, the main source of energy dissipation in the sample, are attributed to the formation of shear bands inside the sample. This observation provides a strong evidence of significant "plastic zone" screening at the crack tip.

Unlike the unstable fracture behavior of monolithic BMG's, ductile phase containing in-situ BMG composite shows stable crack growth behavior. Application of ductile BMG as a matrix for an in-situ composite with controlled microstructural characteristic length scales maximizes the toughening effect. In order to characterize this highly toughened BMG composite, the elastic-plastic fracture mechanics concept is introduced and the J-parameter is evaluated.

A novel thermoplastic bonding concept is demonstrated based on the unique rheological behavior and pattern-replication ability of bulk metallic glass forming liquids. In this approach, the bulk metallic glass is heated above T_g to the "supercooled liquid" region while a small normal force is applied to the joint. This results in liquid reflow, wetting and a strong bond. Complete

wetting between copper substrates and a layer of platinum based bulk metallic glass leads to an atomistically intimate void-free interface.

Contents

List of Figures

List of Tables

Chapter 1

Introduction, Motivations, and Key Contributions

1.1 Fracture toughness of Bulk Metallic Glasses (BMG's) (Chapters 2-4)

1.1.1 General issues with fracture toughness measurement

Fracture toughness evaluates the resistance of an existing crack against further growth under externally applied load. Fracture toughness has been one of the key material properties for structural applications because all structural parts are likely to have defects such as micro-cracks during service. Despite its importance, fracture toughness is not very well understood by the structural materials research community and its measurement is performed much less frequently than other typical material testing methods such as tension, compression and bending tests because of the intrinsic complexity of the concept and difficulties of the actual measurement, some of which are discussed in the following paragraphs.

(1) Unlike other testing methods, fracture toughness tests involve introducing a certain type of crack into the specimen. Due to the almost infinite number of combinations that initial crack shape and specimen geometry can create, the typical fracture parameter known as K, the stress intensity factor, is used to describe the stress distribution around a crack of given geometry in a body containing the crack. In other words, two different cracks in two different bodies with different geometries have the same stress distribution in around the cracks if their stress intensity factors, K's, are defined to be the same. Solutions of K for hundreds of given crack-specimen geometries can be found from reference books [1, 2], among which, three geometries are defined for standard testing methods in structural metallic materials by ASTM E399 and E1820.

(2) Another complexity arises from plastic deformation in front of a crack due to extremely high stress concentration caused by the crack. The amount of plastic deformation occurring around the crack tip area influences the fracture toughness measurement significantly. As shown in Figure 1-1, thinner specimens tend to resist crack propagation more than thicker specimens by dissipating energy via plastic deformation. The plastic deformation originates from the surface earlier than inside and then spreads to the inside. This is due to reduced constraints on the surface (plane stress condition) which increases deviatoric or maximum shear stress terms. As the specimen thickness increases, the contribution of the surface layer deformation decreases and the thickness dependence is negligible over a critical thickness. Plane strain fracture toughness (K_{IC}) is then defined by this thickness independent fracture toughness in order to provide a size-independent material property.

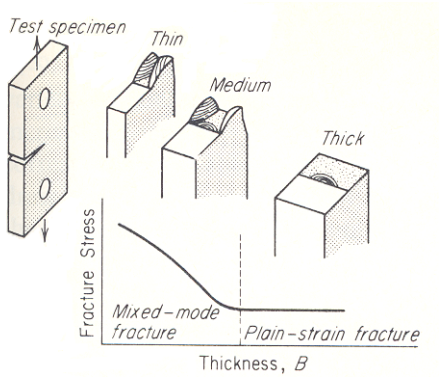

Figure 1-1. Effect of specimen thickness on stress and mode of fracture [3].

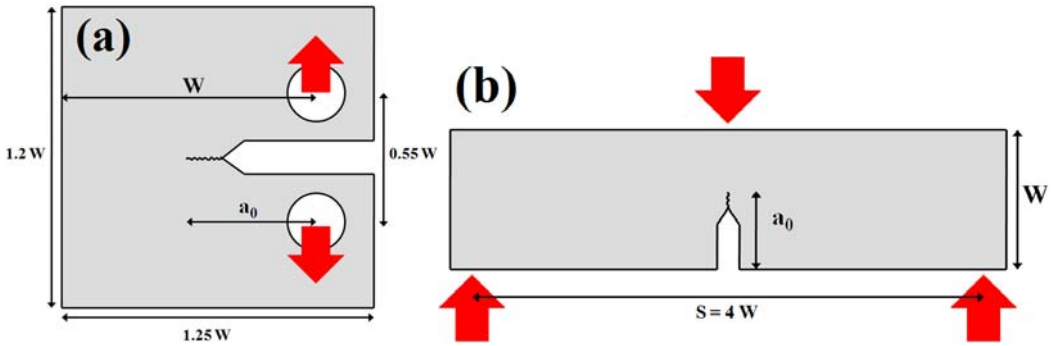

Figure 1-2. Specimen and loading geometries of (a) Compact Tension (CT) and (b) Single Edge Notched Bending (SENB) tests.

The specimen size requirement for metallic materials defined by ASTM E399 is given by Equation 1-1. B, a, and (W-a), are defined in Figure 1-2, and represent specimen thickness, initial crack length and initial ligament length (initially uncracked region), respectively. A material with more resistance to crack propagation ($K_Q \uparrow$) and with less yield stress ($\sigma_Y \downarrow$) requires thicker and larger specimens to interpret the measured critical stress intensity factor (K_Q) as a plane strain fracture toughness (K_{IC}). The size requirement applies to both Compact Tension (CT) and Single Edge Notched Bending (SENB) geometries which are typical standard geometries for fracture toughness measurement (Figure 1-2). The size requirement implies that the size of the plastic zone must be less than 2% of the specimen dimensions in order to obtain a size-independent critical K_{IC} value [4].

$$B, a, (W-a) \geq 2.5 \cdot (K_Q/\sigma_y)^2 \qquad \text{Equation 1-1.}$$

(3) Finally, ASTM standards for fracture toughness measurement require a sharp crack as an initial crack. Since the sharp crack cannot be achieved by conventional machining methods, the only way to generate a sharp crack in front of a notch as depicted in Figure 1-2 is by cyclic fatigue loading. A sharp crack generated in front of the notch is called a ‘pre-crack’. Fracture

toughness data acquired without a pre-crack is called ‘notch toughness’ and, generally, is not accepted as standard fracture toughness (K_{IC}).

1.1.2 History of BMG fracture toughness measurement

Even before the early report of bulk metallic glass forming alloy, Vitreloy 1 [5], mechanical properties including fracture properties of metallic glasses in the form of melt spun ribbon with thickness less than 150 microns had been studied [6-9]. However, thin ribbon specimens have limited validity as standard measurements especially when the ribbon is tough.

After the discovery of Vitreloy 1 [5], rigorous fracture toughness measurements on this alloy were performed by various research groups [10-14]. Although there was a significant scatter within the early stage fracture data, 16~55 $MPa \cdot m^{1/2}$, the evaluated plane strain fracture toughness number is pretty because it is comparable to that of conventional crystalline metals as shown in Table 1-1 [15]. However, it is also well known that BMG’s have almost zero ductility in tension. The unusual combination of zero ductility but high fracture toughness has been attributed to the formation of a high density of shear bands in front of a crack based on observation of shear band networks that evolved on the outer surfaces of specimens [16] as shown in Figure 1-3. However, this observation is based on shear bands formed on surfaces where the plane stress condition dominates.

Table 1-1. Typical values of K_{IC} [15].

Material	Yield strength (MPa)	Fracture toughness K_{IC} (MPa·$m^{1/2}$)
4340 steel	1470	46
Maraging steel	1730	90
Ti-6Al-4V	900	57
2024-T3 Al alloy	385	26
7075-T6 Al alloy	500	24

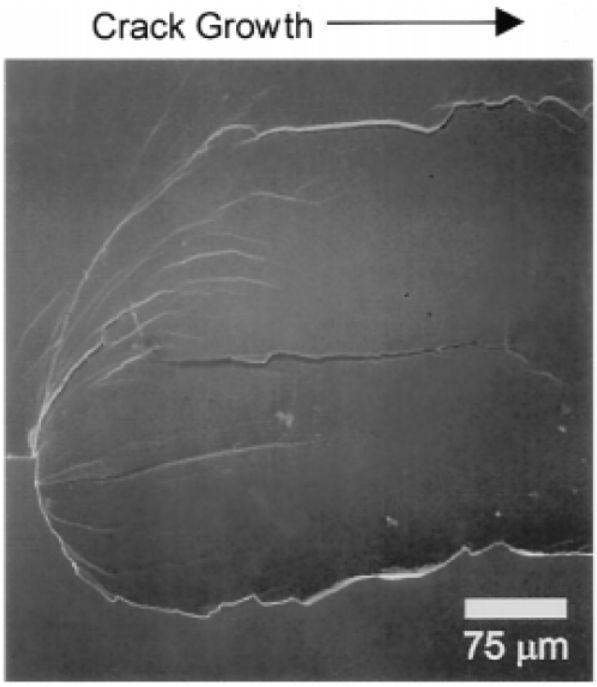

Figure 1-3. SEM micrograph of cracks developed from shear bands [16].

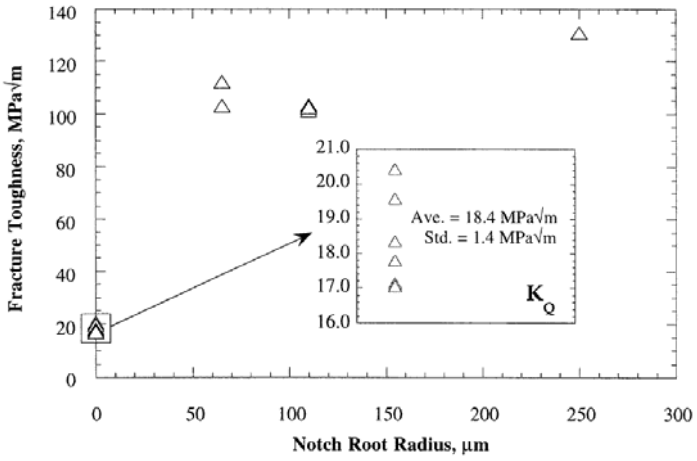

Figure 1-4. Notch toughness, K_Q, as a function of notch root radius. K_Q data obtained on fatigue pre-cracked specimens (i.e., $\rho \approx 0$) are enlarged in inset box [10].

Among the early measurements for Vitreloy 1, the report by Lowhaphandu et al. [10] compared fracture behavior of pre-cracked specimen with those of various notch root radii. As shown in Figure 1-4, the fracture toughness of this BMG was 18.4 MPa·$m^{1/2}$ with a sharp pre-crack, but increased to 130 MPa·$m^{1/2}$ by using a notch instead of a pre-crack.

Later, additional BMG's were measured using notch toughness measurements [17-20]. Together with reports on melt spun ribbon toughness [8, 9], this is shown in Figure 1-5, Lewandowski et al. [21] have proposed a universal correlation between the energy of fracture and the Poisson's ratio (or the elastic modulus ratio G/B) for various metallic glasses. They even showed that the fracture toughness data for annealed BMG's are fit by the proposed universal correlation. However, the data collected in their report [8, 9, 17-20, 22] were not consistent in the testing method used. Furthermore, the annealing experiments used for the fracture toughness study [19] caused crystallization or partial crystallization of specimens [23] which, in turn, increases shear modulus and decreases Poisson's ratio much more than structural relaxation

annealing (causing no crystallization) generally does [24]. Therefore, it appears that a more rigorous study is required to establish such a universal correlation in the BMG systems.

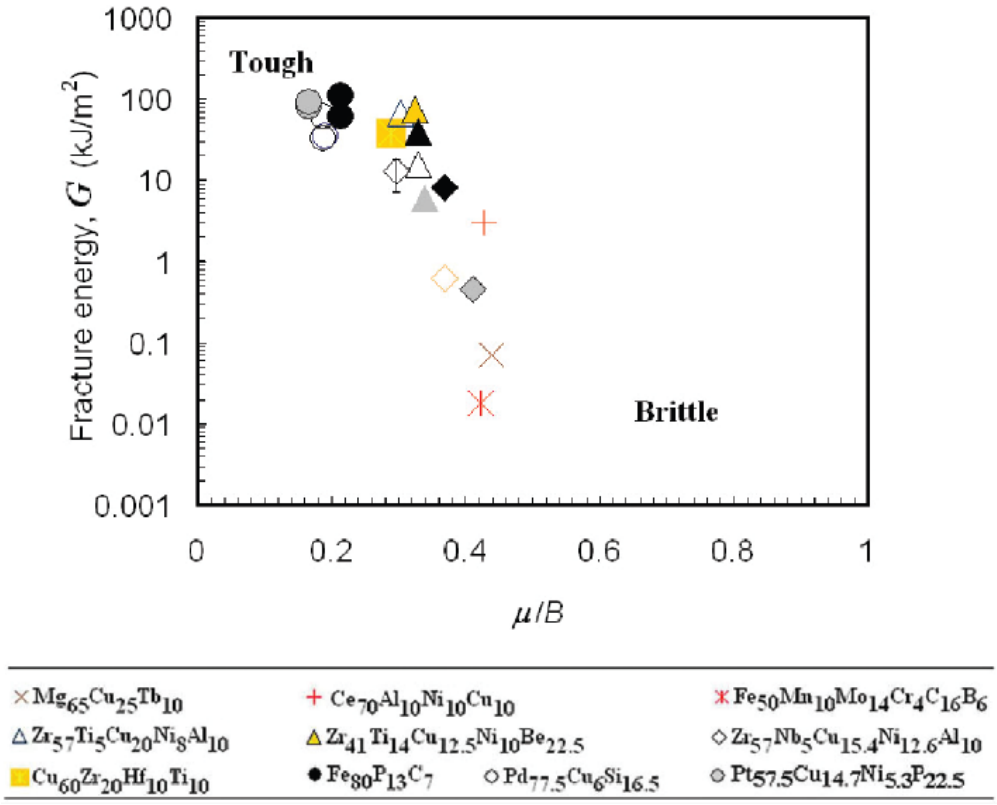

Figure 1-5. The correlation of fracture energy G with elastic modulus ratio μ/B for all the as-cast (unannealed) metallic glasses [21]. In this figure,Lewandowski et al. used G for fracture energy, not shear modulus, with the formula $G= K^2/E/(1-\nu^2)$. Instead, μ is used to denote the shear modulus which is generally expressed by 'G.'

1.1.3 Motivations and key contributions

As stated above, there are still unsolved problems in understanding of the fracture toughness of BMG's especially regarding the major determining factors for fracture toughness. Part of this thesis is devoted to address the following issues:

(1) The effect of composition on fracture toughness. (Chapter 2)

(2) Evidence for the existence of a plastic zone in front of crack. (Chapter 3)

(3) The relationship between fracture toughness and structural relaxation. (Chapter 4)

In chapter 2, three new compositional variants of the Vitreloy 1 are discussed. Not only is this work the first report on the effect of compositional variation on fracture toughness, but the work also proves the effectiveness of fracture toughness measurements for evaluating the mechanical stability of BMG's. It is found that fracture toughness is the most distinguishing parameter to characterize BMG alloys (in contrast to other mechanical properties.) In other words, while properties such as elastic modulus and compressive yield strength show only weak variation with alloy composition, fracture toughness varies much more significantly.

In chapter 3, through detailed observation of fracture surfaces, the existence of a plastic zone screening the crack tip is found. This 'plastic zone' exhibiting jagged patterns caused by the operation of shear bands inside fracture specimen is the main source of energy dissipation during a fracture test. The length and roughness of this plastic zone features correlate well with the measured fracture toughness values.

In chapter 4, the embrittlement of a tough BMG is studied by fracture toughness and elastic property measurements. While maintaining glassy structure, the fracture toughness drops significantly by relaxing the glassy structure into lower temperature.

Through this research, better understanding of the fracture behavior of BMG's has been acquired. It appears that the previously proposed simple universal correlation between fracture energy and Poisson's ratio [21] cannot generally explain the fracture behavior of BMG system.

1.2 Fracture toughness characterization of ductile phase containing in-situ BMG composite (Chapter 5)

Although BMG's are known to have high fracture toughness, the fracture behavior of the monolithic BMG's is unstable under tension loading. Discovery of ductile phase containing in-situ BMG composites [25, 26] were the first reported BMG materials with tensile ductility. This composite microstructure forms by the solidification of a dendritic Zr-Ti rich β-phase with a body centered cubic structure followed by subsequent vitrification of remaining liquid to form a glassy matrix (Figure 1-6). Both phases are formed by processes predictable from a pseudo-binary phase diagram [27]. Both phases (glass and crystal) form during cooling and show atomically sharp, intimate and apparently strong interfaces. The fracture toughness evaluation of these in-situ composites has been reported [28]. Although the reported fracture toughness values were not very high, as shown in Figure 1-7, fracture resistance curves as a function of crack extension (R-curves) show stable crack growth from a sharp fatigue pre-crack during fracture testing. The steeply rising R-curve of the composite can be attributed to a marked increase in fracture resistance with crack extension.

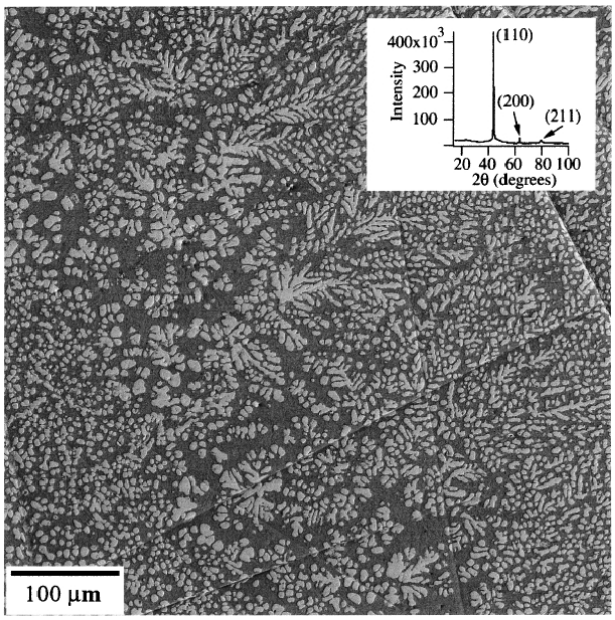

Figure 1-6. SEM backscattered electron image of in-situ composite microstructure (Inset : X-ray diffraction pattern) [25].

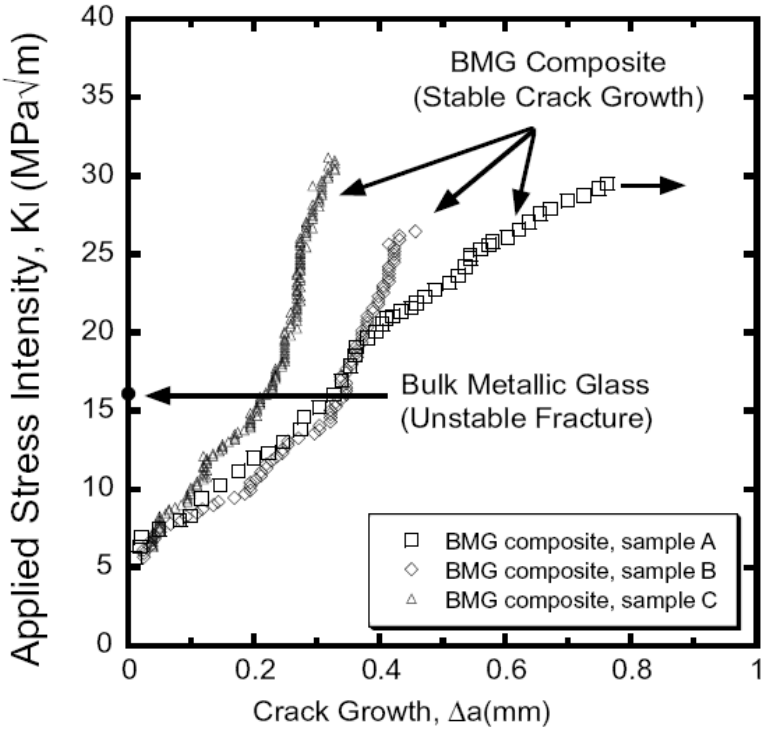

Figure 1-7. Fracture resistance curves for three composite specimens are compared with the fracture toughness of the monolithic alloy (Vitreloy 1) [28].

Recently, significant improvements in the mechanical properties of ductile phase containing in-situ BMG composites have been achieved by Hofmann et al. [29, 30]. Compared to the previous in-situ composites developed by Kim et al. [25, 26], the new BMG composites have the following features:

(1) Increased Ti content and removal of Ni to reduce density. Removal of Ni is also known to enhance fracture toughness of the glass and suppress possible nucleation of brittle intermetallic crystalline phases during processing [31-33].

(2) A homogeneous and coarsened microstructure. Earlier composite has cooling rate dependent microstructures. Ingots cooled from above the alloy liquidus showed large variation in the overall dendrite length scale and interdendrite spacings. In order to produce a uniform microstructure, cooling from the molten state (T > 1100°C) is interrupted at the temperature in the semi-solid two-phase region (T=~800-900°C) between the alloy liquidus and solidus temperature. The sample is held isothermally for several minutes in this region. The isothermal hold in the two-phase region allows the nucleation, growth, and coarsening of the ductile dendrite phase to approach thermodynamic equilibrium prior to final quenching. After the isothermal hold, the semi-solid mixture is cooled to vitrify the remaining liquid phase, and obtain a coarse and uniform dendrite distribution.

(3) The length scale of the dendritic phase is on the order of the length scale of deformation in the glass matrix. With softer dendrite phases deforming first and, subsequently initiating shear bands into the BMG matrix, interdendrite distance is limited to below a characteristic length scale [34, 35]. Matching of microstructural length scales to this characteristic length scale limits shear band extension, suppresses shear band opening, and avoids crack development. The composite microstructure, with softer dendrites, creates short (stable) and dense shear bands rather than long (unstable) and sparse shear bands. This mechanism is illustrated in Figure 1-8.

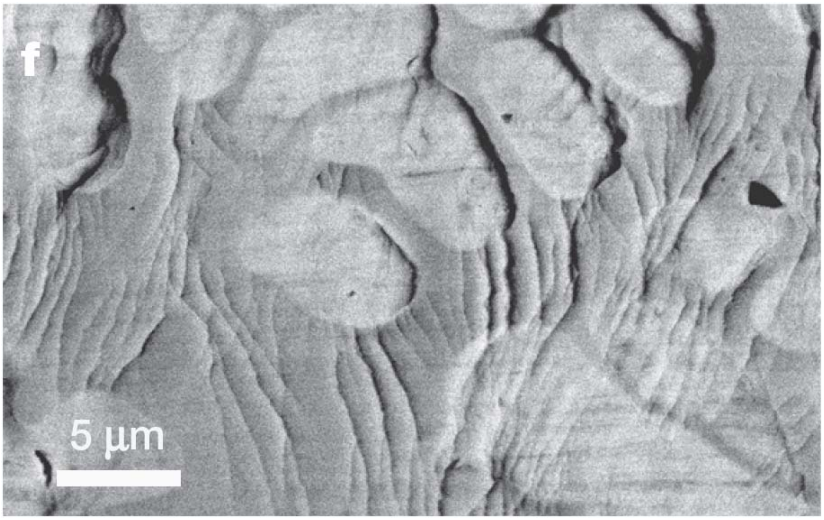

Figure 1-8. SEM micrograph showing interaction of shear bands with ductile phases [29].

As shown above, these in-situ composites show stable crack growth behavior unlike the monolithic BMG's. To compare these new composites with other tough conventional crystalline materials, it is necessary to evaluate the fracture properties using standard elastic-plastic fracture mechanics parameters. Chapter 5 describes the fracture behavior of the newly developed in-situ composites and the evaluation procedure for the elastic-plastic fracture mechanics parameter, J. This work is the first reported "J-integral" evaluation applied to the BMG systems and provides a basis for placing the new in-situ BMG composites among the toughest known materials.

1.3 Novel Joining method using BMG solder (Chaper 6)

One of the characteristics of BMG is the existence of a supercooled liquid region between glass transition (T_g) and crystallization (T_x) temperatures on heating. Figure 1-9 shows a typical Differential Scanning Calorimetry (DSC) curve on heating of a BMG. In between T_g and T_x, the supercooled liquid region exists. The state of the BMG in this region is a viscous liquid and the atomic configuration of the BMG easily rearranges to accommodate plastic flow.

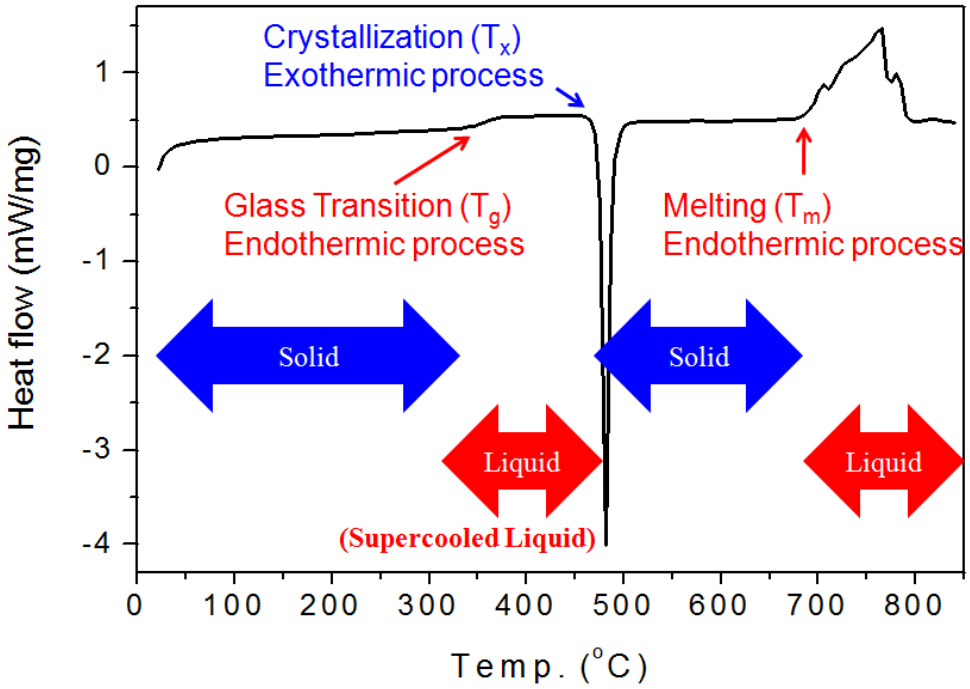

Figure 1-9. A typical Differential Scanning Calorimetry (DSC) curve of a BMG on heating.

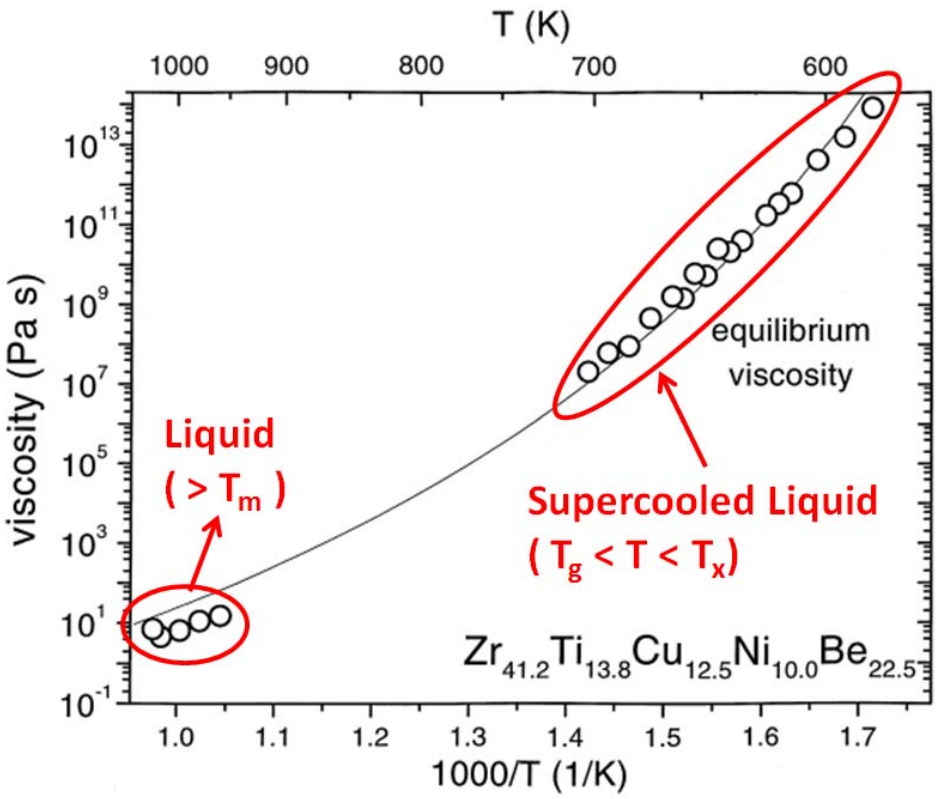

Figure 1-10. A typical equilibrium viscosity curve of a BMG (Vitreloy 1) at molten and supercooled liquid regions [36].

As shown in Figure 1-10, the viscosity of a BMG is described by a single curve as a function of temperature in two different regions, the high temperature melt and the supercooled liquid. Although the viscosity of the supercooled liquid is higher than that of the molten BMG, supercooled liquids have sufficient fluidity to exhibit flow under small applied pressures. The viscosity of the supercooled liquid of a BMG can be as low as 6×10^{4} Pa·s, similar to that of viscous polymer melts [32]. The fluidity of a supercooled BMG forming liquid also makes micron-sized pattern replication possible [37]. Thus it is reasonable to expect that the supercooled BMG forming liquid can wet and bond to another metal surface during this configurational

rearrangement process. As shown in Figure 1-9, the bonding product processed in the supercooled liquid region is expected to have different characteristics from that of the conventional soldering product in which the crystalline solder melts completely to form a joint, because the present process temperature is much lower than the equilibrium melting temperature of the solder. This low temperature soldering concept may appeal to the microelectronics industry in particular, because the solders in microelectronics generally suffer the high homologous temperature in service. This aspect is discussed more in Chapter 6.

In chapter 6, a novel thermoplastic bonding concept is demonstrated based on the unique rheological behavior and pattern-replication ability of bulk metallic glass forming liquids. This work is the first report of joining metals using a BMG in the supercooled liquid state. To the author's knowledge, no work on this concept has been reported. Although this work was initially motivated by the urge to replace the current soldering technology in microelectronics industry, the present result is probably applicable to range of materials to be bonded together with different classes of BMG.

1.4 Related publications

Chapter 2

C.P. Kim, **J.-Y. Suh**, A. Wiest, M.L. Lind, R.D. Conner and W.L. Johnson, ***Fracture toughness study of new Zr-based Be-bearing bulk metallic glasses***, Scripta Materialia 60 (2008) 80-83.

This paper reported the development of new alloys, their thermal properties and mechanical properties. The author contributed to this paper by performing mechanical property evaluation.

Chapter 3

J.-Y. Suh, C.P. Kim, R.D. Conner, M.D. Demetriou and W.L. Johnson, ***Correlation between fracture surface morphology and toughness in Zr-based bulk metallic glasses***, submitted to Acta Materialia.

Chapter 5

D.C. Hofmann, **J.-Y. Suh**, A. Wiest, G. Duan, M.L. Lind, M.D. Demetriou and W.L. Johnson, ***Designing metallic glass matrix composites with high toughness and tensile ductility***, Nature 451 (2008) 1085-1089.

The author evaluated fracture property of the novel composite alloys.

Chapter 6

J.-Y. Suh, B. Lohwongwatana, C.M. Garland, R.D. Conner, W.L. Johnson and D. Suh, ***Novel thermoplastic bonding using a bulk metallic glass solder***, Scripta Materialia 59 (2008) 905-908.

References

[1] H. Tada, P.C. Paris and G.R. Irwin, The stress analysis of cracks handbook, 2nd ed. (Paris Production and Del Research Corp., 1985).

[2] Y. Murakami, Stress Intensity Factors Handbook (Oxford Pergamon Press, 1987).

[3] G.E. Dieter, Mechanical Metallurgy, 3rd ed. (McGraw-Hill, 1986) p.357.

[4] T.L. Anderson, Fracture Mechanics: Fundamentals and Applications, 1st ed. (CRC Press, 1991) p.431.

[5] A. Peker, W.L. Johnson, Appl. Phys. Lett. 63 (1993) 2342.

[6] A.T. Alpas, L. Edwards and C.N. Reid, Metall. Trans. 20A (1989) 1395.

[7] D.G. Ast and D. Krenitsky, Mater. Sci. Eng. 23 (1976) 241.

[8] L.A. Davis, Metall. Trans. 10A (1979) 235.

[9] C.H. Shek, G.M. Lin, K.L. Lee and J.K.L. Lai, J. Non-Cryst. Solids 224 (1998) 244.

[10]. P. Lowhaphandu and J.J. Lewandowski, Scripta Mater. 38 (1998) 1811.

[11]. C.J. Gilbert, V. Schroeder and R.O. Ritchie, Met. Mat. Trans. 30A (1999) 1739.

[12]. D. Suh and R.H. Dauskardt, J. Non-Cryst. Solids 317 (2003) 181.

[13]. D. Suh and R.H. Dauskardt, Ann. Chim. Sci. Mat. 27 (2002) 25.

[14]. R.D. Conner, A.J. Rosakis, W.L. Johnson and D.M. Owen, Scripta Mater. 37 (1997) 1373.

[15] G.E. Dieter, Mechanical Metallurgy, 3rd ed. (McGraw-Hill, 1986) p.353.

[16] K.M. Flores and R.H. Dauskardt, Scripta Mater. 41 (1999) 937.

[17] X.K. Xi, D.Q. Zhao, M.X. Pan, W.H. Wang, Y. Wu and J.J. Lewandowski, Phy. Rev. Lett. 94 (2005) 125510.

[18] P. Wesseling, T.G. Nieh, W.H. Wang and J.J. Lewandowski, Scripta Mater. 51 (2004) 151.

[19] J.J. Lewandowski, Mater. Trans. JIM 42 (2001) 633.

[20] J. Schroers and W.L. Johnson, Phys. Rev. Lett. 93 (2004) 255506.

[21] J.J. Lewandowski, W.H. Wang and A.L. Greer, Phil. Mag. Lett. 85 (2005) 77.

[22] P.A. Hess, S.J. Poon, G.J. Shiflet, R.H. Dauskardt, J. Mater. Res. 20 (2005) 783.

[23] W.H. Wang, R.J. Wang, W.T. Yang, B.C. Wei, P. Wen, D.Q. Zhao and M.X. Pan, J. Mater. Res. 17 (2002) 1385.

[24] W.L. Johnson, M.D. Demetriou, J.S. Harmon, M.L. Lind and K. Samwer, MRS Bull. 32 (2007) 644.

[25] C.C. Hays, C.P. Kim and W.L. Johnson, Phys. Rev. Lett. 84 (2000) 2901.

[26] F. Szuecs, C.P. Kim and W.L. Johnson, Acta Mater. 49 (2001) 1507.

[27] S.Y. Lee, C.P. Kim, J.D. Almer, U. Lienert, E. Ustundag and W.L. Johnson, J. Mater. Res. 22 (2007) 538.

[28] K.M. Flores, W.L. Johnson and R.H. Dauskardt, Scripta Mater. 49 (2003) 1181.

[29] D.C. Hofmann, J.-Y. Suh, A. Wiest, G. Duan, M.L. Lind, M.D. Demetriou and W.L. Johnson, Nature 451 (2008) 1085.

[30] D.C. Hofmann, J.-Y. Suh, A. Wiest and W.L. Johnson, Scripta Mater. 59 (2008) 684.

[31] R.D. Conner, W.L. Johnson, Scripta Mater. 55 (2006) 645.

[32] G. Duan, A. Wiest, M.L. Lind, J. Li, W.-K. Rhim and W.L. Johnson, Adv. Mater. 19 (2007) 4272.

[33] C.P. Kim, J.-Y. Suh, A. Wiest, M.L. Lind, R.D. Conner and W.L. Johnson, Scripta Mater. 60 (2008) 80.

[34] R.D. Conner, W.L. Johnson, N.E. Paton and W.D. Nix, J. Appl. Phys. 94(2) (2003) 904.

[35] R.D. Conner, Y. Li, W.D. Nix and W.L. Johnson, Acta Mater. 52 (2004) 2429.

[36] T.A. Waniuk, R. Busch, A. Masuhr and W.L. Johnson, Acta Mater. 46 (1998) 5229.

[37] J. Schroers, Q. Pham and A. Desai, J. Mems 16 (2007) 240.

Chapter 2

Effect of composition on fracture toughness of new Zr-based Be-bearing bulk metallic glasses

Three new compositional variants of the Zr-Ti-Be–LTM (late transition metal) family of metallic glasses are discussed. Thermal stability, $\Delta T=T_x-T_g$, was increased from 82°C for $Zr_{41.2}Ti_{13.8}Cu_{12.5}Ni_{10}Be_{22.5}$ (Viterloy 1) to 141°C for $Zr_{44}Ti_{11}Cu_{20}Be_{25}$. It is found that fracture toughness is the most distinguishing parameter characterizing the alloys in contrast to other mechanical properties. Quaternary alloys consistently had fracture toughness values exceeding 80MPa·$m^{1/2}$, while for Vitreloy 1 K_Q=48.5MPa·$m^{1/2}$ with a large amount of scatter. Adding iron reduced the fracture toughness to 25MPa·$m^{1/2}$.

2.1 Introduction

Vitreloy 1 ($Zr_{41.2}Ti_{13.8}Cu_{12.5}Ni_{10}Be_{22.5}$) [1], the first commercial Bulk Metallic Glass (BMG), has been the subject of extensive research in scientific and engineering fields. Vitreloy 1 may be cast into rods 25 mm in diameter [2], which exceeds that of most bulk glass forming alloys. It has high thermal stability; ΔT, the difference between a glass transition temperature (T_g) and a crystallization temperature (T_x), is as large as 82°C [3], high yield strength, and high fracture toughness [4-8].

In recent studies on Zr-based Be-bearing BMGs, a number of new alloys with superior thermal stability and comparable glass forming ability have been reported [9-11]. Furthermore, a correlation between a compositional ratio of (Zr,Ti) to other elements and the elastic properties was established in these Vitreloy-like Zr-based Be-bearing alloys [9]. The elastic properties of BMGs are important because mechanical yielding of BMG is strongly correlated with shear modulus (G) [12] and, in some systems, fracture toughness correlates well with Poisson's ratio (ν) [13].

Historically, compression tests have been a prevailing evaluation method for BMGs. However, frictional forces due to closing stresses stabilize shear bands, giving rise to multiple shear bands and global plasticity, which obscures the real stability with respect to failure along an individual shear band during deformation [14]. By comparison, fracture toughness is a measure of the resistance of an existing crack to propagation under an opening or shear stress. Mode-1 fracture toughness evaluates crack resistance under opening loads by where shear bands and opening cracks are less stable than in compression. Although all monolithic BMGs under tensile loading show virtually zero ductility, BMGs have often exhibited relatively high fracture toughness [13,15]. Fracture testing is a desirable method to distinguish and evaluate various BMGs, however limited fracture toughness data on BMGs is available, primarily because most

BMGs lack the robust glass forming ability needed to make the large samples required for fracture toughness testing. Among Zr-based Be-bearing alloys, only one alloy system other than Vitreloy 1 has been studied [16]. No studies have yet been reported regarding the effect of compositional variation on fracture toughness.

In this study, we assess the effect of composition variations on the fracture toughness on Zr-based Be-bearing alloys. Three new alloys have been developed with high glass forming ability as evidenced by a more than 15 mm critical casting thickness. Two alloys, $Zr_{33.5}Ti_{24}Cu_{15}Be_{27.5}$ (Var1) and $Zr_{44}Ti_{11}Cu_{20}Be_{25}$ (Var2), are 4-component (quaternary) alloys without Ni and $Zr_{44}Ti_{11}Cu_{9.3}Ni_{10.2}Be_{25}Fe_{0.5}$ (Var3) is 6-component alloy with Fe as an additional microalloying element. Var 2 and Var 3 are most closely related to $Zr_{44}Ti_{11}Ni_{10.2}Cu_{9.8}Be_{25}$ (known as Vitreloy 1b) [3]. Vitreloy 1b has lower glass forming ability than Vitreloy 1 but a larger ΔT. The (Zr,Ti) concentration in these alloys is maintained at ~55 atomic %, which minimizes the variation in elastic properties [9]. Elastic, thermal and mechanical properties of these alloys were evaluated and compared with those of $Zr_{41.2}Ti_{13.8}Cu_{12.5}Ni_{10}Be_{22.5}$ (Vitreloy 1) to reveal the effect of compositional variation.

2.2 Experimental

Mixtures of elements were alloyed by arc melting under a Ti-gettered argon atmosphere to make BMG ingots. Compression and fracture toughness specimens were prepared by vacuum injection casting BMG ingots into Cu-molds (Figure 2-1). The nominal dimension of the fracture samples was 2.5 mm × 8 mm × 36 mm. The mold incorporated a 2 mm protrusion to form the notch. Approximately 0.15 mm on the faces of each sample was removed from the surface by lapping and polishing, reducing the thickness of each specimen to 1.9~2.2 mm. This procedure

reduces the effects of residual stress resulting from the casting process. A 5-Hz cyclic load was applied to grow a fatigue precrack using an MTS servohydraulic load frame equipped with a 3-pt bend fixture having a 31.75 mm span. Applying a load of approximately $\Delta K \cong 10$ MPa·m$^{1/2}$ and $K_{min}/K_{max} \cong 0.2$, a 1.2~2.5 mm long pre-crack was obtained after 40,000-150,000 cycles. Starting with an initial crack length of ~3.2-4.5 mm (the sum of the notch length and pre-crack), a quasi-static compressive displacement of 0.3 mm/min (K~40 MPa·m$^{1/2}$/min) was applied and the load response of the pre-cracked sample was measured. Fracture toughness, K_Q, was calculated using the formula given by ASTM E399.A3. Here we use K_Q to denote fracture toughness rather than K_{IC} because the sample thicknesses did not guarantee plane strain condition in all cases. The pulse-echo overlap technique with 25MHz piezoelectric transducers was used to measure the shear and longitudinal wave speeds at room temperature enabling calculation of the elastic constants. Sample density was measured by the Archimedean technique according to the ASTM C693-93. Compression tests were performed at room temperature on the Instron 5500R load frame using cylindrical samples of 4 mm diameter, heights from 7 mm to 9 mm, and an aspect ratio close to 1:2. The tests were done with a constant crosshead speed of 0.1 mm min^{-1}. Thermal properties of all alloys were evaluated using differential scanning calorimetry (DSC) at a heating rate of 20K/min. X-ray analysis was performed on a X'Pert Pro x-ray diffractometer to confirm the amorphous nature of samples.

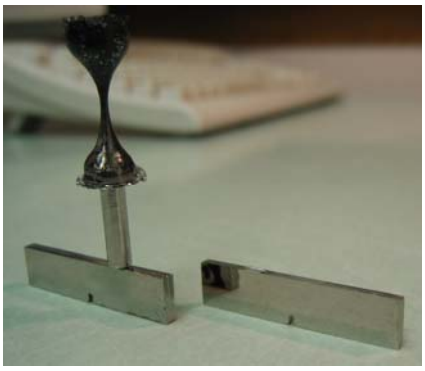

Figure 2-1. Fracture specimen after casting (left) and grinding and polishing (right).

2.3 Results and Discussions

Thermal and elastic properties of the 3 new alloys and Vitreloy 1 are presented in Table 2-1. Glass transition temperatures (T_g) for quaternary Zr-Ti-Cu-Be alloys (Var1 and Var2) are lower than that of Vitreloy1 while the addition of iron to Vitreloy 1 had minimal effect on T_g. On the other hand, these compositions show increased crystallization temperature (T_x), and increased ΔT up to 141°C. Var2 and 3 were derived from a $Zr_{44}Ti_{11}Ni_{10.2}Cu_{9.8}Be_{25}$ (Vitreloy 1b) alloy which has ΔT of 132°C [3]. ΔT is increased by replacing Ni with Cu (Var2), but decreased with the addition of 0.5% Fe in place of Cu (Var3).

Table 2-1. Thermal, elastic and mechanical properties of Zr-based BMG's.

	T_g (°C)	T_x (°C)	ΔT	ρ (g/cc)	G (GPa)	B (GPa)	E (GPa)	ν	σ_y (GPa)
$Zr_{33.5}Ti_{24}Cu_{15}Be_{27.5}$ (Var 1)	333	447	114	5.58	36.8	113	99.6	0.353	1.75
$Zr_{44}Ti_{11}Cu_{20}Be_{25}$ (Var 2)	340	481	141	6.03	35.3	111.2	95.8	0.356	1.8
$Zr_{44}Ti_{11}Cu_{9.3}Ni_{10.2}Be_{25}Fe_{0.5}$ (Var 3)	348	472	124	6.05	35.7	112.2	96.8	0.356	1.86
$Zr_{41.2}Ti_{13.8}Ni_{10}Cu_{12.5}Be_{22.5}$ (Vitreloy 1)	350	432	82	6.09	35.7	115.3	97.1	0.360	1.86

All four alloys have nearly identical elastic properties. This agrees well with the report of Duan et al. [9] in which the dependence of elastic properties on the ratio of (Zr,Ti) to other elements were observed. Yield stresses measured by compression test of Var1 and 2 alloys are slightly lower than the known value of Vitreloy 1 [12] while Var3 alloy has almost identical yield stress to Vitreloy 1. This is not surprising considering the compositional similarity.

Figure 2-2 shows the fracture toughness data of Vitreloy 1 and Var1, 2 and 3. Detailed information of the fracture toughness measurement is listed in Table 2-2. For each composition, we obtained 3 data points except Var2, which had 2. Quaternary Zr-Ti-Cu-Be alloys (Var1 and Var2) consistently had linear elastic fracture toughness values greater than 80 MPa·$m^{1/2}$, while Vitreloy 1, a Zr-Ti-Cu-Ni-Be alloy, had an average fracture toughness of 48.5 MPa·$m^{1/2}$ with a large amount of scatter. The addition of iron to Vitreloy 1 reduced the fracture toughness to 25 MPa·$m^{1/2}$. The error bars reflect the standard deviation of the data.

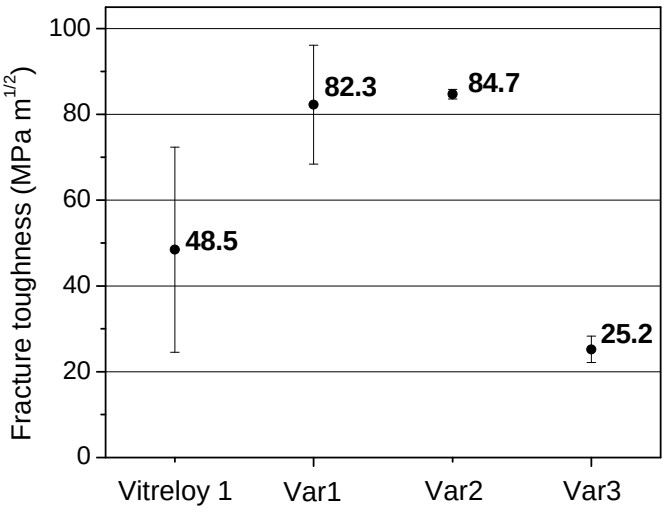

Figure 2-2. Effect of composition on fracture toughness.

Table 2-2. Experimental conditions and data of BMGs used in this study.

a_0: initial crack length (a_0 = length of notch + length of fatigue precrack), K_Q: Fracture toughness calculated using critical fracture load, G: shear modulus, ν: Poisson's ratio.

Composition	thickness (mm)	Initial crack a_0 (mm)	K_Q (MPa·m$^{1/2}$)	G (GPa)	ν
$Zr_{33.5}Ti_{24}Cu_{15}Be_{27.5}$ (Var1)	2.16	3.1	**96.8**	36.7	0.36
	2.19	4.4	**80.8**	36.7	0.35
	2.26	3.5	**69.2**	36.9	0.35
$Zr_{44}Ti_{11}Cu_{20}Be_{25}$ (Var2)	2.13	3.5	**85.5**	35.5	0.36
	2.22	4.3	**83.9**	35.1	0.36
$Zr_{44}Ti_{11}Ni_{10.2}Cu_{9.3}Be_{25}Fe_{0.5}$ (Var3)	2.15	3.7	**27.5**	-	-
	2.16	3.7	**26.4**	35.7	0.36
	2.16	3.4	**21.7**	-	-
$Zr_{41.2}Ti_{13.8}Ni_{10}Cu_{12.5}Be_{22.5}$ (Vitreloy1)	2.18	3.8	**74.4**	35.8	0.36
	1.86	3.2	**49.6**	-	-
	2.22	4.1	**27.3**	35.6	0.36

The specimen size requirement for plane strain fracture toughness (K_{IC}) limits the valid measurable fracture toughness value for a given specimen dimension, as described in ASTM E399: $B, a, (W-a) \geq 2.5 \cdot (K_Q/\sigma_y)^2$

where B = sample thickness, a = initial crack length, and (W-a) = untorn ligament length.

For example, a specimen with thickness of B = 2.1mm and yield stress of 1.8 GPa is limited to a maximum valid fracture toughness value of 52 MPa·m$^{1/2}$. Thus the K_Q values higher than 80 MPa·m$^{1/2}$ of the Var1 and Var2 alloys cannot be regarded as plane strain fracture toughness (K_{IC}). On the other hand, all data points for the Var3 satisfy the plane strain condition. The Vitreloy 1 data lie on the boundary. To obtain valid plane strain fracture toughness, Var1 and

Var2 should be measured with specimens having thickness of ~6mm. Rather than measuring plane strain fracture toughness, we have compared the fracture behavior of specimens in the same geometry.

Reported fracture toughness for Vitreloy 1 varies from 16~55 MPa·$m^{1/2}$ [4-8]. The significant scatter in data has been attributed to variations in processing conditions, such as the cooling rate during casting [17]. The high degree of scatter in the fracture toughness measurements of Vitreloy 1 was also pointed out earlier by Gilbert et al. [5], who reported values ranging from 30 to 68 MPa·$m^{1/2}$. This is comparable to the scatter of the Vitreloy 1 data in this study, 27-74 MPa·$m^{1/2}$. Possible sources of scatter in the data include (1) cooling rate differences during casting, (2) variations in residual stress, and (3) composition fluctuations in a given alloy. Each fracture specimen was produced via vacuum injection casting into copper mold from separately prepared ingots. Injection temperature during the casting process was not strictly controlled so the cooling rate could vary between specimens. In turn, this will leads to differences in the configurational state of the sample and associated free volume distribution [17]. Residual stress develops during the casting process due to the high temperature gradients which arise during sample cooling and solidification. Residual stress is known to affect fracture toughness significantly [16]. According to Aydiner et al. [18], an 8.25mm thick Vitreloy 1 plate cast in a copper mold exhibited -25 to -30MPa surface compression and +10 to +13 interior tension. Their model suggested significant residual stress decreases with decreasing casting thickness. The casting thickness used in this study is 2.5mm. Aydiner et al. also showed that the compressive surface stresses were confined to a relatively thin surface layer. To reduce residual stress effects in the present work, ~10% of the surface layer was removed by grinding. This should significantly reduce residual stress effects in the tested samples. It is noteworthy that Var1, Var2 and Var3 samples studied here show relatively small scatter in fracture toughness values. On the

other hand, the large scatter in the Vitreloy 1 data suggests a greater sensitivity of Vitreloy 1 to process conditions. Removing Ni from Vitreloy 1 significantly reduced experimental scatter and increased fracture toughness. Adding Fe to Vitreloy 1 decreased the experimental scatter, but also decreased the fracture toughness. $Zr_{33.5}Ti_{24}Cu_{15}Be_{27.5}$ (Var1) and $Zr_{44}Ti_{11}Cu_{20}Be_{25}$ (Var2), which contain no Ni, exhibit consistently high fracture toughness while $Zr_{44}Ti_{11}Cu_{9.3}Ni_{10.2}Be_{25}Fe_{0.5}$ (Var3) has consistently low fracture toughness. The reduction in the scatter of fracture toughness resulting from the small composition changes suggests that Vitreloy 1, in the compositional sense, is on a "boundary" separating high toughness (~80MPa·$m^{1/2}$) and low toughness (~25MPa·$m^{1/2}$) materials. In turn, this suggests that the fracture toughness of these BMG's tends to exhibit a relatively sharp "transition" in fracture toughness with varying composition and to a lesser extent with process history for a single composition. In this picture, addition of Ni (or Fe) tends to stabilize the "brittle" phase. Recent reports on very high toughness BMG-composites [14] with a Ni-free Zr-BMG matrix [10] are consistent with this view. A report by Conner et al. [19] of a reduction in bending ductility with Ni addition to Vitreloy alloys also appears to be related. Finally, we note that the addition of Ni (and other composition variations) may modify the free volume distribution in the glass. This is known to be a determining factor in BMG mechanics as shown by Launey et al. [20].

Figure 2-3 shows fracture energy, calculated from fracture toughness and elastic constants, as a function of Poisson's ratio including the data of Fe-based bulk metallic glass [21, 22] and various non-metallic glasses [23]. As pointed out by Lewandowski et al. [13], the data suggest a universal correlation between the energy of fracture and the Poisson's ratio (or the elastic modulus ratio G/B) for various glasses. Although a correlation is suggested over a broad range of glasses, within the data set of Zr-based BMGs, the tendency is not clear. The effect of

composition changes or addition of specific constituent elements (e.g., Ni and Fe in this study) may be a more dominant factor.

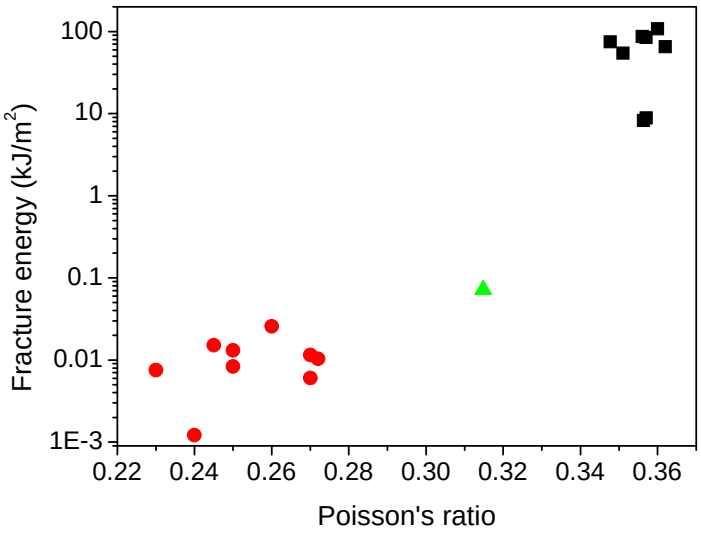

Figure 2-3. Effect of Poisson's ratio (ν) on fracture energy (Fracture Energy = $K^2/E/(1-\nu^2)$).

■: Zr-based bulk metallic glasses measured in this study

▲: Fe-based bulk metallic glass (fracture data from Ref.21 and elastic property data from Ref.22)

●: Various glasses including phosphate glasses and soda lime silicate [23]

2.4 Conclusions

In summary, we have developed Vitreloy type alloys with robust glass forming ability and thermal stability and measured basic properties including thermal, elastic and mechanical properties. While all the alloys have comparable elastic properties and compressive yield strength, the fracture toughness exhibits much greater variation. Ni-free quaternary alloys consistently have

linear elastic fracture toughness values (K_Q) of ~80 MPa·$m^{1/2}$, while Vitreloy 1 had an average fracture toughness of 48.5 MPa·$m^{1/2}$ with a large amount of scatter. The addition of iron to Vitreloy 1 consistently reduces K_Q to 25 MPa·$m^{1/2}$ with little scatter. This suggests that specific elemental constituents can have a significant effect on toughness and thus on the stability of shear bands during deformation under opening stress.

Acknowledgements

The authors would like to thank Prof. G. Ravichandran of GALCIT, Caltech for providing the MTS test system. This work was supported in part by the MRSEC Program of the National Science Foundation under Award Number DMR-0520565.

References

[1] A. Peker, W.L. Johnson, Appl. Phys. Lett. 63 (1993) 2342.

[2] W.H. Wang, C. Dong, C.H. Shek, Mat. Sci. Eng. R 44 (2004) 45.

[3] C.C. Hays, C.P. Kim, W.L. Johnson, Appl. Phys. Lett. 75 (1999) 1089.

[4] P. Lowhaphandu, J.J. Lewandowski, Scripta Mater. 38 (1998) 1811.

[5] C.J. Gilbert, V. Schroeder, R.O. Ritchie, Met. Mat. Trans. 30A (1999) 1739.

[6] D. Suh, R.H. Dauskardt, J. Non-Cryst. Solids 317 (2003) 181.

[7] D. Suh, R.H. Dauskardt, Ann. Chim. Sci. Mat. 27 (2002) 25.

[8] R.D. Conner, A.J. Rosakis, W.L. Johnson, D.M. Owen, Scripta Mater. 37 (1997) 1373.

[9] G. Duan, M.L. Lind, K. De Blauwe, A. Wiest, W.L. Johnson, Appl. Phys. Lett. 90 (2007) 211901.

[10] G. Duan, A. Wiest, M.L. Lind, J. Li, W.-K. Rhim, W.L. Johnson, Adv. Mater. 19 (2007) 4272.

[11] A. Wiest et al., Acta Mater. 56 (2008) 2625.

[12] W.L. Johnson, K. Samwer, Phys. Rev. Lett. 95 (2005) 195501.

[13] J.J. Lewandowski, W.H. Wang, A.L. Greer, Phil. Mag. Lett. 85 (2005) 77.

[14] D.C. Hofmann, J.-Y. Suh, A. Wiest, G. Duan, M.L. Lind, M.D. Demetriou, W.L. Johnson, Nature 28 (2008) 1085.

[15] W.L. Johnson, MRS Bull. 24(10) (1999) 42.

[16] M.E. Launey, R. Busch and J.J. Kruzic, Acta Mater. 56 (2008) 500.

[17] M.E. Launey, R. Busch and J.J. Kruzic, Scripta Mater. 54 (2006) 483.

[18] C.C. Aydiner, E. Ustundag, M.B. Prime and A. Peker, J. Non-Cryst. Solids 316 (2003) 82.

[19] R.D. Conner, W.L. Johnson, Scripta Mater. 55 (2006) 645.

[20] M.E. Launey, J.J. Kruzic, C. Li and R. Busch, Appl. Phys. Lett. 91 (2007) 051913.

[21] P.A. Hess, S.J. Poon, G.J. Shiflet, R.H. Dauskardt, J. Mater. Res. 20 (2005) 783.

[22] V. Ponnambalam, S.J. Poon, G.J. Shiflet, J. Mater. Res. 19 (2004) 1320.

[23] T. Miura, T. Watanabe, Y. Benino, T. Komatsu, J. Am. Ceram. Soc. 84 (2001) 2401.

Chapter 3

Correlation between fracture surface morphology and toughness in Zr-based bulk metallic glasses

Fracture surfaces of Zr-based bulk metallic glasses of various compositions tested in the as-cast and annealed conditions were analyzed using scanning electron microscopy. The tougher samples have shown highly jagged patterns at the beginning stage of crack propagation, and the length and roughness of this jagged pattern correlate well with the measured fracture toughness values. These jagged patterns, the main source of energy dissipation in the sample, are attributed to the formation of shear bands inside the sample. This observation provides strong evidence of significant “plastic zone” screening at the crack tip.

3.1 Introduction

Bulk Metallic Glasses (BMG's) fail without detectable plasticity when loaded in the absence of geometrical confinement, as, for example, in tension or in bending of plates with thicknesses greater than the material characteristic length scale [1,2]. For fracture toughness measurements, typical test geometries are compact tension (CT) and single edge notched bending (SENB). The loading geometry of both methods is bending of plates which are several millimeters thick. Considering that typical characteristic process zone sizes for BMG's are below 1 millimeter [3], one would expect BMG to exhibit poor toughness. However, fracture toughness data for Vitreloy 1 ($Zr_{41.2}Ti_{13.8}Cu_{12.5}Ni_{10}Be_{22.5}$) [4], the first commercial BMG alloy, taken from several reports suggest a range of fracture toughness that extends to values comparable to those of conventional crystalline metals, although the scatter associated with these data is significant. Specifically, the reported fracture toughness of Vitreloy 1 varies between 16 and 55 $MPa \cdot m^{1/2}$ [5-9]. In an additional study however in which single edge notched tension (SENT) was employed, the fracture toughness of Vitreloy 1 was reported to be in excess of 130 $MPa \cdot m^{1/2}$ [10]. Such an extremely high toughness is surprising, given that the tension loading geometry of SENT is geometrically less confined than the bending loading geometry of CT and SENB. The unusual combination of zero ductility but high fracture toughness of BMG's was also pointed out by Ashby and Greer [3]. The perceived high fracture toughness of metallic glasses has been attributed to the formation of a high density of shear bands at the crack tip [11]. However, this argument has only been supported by finite element analysis [12] and observation of shear band networks that evolved on the outer surfaces of specimens [5,10], although it is known that such surface shear bands only reflect the stress state of the free surface dominated by the plane stress condition.

In this study, the fracture surfaces of as-cast and annealed Zr-based BMGs of various compositions were carefully investigated to gain insight on how shear bands form in the regions of plane strain (far from the surface) and whether the extent of shear band propagation correlates to the measured fracture toughness. Various fracture samples from the Vitreloy alloy family were utilized in this study, including Vitreloy 1 ($Zr_{41.2}Ti_{13.8}Cu_{12.5}Ni_{10}Be_{22.5}$), Vitreloy 4 ($Zr_{46.75}Ti_{8.25}Cu_{7.5}Ni_{10}Be_{27.5}$), two different 4-component variants ($Zr_{33.5}Ti_{24}Cu_{15}Be_{27.5}$ and $Zr_{44}Ti_{11}Cu_{20}Be_{25}$) and a 6-component variant ($Zr_{44}Ti_{11}Cu_{9.3}Ni_{10.2}Be_{25}Fe_{0.5}$). Some of the $Zr_{44}Ti_{11}Cu_{20}Be_{25}$ samples were annealed at 3 different temperatures prior to testing. This wide variation in the chemical and thermodynamic state of the material produced a set of fracture toughness data (K_Q) that ranged from 6 MPa·$m^{1/2}$ to 96.8 MPa·$m^{1/2}$, enabling assessment of the key intrinsic material parameters that govern the fracture toughness of these materials. The effect of composition on fracture toughness was discussed in a separate report [13], while the effect of annealing will be discussed elsewhere. In the present study, fracture surface morphologies of specimens of varying composition and specimens with varying fracture toughness values will be investigated in an aim to explore the relationship between shear band propagation and toughness.

3.2 Experimental

Approximately 10g of arc melted BMG of the various compositions was cast into a Cu mold of nominal dimensions of 2.5 mm × 8 mm × 36 mm. The mold incorporated a 2 mm protrusion to form a notch. Lapping and polishing were performed to reduce the possible effect of residual stresses originating from the casting process, which resulted in specimen thicknesses of 1.9~2.2 mm. Fatigue pre-cracking and subsequent quasi-static loading for the determination of the critical load (P_Q) were performed using an MTS servohydraulic load frame equipped with a 3-

pt bend fixture with 31.75 mm span. The geometry of the SENB specimen and the definitions of several geometrical terms used in this study are shown in Figure 3-1(a). By applying a load corresponding to $\Delta K \cong 10$ MPa·m$^{1/2}$ and $K_{min}/K_{max} \cong 0.2$, a 1.1~2.4 mm long pre-crack was obtained after 40,000-150,000 cycles. Starting with an initial crack length of ~3.1-4.4 mm (the sum of the notch length and pre-crack), a quasi-static compressive displacement of 0.3 mm/min (K~40 MPa·m$^{1/2}$/min) was applied and the load response of the pre-cracked sample was measured. Fracture toughness (K_Q) was calculated from the critical load using the formula given in ASTM E399.A3. It should be clarified that K_Q was used to denote fracture toughness rather than K_{IC} because the sample thickness did not guarantee plane strain condition in all cases (addressed later in this paper). The compositions and process conditions of the specimens used for this study, along with geometrical information such as specimen thickness and initial crack length (a_0), are listed in Table 3-1. Specimens are numbered in the order of decreasing K_Q in the first column of Table 3-1. These numbers will be used to refer to the specific specimens in this report.

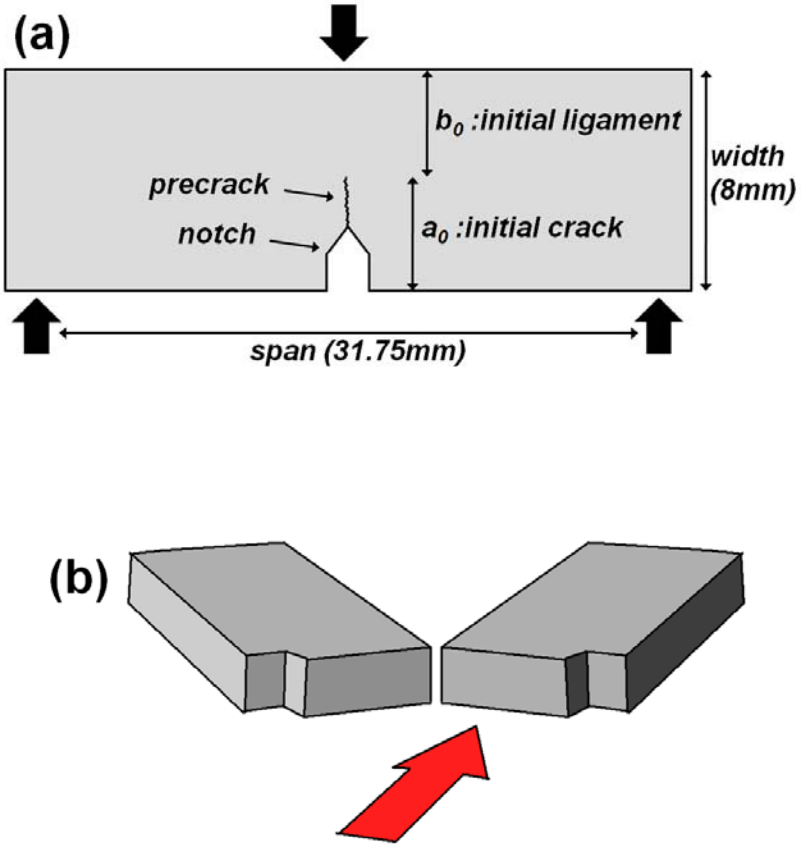

Figure 3-1. (a) Single edge notched bending fracture specimen geometry and dimension. (b) Viewpoint of fracture surface observation after ultimate fracture.

Table 3-1. Experimental conditions and data of BMGs used in this study.

a_0: initial crack length (a_0 = length of notch + length of fatigue pre-crack).

L_A : size of the plastic zone as defined in Figure 3-2(a).

The process zone size is calculated from $K_Q^2/\pi/\sigma_y^2$ (see Equation 3-2)

Sample No.	Composition	Annealing	thickness (mm)	Initial crack a_0 (mm)	K_Q (MPa·m$^{1/2}$)	L_A (mm)	σ_y (GPa)	Process zone size (μm)
S1	$Zr_{33.5}Ti_{24}Cu_{15}Be_{27.5}$	as cast	2.16	3.1	**96.8**	2.33	1.75	974
S2	$Zr_{44}Ti_{11}Cu_{20}Be_{25}$	as cast	2.13	3.5	**85.5**	2.07	1.8	718
S3	$Zr_{44}Ti_{11}Cu_{20}Be_{25}$	as cast	2.22	4.3	**83.9**	1.68	1.8	692
S4	$Zr_{33.5}Ti_{24}Cu_{15}Be_{27.5}$	as cast	2.19	4.4	**80.8**	1.69	1.75	679
S5	$Zr_{41.2}Ti_{13.8}Ni_{10}Cu_{12.5}Be_{22.5}$	as cast	2.18	3.8	**74.4**	1.95	1.86	509
S6	$Zr_{33.5}Ti_{24}Cu_{15}Be_{27.5}$	as cast	2.26	3.5	**69.2**	1.84	1.75	498
S7	$Zr_{46.75}Ti_{8.25}Ni_{10}Cu_{7.5}Be_{27.5}$	as cast	2.21	4.0	**54.6**	1.43	1.86	274
S8	$Zr_{44}Ti_{11}Cu_{20}Be_{25}$	350°C 2hrs	2.12	3.9	**51.3**	1.58	-	259
S9	$Zr_{41.2}Ti_{13.8}Ni_{10}Cu_{12.5}Be_{22.5}$	as cast	1.86	3.2	**49.6**	1.59	1.86	226
S10	$Zr_{44}Ti_{11}Ni_{10.2}Cu_{9.3}Be_{25}Fe_{0.5}$	as cast	2.15	3.7	**27.5**	0	1.86	70
S11	$Zr_{41.2}Ti_{13.8}Ni_{10}Cu_{12.5}Be_{22.5}$	as cast	2.22	4.1	**27.3**	0	1.86	69
S12	$Zr_{44}Ti_{11}Ni_{10.2}Cu_{9.3}Be_{25}Fe_{0.5}$	as cast	2.16	3.7	**26.4**	0	1.86	64
S13	$Zr_{44}Ti_{11}Cu_{20}Be_{25}$	320°C 25hrs	2.09	4.1	**25**	0	-	61
S14	$Zr_{44}Ti_{11}Ni_{10.2}Cu_{9.3}Be_{25}Fe_{0.5}$	as cast	2.16	3.4	**21.7**	0	1.86	43
S15	$Zr_{44}Ti_{11}Cu_{20}Be_{25}$	290°C 62hrs	2.13	3.6	**6**	0	-	4

3.3 Fracture surface of bulk metallic glasses

Figure 3-2 shows the fracture surfaces of the various alloys studied. The viewpoint of observation is as described in Figure 3-1(b). The images in Figure 3-2 are arranged in the order of decreasing fracture toughness. The vertical arrows in all images point to the end of the pre-crack region. Beginning at the pre-crack, ultimate fracture occurred by crack propagation from right-to-left under monotonically increasing quasi-static load. The fracture surfaces of some specimens (Figure 3-2(a)-(e)) show highly jagged patterns at the beginning stage of crack propagation (region "A" in Figure 3-2(a)), and the length ("L_A" defined in Figure 3-2(a), listed in Table 3-1) and roughness of these jagged patterns are in good agreement with the measured fracture toughness values. This jagged region will be termed as 'plastic zone' hereafter. As fracture progresses these plastic zones (jagged patterns) disappear, and the rest of the fracture surface (region "B" in Figure 3-2(a)) shows the typical glassy metal dimple pattern, which is shown in Figure 3-3 and reported in many other studies [5-8,14-17]. The fracture surfaces of low fracture toughness specimens shown in Figure 3-2(f) and (g) don't exhibit the characteristic rough topography in front of the pre-crack, and they appear to be uniformly filled with dimples created by mode 1 opening (Figure 3-3). The severe embrittlement caused by annealing the specimens for 2.5 days at 50°C below the glass transition temperature (T_g, 340°C measured by 20K/min DSC scan [13]) resulted in the fracture surface shown in Figure 3-2(h). This mirror-like fracture surface consists of hundred-nanometer sized dimples (Figure 3-3(d)), as observed by Xi et al. [14].

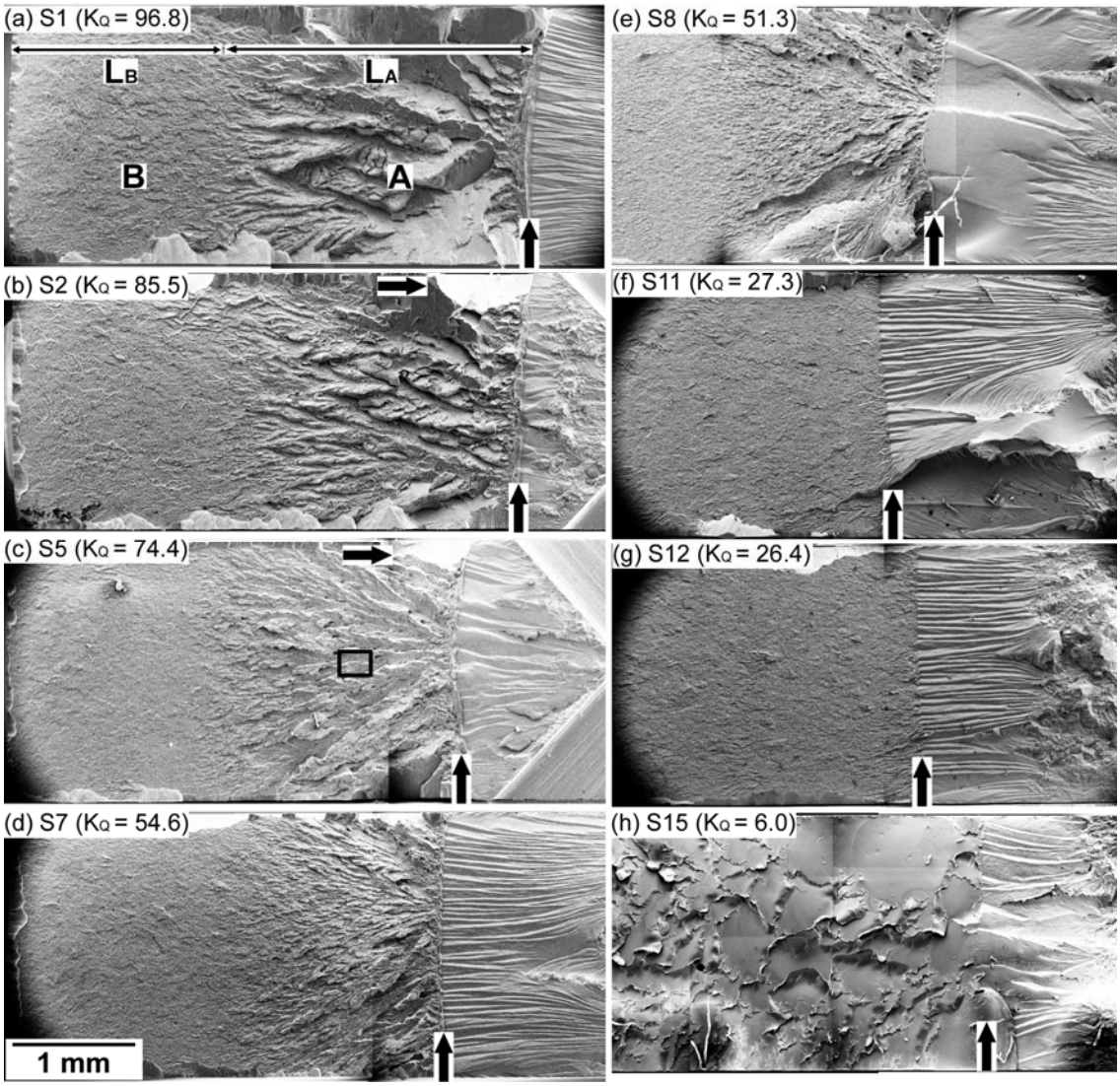

Figure 3-2. Scanning electron micrographs of the fracture surfaces. The vertical arrows mark the location of the initial pre-cracks. Crack propagation is from right to left in each micrograph. (a) specimen S1, (b) S2, (c) S5, (d) S7, (e) S8, (f) S11, (g) S12 and (h) S15. Measured fracture toughnesses (K_Q) are shown in the parentheses for all specimens.

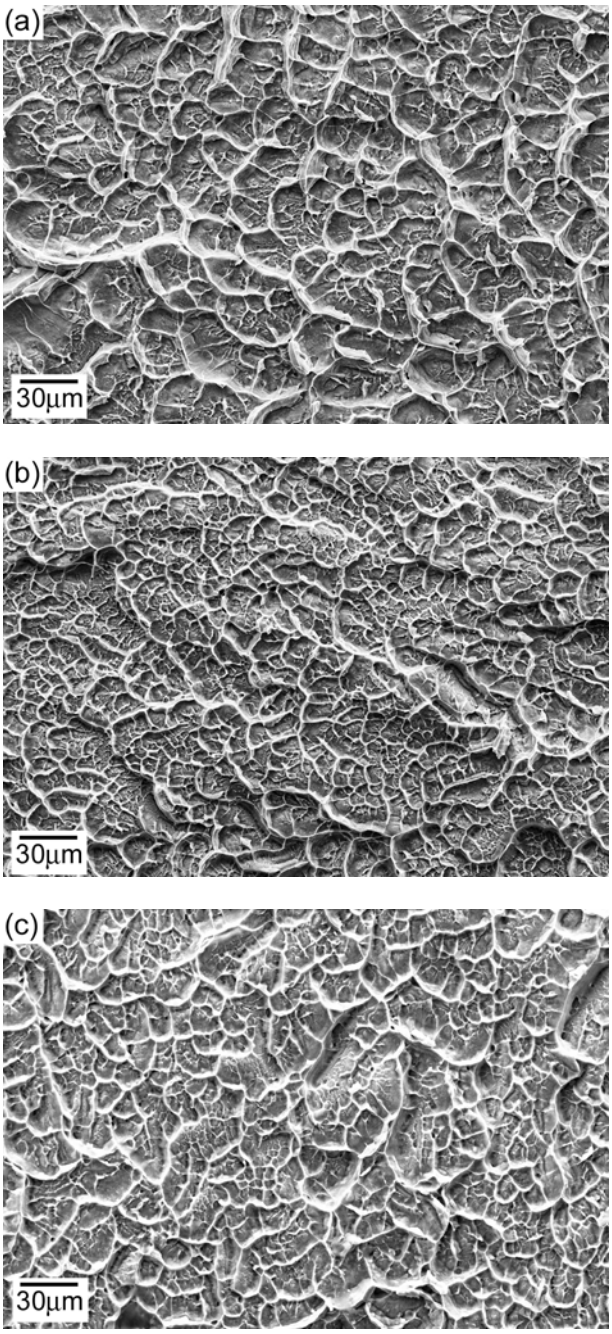

(Figure 3-3. Continued)

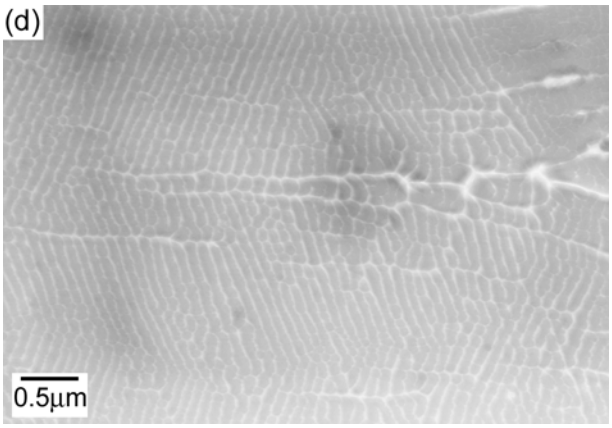

Figure 3-3. Fracture surface of area B (defined in Figure 3-2(a)). (a) specimen S2, (b) S7, (c) S10 and (d) S15.

3.4 Size of the dimple patterns

Dimple patterns of the BMG fracture surfaces (region "B" in Figure 3-2(a)) are shown in Figure 3-3. This region of the fracture surface is covered by isotropic dimples (no specific directionality) indicating that failure occurs by pure opening mode (Mode 1). Dimple patterns have been explained to form by massive flow of softened material at the crack tip [18] based on Taylor's meniscus instability criterion applied to metallic glass fracture by Argon et al. [19] and the correlation between the process zone size and fracture energy recently proposed by Xi et al. [14]. It is noteworthy that even deeply embrittled BMG's form dimple patterns, which is an indication that they undergo a certain degree of plastic flow prior to fracture (Figure 3-3(d)). The mean area of the dimples in Figure 3-3(d) is about $0.03\mu m^2$. However, the dimple size in Figures 3-3(a-c) is not unique, as small dimples reside inside large dimples, and the distinction between these two different dimple sizes is not clear. A distribution of dimple sizes suggests the occurrence of multiple coalescence events accompanied by a significant degree of cavity growth until the final fracture opening occurs. In other words, multiple cavitation events (nucleation of

cavities) and subsequent growth and coalescence of these cavities through plastic flow occur in front of a crack in a highly stressed BMG. Based on this observation, both the nucleation of cavities (which might be governed by the critical wavelength of the meniscus instability [19]) and the stability of the flow in the vicinity of nucleated cavity should be considered important contributing parameters to the fracture behavior. Despite the difficulty in quantifying the size distributions in these figures, it is obvious that the dimple sizes appearing in Figure 3-3(a) are larger than those in Figure 3-3(b) and (c), while the size difference between the dimples in Figure 3-3(b) and (c) is not significant. Likewise, the quaternary $Zr_{33.5}Ti_{24}Cu_{15}Be_{27.5}$ (S1, S4 and S6) and $Zr_{44}Ti_{11}Cu_{20}Be_{25}$ (S2 and S3) alloys listed in Table 3-1, which have K_Q ranging from 69.2 to 96.8MPa·$m^{1/2}$, consistently have patterns of larger dimple sizes comparable to the those shown in Figure 3-3(a), while the patterns of $Zr_{41.2}Ti_{13.8}Cu_{12.5}Ni_{10}Be_{22.5}$ (Vitreloy 1, S5, S9 and S11), $Zr_{46.75}Ti_{8.25}Cu_{7.5}Ni_{10}Be_{27.5}$ (Vitreloy 4, S7) and $Zr_{44}Ti_{11}Cu_{9.3}Ni_{10.2}Be_{25}Fe_{0.5}$ (S10, S12 and S14) alloys, which have K_Q ranging from 21.7 to 74.4MPa·$m^{1/2}$, are characterized by the smaller dimple sizes like those in Figure 3-3(b) and (c). Since the size of a dimple is a measure of BMG plastic flow prior to failure, a tendency of decreasing dimple size with decreasing fracture toughness is conceivable. Interestingly, BMG's that demonstrate a dimple size distribution similar to those in Figures 3-3(b) and (c), i.e. Vitreloy 1, Vitreloy 4 and $Zr_{44}Ti_{11}Cu_{9.3}Ni_{10.2}Be_{25}Fe_{0.5}$, exhibit fracture toughness that may be high or low depending on whether a plastic zone (the jagged zone in front of the pre-crack, defined by region "A" in Figure 3-2(a)) develops during fracture. Specifically, K_Q for these alloys ranges from 49.6 to 74.4MPa·$m^{1/2}$ if the fracture surface reveals a plastic zone, and from 21.7 to 27.5MPa·$m^{1/2}$ if no plastic zone develops. This behavior suggests that this class of BMGs can be either "tough" or "less tough", and this distinction is characterized by a tendency to develop a jagged plastic zone during fracture. Furthermore, it would be reasonable to assume that the mechanical energy spent

to generate this jagged plastic zone should be significantly more than the energy consumed to generate the dimples.

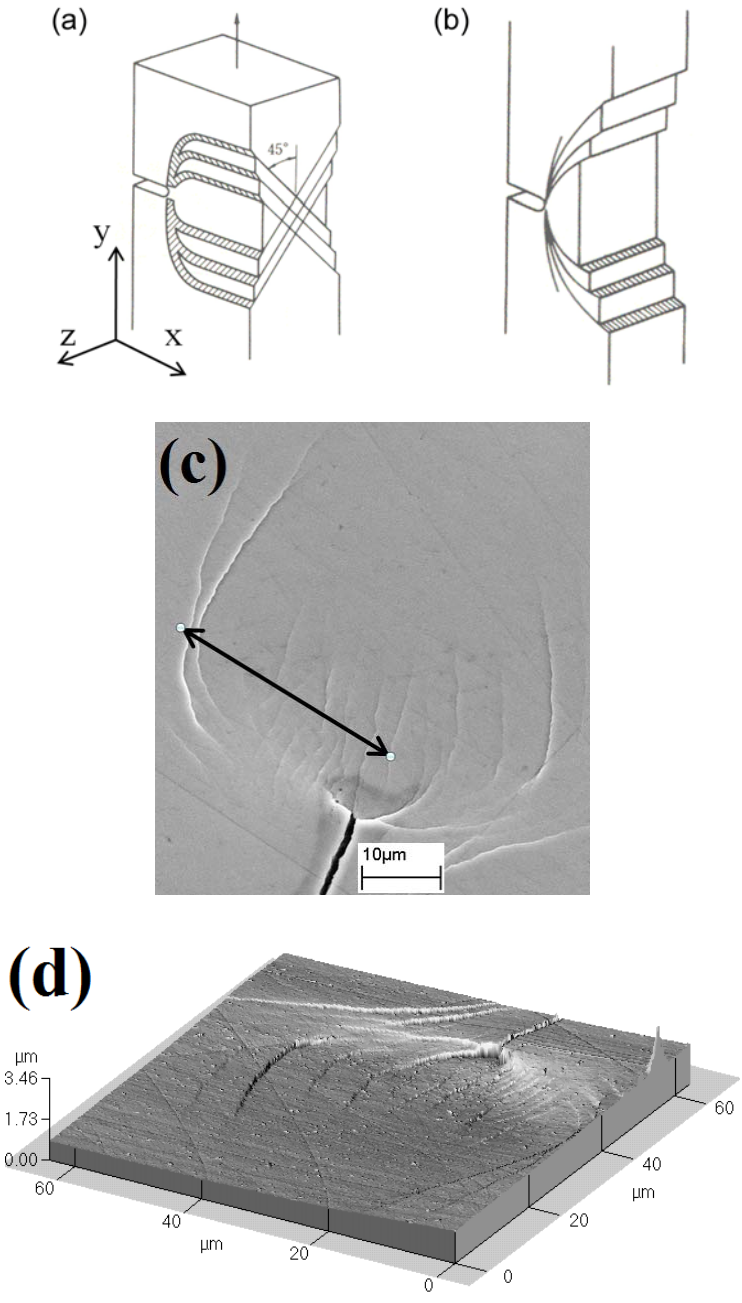

(Figure 3-4. Continued)

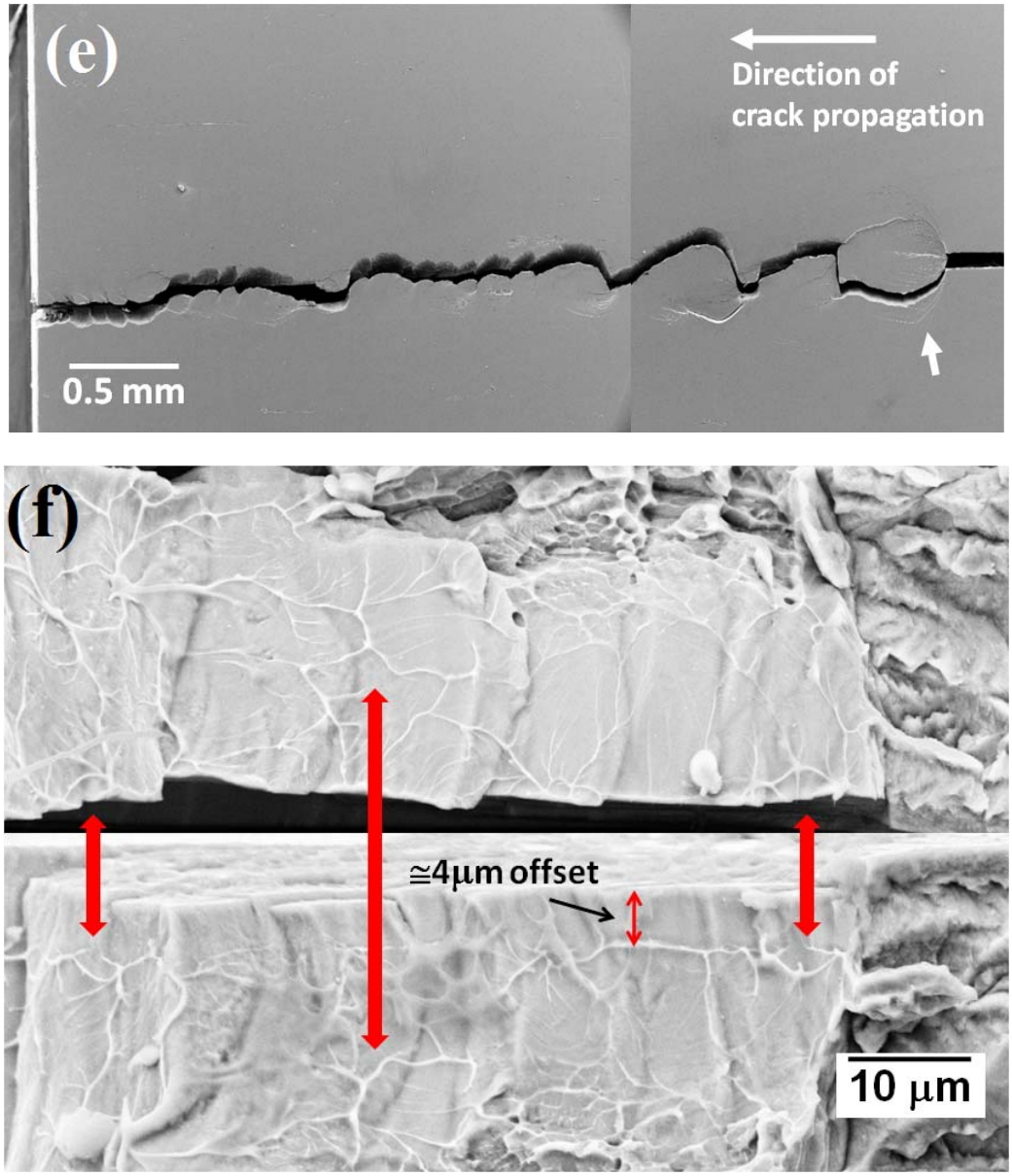

Figure 3-4. Direction of maximum shear stress and resultant slip in front of crack under mode 1 loading [20] under (a) plane stress condition and (b) plane strain condition. (c) Shape of a surface shear band formed around the crack tip (d) Atomic Force Microscopy (AFM) scan of the area shown in (c). (e) Wavy path of crack propagation on the surface of the specimen S2. (f) Fracture surface of specimen S9 on the area shown in (c) and (d).

3.5 Stress state around a crack tip (surface)

On the specimen surface, where the plane stress condition dominates, $\sigma_{zz}=0$. Since $\sigma_{yy} > \sigma_{xx} > \sigma_{zz}=0$, the maximum shear stress component is τ_{yz} as shown in Figure 3-4(a) [20]. The directions of x, y and z axes are defined in Figure 3-4(a). Figure 3-4(d) is a fast-scan AFM image of the area surrounding the pre-crack tip, shown in figure 3-4(c), opened under mode 1 loading. Figure 3-4(d) suggests that the shear offsets are directed into the thickness direction (z-direction), which is in agreement with the hypothesis of figure 3-4(a). The shear offsets appearing on the surface have also been observed to be directed into the thickness direction by Schneibel et al. [21]. Figure 3-4(e) shows the wavy path of a propagated crack on the surface of one of the tougher samples (specimen S2). At the beginning stage of ultimate fracture, the crack follows one of the shear bands distributed around the pre-crack tip, as indicated by the arrow in Figure 3-4(e). Figure 3-4(f) shows the matching surfaces of the fracture that occurred at this specific region (the arrow in Figure 3-4(e)) of specimen S9 (also, the area marked by horizontal arrows in Figure 3-2(b) and (c)). The fracture surfaces are filled with vein-like patterns, and these patterns look different from the typical dimple patterns shown in Figure 3-3. Vein-like patterns are generally observed from fracture surfaces generated by tensile loading conditions [22-25], under which single unstable shear band sliding occurs immediately before fracture. Unlike dimple patterns, which are characterized by isotropic, taller and thicker walls, vein patterns are characterized by shorter and thinner walls. Presumably, the difference in the two patterns can be attributed to a different BMG fluidity at the stage of ultimate fracture. The creation of a vein-like pattern would be associated with a higher fluidity originating from material softening during shear band sliding. Each arrow in Figure 3-4(f) connects the mating points at which the two opposite surfaces were attached before final fracture. From the lower surface in Figure 3-4(f), a shear band offset of about 4 μm can be observed. This observation also agrees well with Figure 3-4(a, c and d) in

terms of the direction of shear band propagation. It should be noted that the shear band pattern at the crack tip indicated by the arrow in Figure 3-4(e) and the fracture along one of these shear bands are only observed in the surface area shown by the horizontal arrows in Figure 3-2(b) and (c). Shear banding and fracture in interior of the specimen appears to be dominated by a different stress state.

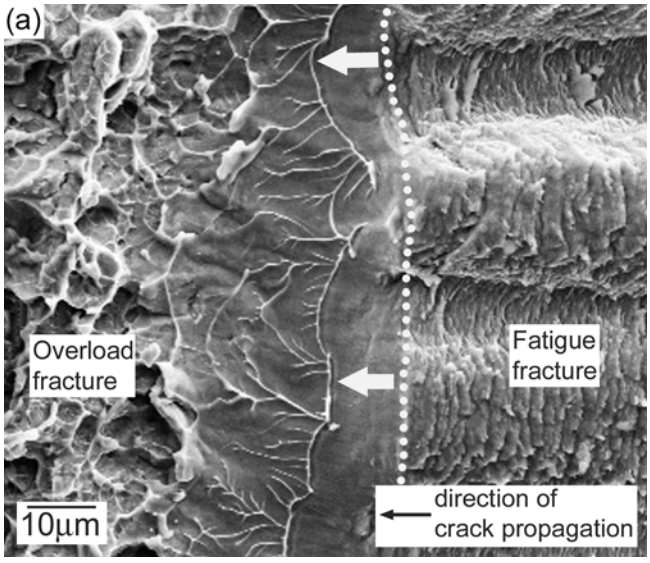

(Figure 3-5. Continued)

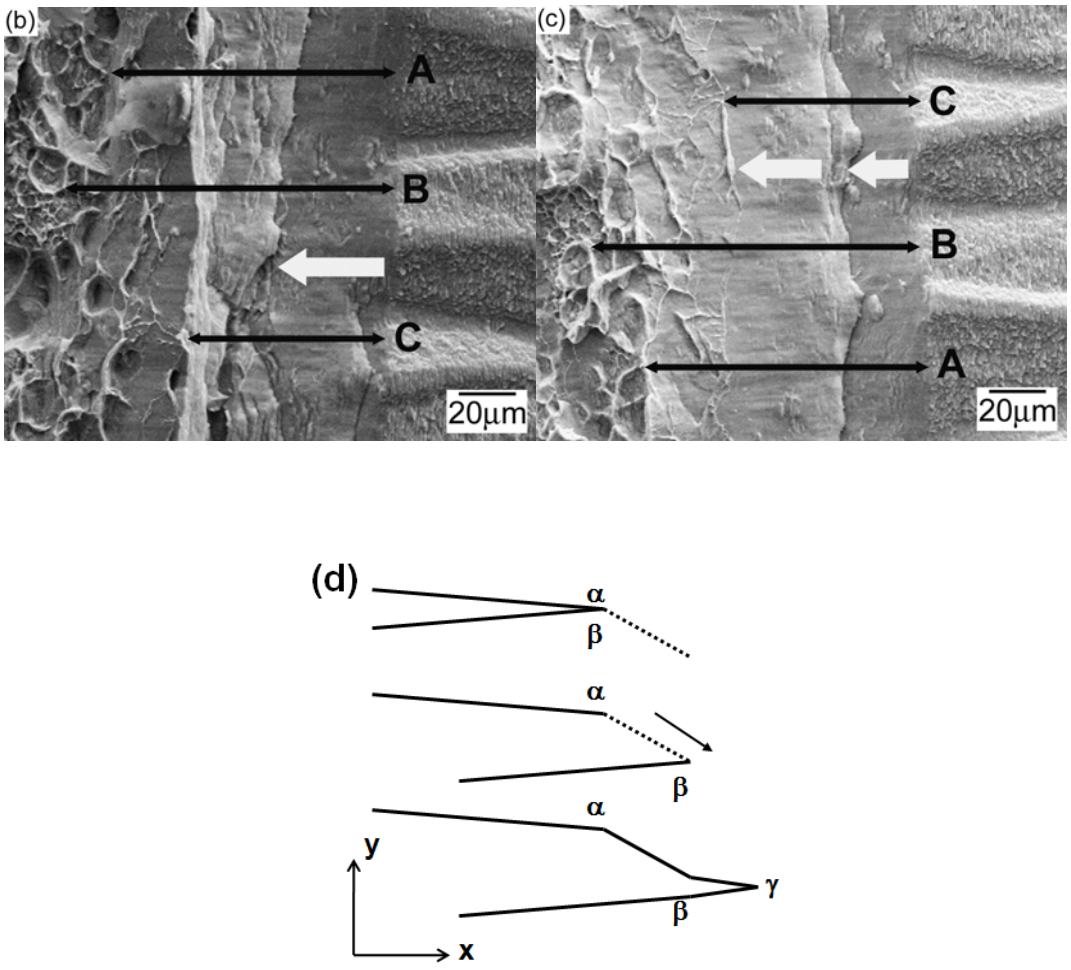

Figure 3-5. (a) boundary (dotted line) between fatigue pre-crack (right) and ultimate fracture (left) of specimen S5. Crack growth direction is from right to left. (b, c) matching surfaces of the boundary of specimen S1. (d) single shear band mechanism for blunting crack tip [17].

3.6 Stress state around a crack tip (interior)

The plane strain condition starts to dominate as the depth from the surface increases. In the plane strain condition, deformation along the z-direction (defined in Figure 3-4(a)) is confined such that the only shear direction available appears to be x-y direction as shown in Figure 3-4(b). A shear band pattern in front of crack tip, as shown in Figure 3-4(b), is also predicted by Tandaiya el al. [12]. Indeed, evidence of such shear band sliding is observed at the boundary between fatigue pre-crack and ultimate overload fracture. Figure 3-5(a) shows the boundary between fatigue pre-crack (right to the dotted line) and ultimate fracture (left to the dotted line) for specimen S5. The dotted line marks the pre-crack tip boundary before ultimate fracture. The crack growth direction is right to left. On the left of the pre-crack tip (dotted line), a smooth featureless region is observed (see thick arrow marks), followed by vein patterned region. This surface feature is pretty similar to the one shown in Figure 3-4(f), which suggests an evidence of shear band sliding and subsequent fracture. The direction of shear band sliding is indicated by the thick arrows. A possible shear banding mechanism for this fracture behavior was proposed by Tatschl et al. to explain crack tip blunting during loading [17] (see Figure 3-5(d)). This single shear band mechanism predicts that the distance between points α and γ and the distance between points β and γ (defined in Figure 3-5(d)) are different due to the shear band sliding. However, the matching surfaces of the specimen S1 shown in Figure 3-5(b) and (c) indicate that the distances of matching features (indicated by thin arrows A,B and C) from the pre-crack tip are almost the same despite the large amount of shear slip (more than 10μm) marked by thick arrows. The single shear banding mechanism proposed in [17] (Figure 3-5(d)) therefore is not adequate to explain this behavior. One possible explanation is a combination of multiple shear bands. Flores and Dauskardt observed multiple steps ahead of the pre-crack [10, see their Figure 4(b)], which is also observed in this study.

The jagged surfaces (defined by the region “A” in Figure 3-2(a)) of the tougher samples shown in Figure 3-2(a)-(e) don’t appear to follow the deformation mode discussed above. The fracture surface shown in figure 3-2(a) has an inclination of about 45° with respect to the mode 1 loading direction, and agrees with Figure 3-4(a), not Figure 3-4(b). However, it should be noted that the specimen in Figure 3-2(a) may not be a perfect example, as it hardly show plane strain deformation occurring inside the sample due to the extensive surface shear banding that reaches almost to the center of the specimen. Other specimens, relatively less affected by the surface shear banding such as specimens in Figure 3-2(b)-(e), must provide better evidence for the plane strain behavior. Specimens in Figure 3-2(b)-(e) have rough and jagged surfaces as well, but the roughness doesn’t appear to result from shear band formation as clearly as Figure 3-2(a). However, careful observation reveals evidence of shear banding even on the less jagged surfaces of Figure 3-2(b)-(e). Figure 3-6 is a magnified image of the squared area marked in Figure 3-2(c). The fracture surface consists of steps running parallel to the crack propagation direction. As previously discussed, vein-like patterns on the surfaces (indicated by arrows) are observed on fracture surfaces generated by tensile loading [22-25]. Extensive shear band propagation (sliding) occurs up to a critical load at which the opening fracture process leads to ultimate fracture, generating the typical vein pattern. The rest of the fracture surface shown in Figure 3-6 resembles the typical dimple pattern of metallic glasses [5-8, 14-17], generated by direct opening without significant prior shear band sliding.

The evidence of shear banding inside the fracture specimen described above (and shown in Figure 3-6) is incongruent with the current understanding of crack tip plasticity [10, 12] in which the crack tip deformation behavior is described by Figure 3-4(b). The origin of the shear bands creating the jagged plastic zone is not clear yet, but this jagged zone has also been observed in other studies [6, 26-28]. “In some regions, these ridges were quite large and ran nominally

parallel to the direction of crack propagation [6, See their Figure 8(a) and 15].” Presumably, this shear band pattern shown in Figure 6 may be due to the morphology of the fatigue pre-crack. As shown in Figure 3-2, the fracture surface generated by fatigue pre-cracking has ridges running parallel to the crack growth direction. Magnified view of these fatigue fracture surface is given in Figure 3-5(a-c) to show that the surfaces have ‘ridge and furrow’ morphology directed normal to the crack front as well as the typical fatigue striations parallel to the crack front. This rough fatigue surface was also observed by Gilbert el al. [6, 17, 29]. Their surface, generated from $\Delta K \sim 10$ MPa·$m^{1/2}$ and $da/dN \sim 10^{-8}$ m/cycle, agrees with the fatigue pre-cracking condition used in this study. The roughness of the fatigue surfaces progressively diminishes with decreasing growth rates [29]. Even at slow growth rates, the ridges running parallel to the crack growth direction were reported [24, 30]. Irregularity due to kinks or steps along the crack front might cause a complex stress state in front of the crack and contribute to the jagged morphology. Indeed, Gao [31] performed an instability analysis of three-dimensional crack problem that included the shape perturbations parallel to the crack front to explain the ridge-like surface features running parallel to the crack growth direction as shown in Figure 3-5(a-c) and Figure 3-6. Gao studied the role of so-called T-stress term on determining crack front morphology. The stress intensity factor is the first term of the Irwin-Williams expansion of the crack tip stress field, and the second term is a constant stress contribution that acts over a longer distance from the crack tip, which is known as T-stress. The T-stress is known to affect the crack growth direction in two-dimensional crack propagation problem [32]. Hess and Dauskardt used Gao’s T-stress analysis to successfully model the surface morphology of fatigue fracture surface of BMG [30]. Additional study is required to understand the shear band pattern in the jagged plastic zone. It is important to note that the specimens without a plastic zone (Figure 3-2(f) and (g), specimens S10-S15) also have

nonplanar ridged fatigue fracture surfaces, which suggests that the nonplanar pre-crack front might be a necessary, but not a sufficient, condition for the formation of a jagged plastic zone.

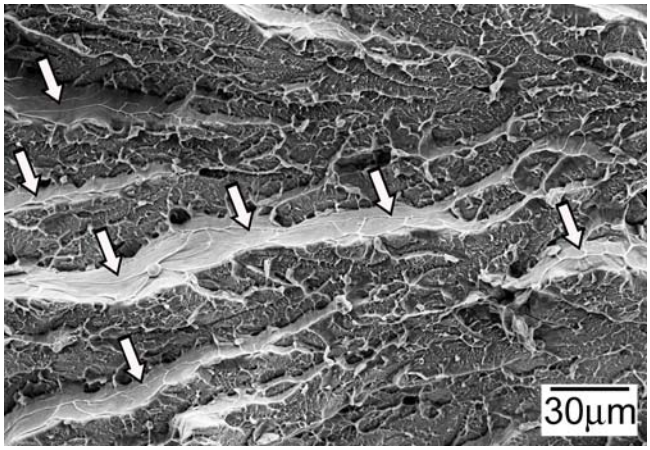

Figure 3-6. Magnified image of squared area in Figure 3-2(c).

3.7 Formation of the shear bands

A shear band that originates at the surface, where plane stress condition dominates, should be distinguished from one that originates inside the specimen, where plane strain condition prevails. This is because the formation of interior shear bands determines the validity of the measurement as plane strain fracture toughness (K_{IC}). Shear bands originating at the surface, which have the typical shape shown in Figure 3-4(c) and (d), propagate in the thickness direction. Figure 3-2(a) shows that these shear planes penetrate almost to the center of the specimen from both sides. It is also evident from Figure 3-2(b)-(c) that the plastic deformation originating at the surface propagates through a significant fraction of the specimen thickness (marked by horizontal arrows in Figure 3-2(b)-(c)). This suggests that the thickness of the specimens used in this study

is insufficient to satisfy the plane strain condition for the highly deformable and tough metallic glasses investigated here. However, the specimens in Figure 3-2(d) and (e) have a relatively small fraction of plane stress fracture surface. For the specimen S7 shown in Figure 3-2(d), the distance of the outermost shear band detectable by scanning electron microscopy (defined by the arrow in Figure 3-4(b)) was 130 μm, and the penetration depth of a surface shear band into the thickness direction (measured in Figure 3-2(d)) was about 160 μm. It is thus plausible that the bulk of the sample is far from the influence of surface shear bands, that is, the bulk of the sample could be under plane strain condition and the jagged pattern could be created by shear bands that originate within the sample, not at the surface.

BMG shear banding (i.e., localized plastic flow) occurs as a consequence of mechanical energy dissipation into the bulk glassy nanostructure, giving rise to local configurational changes that lead to a decrease in the local rigidity (i.e., local softening) [33] and eventual flow percolation along planes of maximum resolved shear stress. It is therefore reasonable to expect that shear bands will evolve within a bulk glassy nanostructure loaded in plain strain, and generation of these interior shear bands is argued here to be the origin of the jagged pattern formation observed in the images of Figure 3-2(b)-(e).

3.8 Effect of loading geometry

From the evidence gathered so far, the fracture process during a fracture test based on bending geometry such as CT and SENB is understood to progress by uniform spreading of a large number of shear bands, resulting in the development of a plastic zone within the test specimen (region “A” in Figure 3-2(a)), and ultimate fracture follows at the instant of critical load. It is reasonable to assume that the extension of the plastic zone (denoted as “L_A” in Figure 3-2(a))

is limited by the nature of the bending geometry of the CT and SENB test methods, as the remaining area (region "B" in Figure 3-2(a)) is loaded under compression during the test. Therefore, the fracture toughness value for Vitreloy 1, which is reported to be in excess of 130 $MPa \cdot m^{1/2}$ by the SENT method [10], may in fact a be a reasonable estimate, because unlike the typical CT and SENB test geometry, the SENT test loading geometry is tension, which would drive the jagged region to cover the entire fracture surface, increasing the critical failure load dramatically resulting in a higher apparent fracture toughness.

3.9 Size of the plastic zone and the validity of K_Q as plane strain fracture toughness (K_{IC})

One of the ASTM size requirements for fracture toughness specimen is given by Equation 3-1, which implies that the size of the plastic zone must be less than 2% of the specimen dimensions in order to obtain a size-independent critical K_{IC} value [34].

$$B, a, (W-a) \geq 2.5 \cdot (K_Q/\sigma_y)^2 \qquad \text{Equation 3-1.}$$

From Equation 3-1, the critical dimension for the specimen S7 with $K_Q=54.6 MPa \cdot m^{1/2}$ and σ_y =1.86GPa is 2.15mm, while the actual sample dimensions are B=2.21mm, a=3.96mm and b_o=4.04mm (initial ligament size, b_0=W-a). Thus, the measured K_Q value for this sample can be regarded as K_{IC} based on the specimen geometry. Other specimens listed below this sample in Table 3-1 (S8 to S15) satisfy the size requirement as well. It is worth noting however that the size of the plastic zone of specimen S7 measured from the image of Figure 3-2(d) (defined as "L_A" in Figure 3-2(a)) is 1.43mm, which is 35% of the initial ligament size b_o. In Figure 3-7, the plastic zone region (L_A) acquired from the fracture surface of each sample is plotted against the process zone size, d, calculated from the measured K_Q and σ_y using Equation 3-2 below [3].

$$d = \frac{K_Q^2}{\pi \sigma_y^2}$$ Equation 3-2.

As seen from the plot in Figure 3-7, the length of the plastic zone region observed in the sample fracture surface correlates well with the plastic zone size estimated from the measured K_Q and σ_y, which suggests that the extent of the jagged pattern propagation is in essence a direct measure of the material fracture toughness.

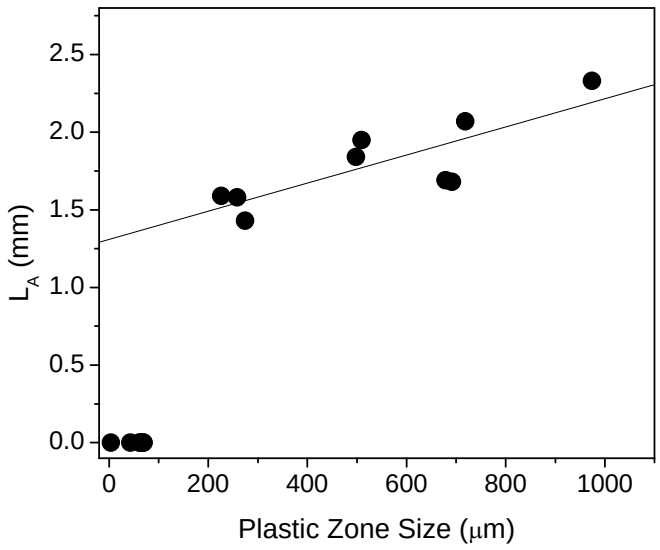

Figure 3-7. Correlation between jagged pattern extension (denoted as L_A in Figure 3-2(a)) and process zone size calculated from Equation 3-2 [3].

3.10 Possible effect of residual stress

Residual stress is known to affect fracture toughness significantly [35]. Residual stress develops during the casting process due to the high temperature gradients which arise during sample cooling and solidification. Compressive stress develops in the surface while tensile stress develops in the interior. The development of the plastic zone could be influenced by the residual stress. Generally, heat treatment below glass transition temperature is used to anneal out residual stress. In this study, the surfaces of all the as-cast test specimens were ground off in an attempt to remove the compressive region of the residual stress and produce a certain degree of relaxation. According to the viscoelastic model of Aydiner et al. [36], an 8.25mm thick Vitreloy 1 plate is estimated to develop up to -230MPa surface compression and +90MPa interior tension. However, an actual experiment by these authors revealed that a copper mold cast piece with the same thickness exhibited only -25 to -30MPa surface compression and +10 to +13 interior tension. In addition, the model suggested significant residual stress decreases with decreasing casting thickness. The casting thickness used in this study is 2.5mm. Their results also indicate that the compressive surface stresses are confined to a relatively thin surface layer. Therefore, removing ~10% of the surface layer is believed to reduce the residual stress to an insignificant level. Indeed, no difference in the size and shape of the plastic zone between as-cast (S7) and annealed (S8) specimens can be observed (See Figure 3-2(d) and (e)). Specimen S13 also exhibits exactly the same surface feature as those of other as-cast specimens (S10-12 and S14). Based on these comparisons, residual stress did not affect the results of this study.

3.11 Conclusions

In summary, in this study, the development of a significant “plastic zone” region during fracture of BMG samples that screens a crack tip was confirmed. The development of this jagged plastic zone region qualitatively and quantitatively explains why BMGs exhibit good toughness despite a near-zero ductility. Fracture surfaces were revealed showing that the roughness and the length of the jagged region adjacent to the pre-crack correlates well with the plastic zone size estimated from the measured fracture toughness values. The propagation of these jagged patterns, the main source of energy dissipation in the sample, was attributed to the ability of shear bands to form and propagate afar from the surfaces where plain strain conditions prevail. By recognizing that the jagged pattern is primarily the result of shear banding, it is understood that fracture toughness is closely related to the ability of the BMG to undergo a certain amount of plasticity prior to failing by catastrophic fracture.

Acknowledgements

The authors would like to thank Prof. G. Ravichandran of GALCIT, Caltech for providing the MTS test system. This work was supported in part by the MRSEC Program of the National Science Foundation under Award Number DMR-0520565.

References

[1] Conner RD, Johnson WL, Paton NE, Nix WD. J Appl Phys 2003;94(2):904

[2] Conner RD, Li Y, Nix WD, Johnson WD. Acta Mater 2004;52:2429

[3] Ashby MF, Greer AL, Scripta Mater 2006;54:321

[4] Peker A, Johnson WL. Appl Phys Lett 1993;63:2342

[5] Lowhaphandu P, Lewandowski JJ. Scripta Mater 1998;38:1811.

[6] Gilbert CJ, Schroeder V, Ritchie RO. Met Mat Trans 1999;30A:1739

[7] Suh D, Dauskardt RH. J Non-Cryst Solids 2003;317:181

[8] Suh D, Dauskardt RH. Ann Chim Sci Mat 2002;27:25

[9] Conner RD, Rosakis AJ, Johnson WL, Owen DM. Scripta Mater 1997;37:1373

[10] Flores KM, Dauskardt RH. Scripta Mater 1999;41:937

[11] Johnson WL. MRS Bulletin 1999;24(10):42

[12] Tandaiya P, Narasimhan R, Ramamurty U. Acta Mater 2007;55:6541

[13] Kim CP, Suh JY, Wiest A, Lind ML, Conner RD, Johnson WL. Scripta Mater 2008;60:80

[14] Xi XK, Zhao DQ, Pan MX, Wang WH, Wu Y, Lewandowski JJ. Phys Rev Lett 2005;94:125510

[15] Lewandowski JJ, Wang WH, Greer AL. Phil Mag Lett 2005;85:77

[16] Gilbert CJ, Ritchie RO, Johnson WL. Appl Phys Lett 1997;71:476

[17] Tatschl A, Gilbert CJ, Schroeder V, Pippan R, Ritchie RO. J Mater Res 2000;15:898

[18] Schuh CA, Hufnagel TC, Ramamurty U. Acta Mater 2007;55:4067

[19] Argon AS, Salama M. Mater Sci Eng 1976;23:219

[20] Hahn GT, Rosenfield AR. Acta Metall 1965;13:293

[21] Schneibel JH, Horton JA, Munroe PR. Metall Mater Trans 2001;32A:2819

[22] Spaepen F, Turnbull D. Scripta Metall 1974;8:563

[23] Leamy HJ, Chen HS, Wang TT. Metall Trans 1972;3:699

[24] Alpas AT, Edwards L, Reid CN. Metall Trans A 1989;20A:1395

[25] Zhang ZF, Eckert J, Schultz L. Acta Mater 2003;51:1167

[26] Davis LA. Metall Trans A 1979;10A:235

[27] Lowhaphandu P, Ludrosky LA, Montgomery SL, Lewandowski JJ. Intermetallics 2000;8:487

[28] Nagendra N, Ramamurty U, Goh TT, Li Y. Acta Mater 2000;48:2603

[29] Gilbert CJ, Lippmann JM, Ritchie RO. Scripta Mater 1998;38:537

[30] Hess PA, Dauskardt RH. Acta Mater 2004;52:3525

[31] Gao H. J Appl Mech 1992;59:335

[32] Cotterell B, Rice JR. Int J Fract 1980;16:155

[33] Harmon JS, Demetriou MD, Johnson WL, Samwer K. Phys Rev. Lett 2007;99:135502

[34] Anderson TL. Fracture Mechanics: Fundamentals and Applications, 1st ed.: CRC Press, 1991. p.431.

[35] Launey ME, Busch R, Kruzic JJ. Acta Mater 2008;56:500

[36] Aydiner CC, Ustundag E, Prime MB, Peker A. J Non-Cryst Solids 2003;316:82

Chapter 4

Effect of annealing on fracture toughness of a Zr-based Be-bearing bulk metallic glass

The $Zr_{44}Ti_{11}Cu_{20}Be_{25}$ alloy with as-cast fracture toughness K_Q = 85 MPa·$m^{1/2}$ is annealed at three different temperatures. Fracture toughness is found to decrease linearly as the annealing temperature decreases and the glass relaxes into lower energy configurations. When annealed at 290°C, 50°C below T_g, the fracture toughness drops to 6 MPa·$m^{1/2}$, while the glassy structure is retained. This annealing embrittlement behavior is discussed together with the change of elastic properties.

4.1 Introduction

The structure of Bulk Metallic Glass (BMG) is bound to relax to some equilibrium liquid state, since the vitrification process called glass transition causes the liquid structure to deviate from its instantaneous equilibrium state at some temperature, termed the glass transition temperature, T_g. As shown in Figure 4-1 [1], the as-cast BMG structure is essentially a frozen liquid structure that has deviated from its equilibrium structure, depicted by dotted line, and is therefore bound to relax back to the equilibrium state via a thermally activated relaxation process.

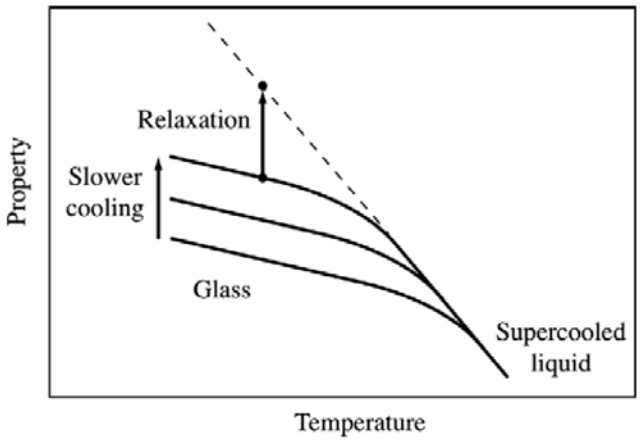

Figure 4-1. Schematic diagram of structural relaxation of BMG taken from Ref. 1. As temperature decreases, the supercooled liquid deviates from the equilibrium behavior at the glass transition point, and this deviation depends on the cooling rate.

This structural relaxation has been known to give rise to embrittlement of the BMG [2-6]. Suh and Dauskardt [2,3] and Launey et al. [6] used plane strain fracture toughness measurement (K_{IC}) to study the embrittlement behavior of Vitreloy 1 ($Zr_{41.2}Ti_{13.8}Cu_{12.5}Ni_{10}Be_{22.5}$) [7] and

Vitreloy 1b ($Zr_{44}Ti_{11}Ni_{10.2}Cu_{9.8}Be_{25}$) [8], respectively. The severe reduction of ductility and fracture toughness has been attributed to the reduction of free volume [2-6]. A reduction of free volume is known to hinder plastic deformation (shear banding) of the BMG, thereby reducing fracture toughness. This is a plausible argument, as suppressing the ability of the BMG to plastically deform leads to lower fracture toughness, as shown in Chapters 2 and 3.

In several recent rheological/ultrasonic studies, it has been demonstrated that a one-to-one correspondence exists between the configurational energy state of the BMG (determined by annealing temperature and time) and the isoconfigurational shear modulus [9-11]. More interestingly though, a functional relationship between viscosity and isoconfigurational shear modulus has been demonstrated in those studies [9-11], which implies a one-to-one correspondence between shear modulus and the activation barrier for configurational hopping, which determines the ability of the BMG to plastically flow.

In this study, the change in fracture toughness of the BMG at different annealing temperature was studied along with the change in isoconfigurational shear modulus and other elastic constants, and the possible origin of the fracture toughness variation is discussed in terms of the ability of the material to overcome the barriers for plastic flow.

4.2 Experimental

The specimen preparation and fracture toughness measurement procedures are described in the previous chapters (Chapters 2 and 3). The $Zr_{44}Ti_{11}Cu_{20}Be_{25}$ alloy, which in the previous chapters is found to have the highest measured as-cast fracture toughness, K_Q=85 MPa·$m^{1/2}$, was annealed at various temperatures around and below the calorimetric T_g for durations adequate to achieve structural relaxation: 350°C for 2 hrs, 320°C for 25 hrs and 290°C for 62 hrs. The

calorimetric glass transition temperature (T_g) of the alloy is 340°C [12]. The thermal properties of all specimens were evaluated using differential scanning calorimetry (DSC) at a heating rate of 20K/min. X-ray analysis was performed on a X'Pert Pro x-ray diffractometer to confirm the amorphous nature of annealed specimens. LEO 1550 VP field emission scanning electron microscope was used for fracture surface observation. The pulse-echo overlap technique with 25MHz piezoelectric transducers was used to measure the shear and longitudinal wave speeds at room temperature enabling calculation of the room-temperature elastic constants. Densities were measured by the Archimedean technique according to the ASTM C693-93.

4.3 Fracture toughness of annealed specimens

Figure 4-2 shows fracture toughness data for the annealed specimens together with that for the as-cast specimen. Fracture toughness is shown to decreases linearly with decreasing annealing temperature as the glass relaxes into lower energy configurations. When the alloy is annealed at 290°C, 50°C below T_g, the fracture toughness drops to 6 MPa·$m^{1/2}$, while retaining its glassy structure. Figure 4-3 shows the X-ray diffraction patterns of all annealed specimens, and reveals that no crystallization is detected in any of the specimens. Figure 4-4 shows the DSC curves acquired from each fracture specimen. Enthalpy recovery around glass transition point is observed for each annealed specimen. The heat of crystallization measured for the as-cast and annealed specimens is 131.6-132.8 J/g (see Table 4-1); this, along with X-ray diffraction verifies that these alloys mostly remain amorphous during annealing.

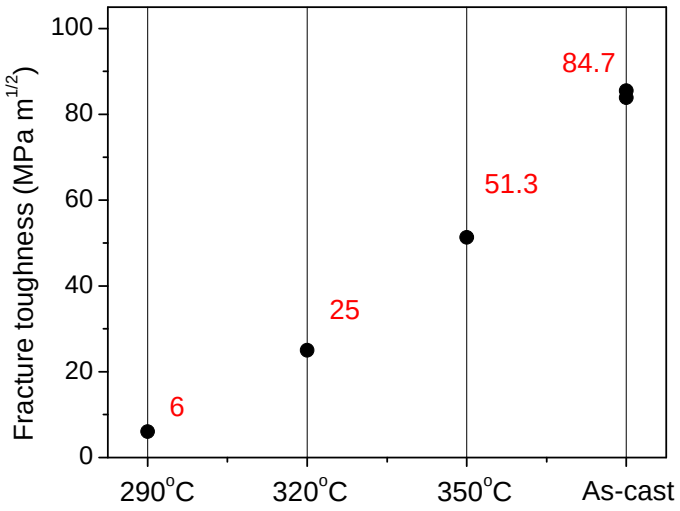

Figure 4-2. Effect of annealing on fracture toughness of $Zr_{44}Ti_{11}Cu_{20}Be_{25}$ alloy.

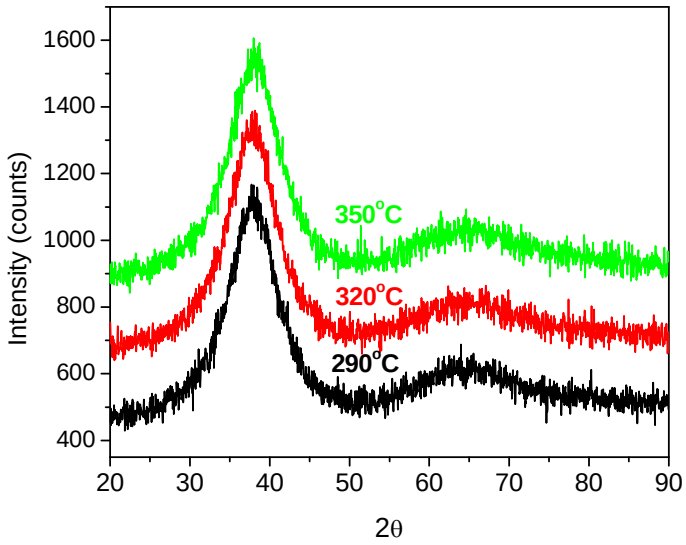

Figure 4-3. X-ray diffraction patterns of specimens annealed at different temperatures.

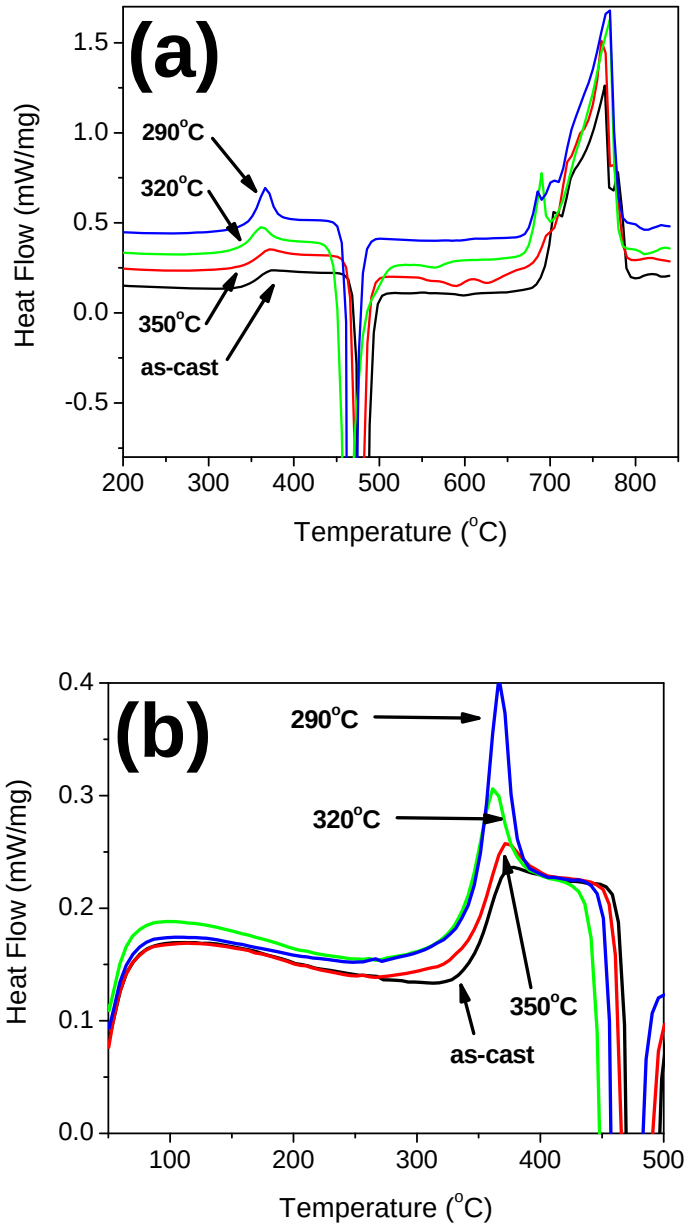

Figure 4-4. DSC curves of as-cast and annealed fracture specimens. (a) overall and (b) magnified images.

Table 4-1. Measured thermal properties of as-cast and annealed specimens.

	T_g (°C)	T_x (°C)	$H_{crystal}$(J/g)	T_m (°C)	H_{fusion}(J/g)
as-cast	340.8	470	132.3	689.5	173.3
350°C	341.3	468.9	131.6	682.2	177.9
320°C	335.6	450.6	132	675.6	182.3
290°C	347.6	458.5	132.8	674.5	187.9

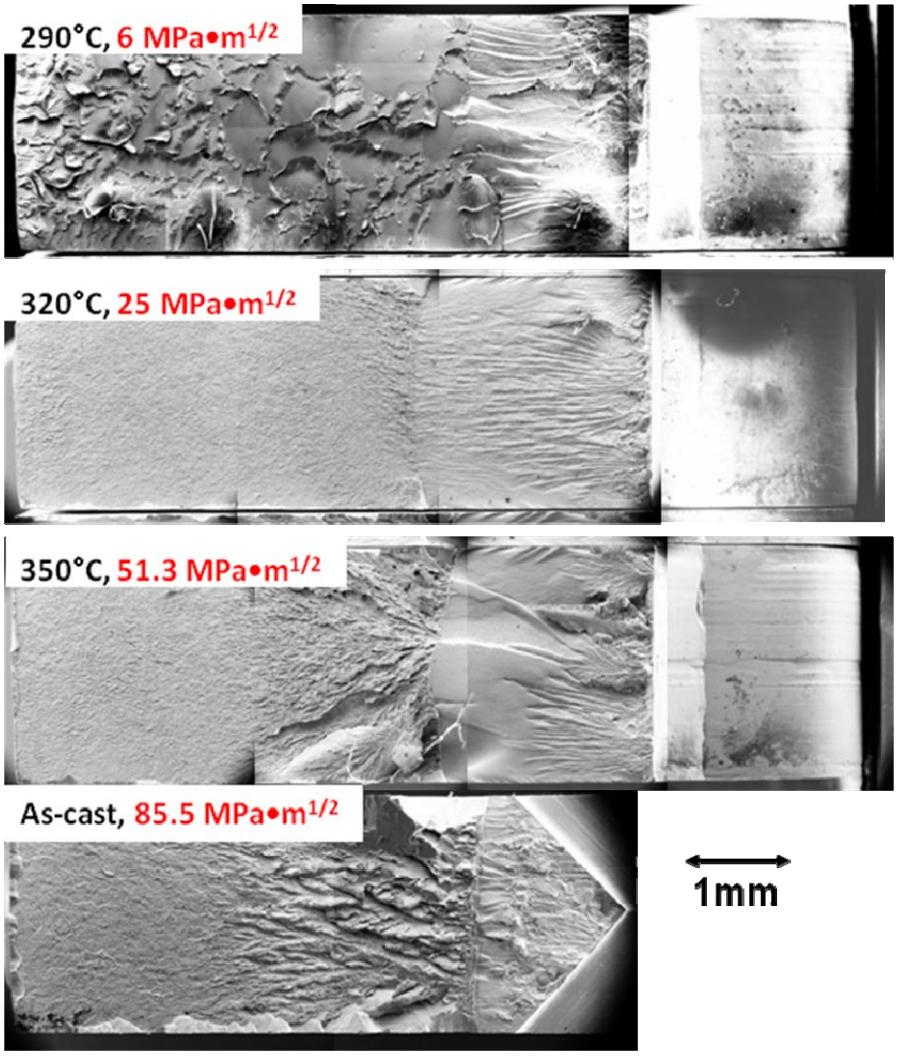

Figure 4-5. Fracture surfaces of annealed and as-cast $Zr_{44}Ti_{11}Cu_{20}Be_{25}$ alloy.

The fracture surfaces shown in Figure 4-5 of the annealed specimens are in agreement with the surface features described in Figure 3-2 in chapter 3. The viewpoint of the observation is described in Figure 3-1(b). The fracture surface of the specimen annealed at 350°C, which has fracture toughness of 51.3 $MPa \cdot m^{1/2}$, has almost the same surface features as shown in Figure 3-2(d). The specimen annealed at 320°C, with K_Q = 25 $MPa \cdot m^{1/2}$, has a uniform fracture surface covered with dimples as shown in Figure 3-2(f) and (g). The fracture surface of the specimen annealed at 290°C is unique. It looks like a cleavage fracture surface having exactly the same features shown by Suh et al [2, 3]. High magnification observation of this surface reveals a uniform dimple structure, with dimples less than 100nm in diameter (see Figure 3-3(d)). These extremely small dimples were also reported by Xi et al [13]. Annealing metallic glass allows the structure to relax into a lower energy configuration, such that it has a higher barrier to flow, and consequently, a reduced resistance to fracture. Considering that the jagged pattern observed in the region adjacent to the notch is primarily the result of shear bands, as discussed in chapter 3, it is conceivable that fracture toughness should be closely related to the ability of the metallic glass to undergo shear and flow.

4.4 Elastic property changes due to annealing of the $Zr_{44}Ti_{11}Cu_{20}Be_{25}$ alloy

The transient structural relaxation behavior of $Zr_{44}Ti_{11}Cu_{20}Be_{25}$ alloy is observed by carrying out consecutive steps of annealing of as-cast specimens. A cast rod of $Zr_{44}Ti_{11}Cu_{20}Be_{25}$ alloy with a diameter of 6 mm is sectioned into disk specimens of height of around 8~9 mm for annealing experiments. The density and elastic properties of each specimen were measured before (as-cast) and after each annealing step. The change in density and elastic properties as a function of annealing time is evaluated by using the same specimen for all annealing steps at each

temperature, in order to maintain consistency with the specimen preparation conditions. The specimens were isothermally annealed under argon in sealed quartz tubes in a tube furnace. For the transient relaxation experiments, two temperatures were considered: 320 and 350°C. These temperatures are also used for the fracture toughness study in the previous section. Two as-cast specimens with a density of 6.027 g/cc were used, having room temperature shear moduli of 35.1 and 35.3 GPa. Because these elastic properties are measured at room temperatures, the effect of thermal expansion has to be considered. The effect of thermal expansion, known as Debye-Grüneisen (DG) effect, is independent of the configurational state. Lind et al. found average DG shear modulus slope $[dG/dT]_{DG}$ = -0.009115 GPa/K and average DG bulk modulus slope $[dB/dT]_{DG}$ = -0.006815 GPa/K for Vitreloy 4 ($Zr_{46.25}Ti_{8.25}Cu_{7.5}Ni_{10}Be_{27.5}$) [10]. Figure 4-6 shows changes of DG corrected elastic properties as a function of annealing time at both temperatures. As-cast shear moduli of both specimens are corrected to be 32.2 and 32.4 GPa with a reference temperature of 340°C, the calorimetric T_g. For the specimen annealed at 350°C, small changes in elastic properties within a range of experimental errors are detected due to the proximity of the annealing temperature to T_g. Although the T_g of this alloy measured at 20K/min DSC scan is 340°C, the specimen in its as-cast state appears to have a lower shear modulus, and hence higher configurational energy, than in the state equilibrated at 350°C. The enthalpy relaxation of the fracture specimen annealed at 350°C, as shown in Figure 4-4(b), also supports that the specimen equilibrated at 350°C is at lower energy configuration than the as-cast specimen. The transition relaxation at 320°C results in more distinct changes in elastic properties. The shear modulus and bulk modulus increase, but Poisson's ratio decreases. Full equilibration is attained in less than 300 minutes. The transient relaxation of shear modulus at this temperature follows the known stretched exponential function [10].

The equilibrium shear moduli at 320°C (593 K) and 350°C (623 K) are 33.8 and 35.5 GPa, respectively, which yields dG_e/dT is -42 MPa/K. This slope is close to that of Vitreloy 4, which is tabulated in Table 4-2 [9]. Dividing dG_e/dT with the slope of the enthalpy with respect to temperature $d\Delta h/dT$, which can be approximated by the change in heat capacity at T_g, Δc_p, the change in the shear modulus with respect to changes in configurational potential energy can be estimated:

$$(dG/d\Delta h) \cong (dG_e/dT)|_{Tg} / \Delta c_p \qquad \text{Equation 4-1.}$$

Although dG/dT of the $Zr_{44}Ti_{11}Cu_{20}Be_{25}$ alloy is close to that of Vitreloy 4, Δc_p, however is smaller, and hence the dependence of isoconfigurational shear modulus on configurational potential energy is as large as that of the Pt-based BMG. According to the cooperative shear model developed by Johnson and Samwer [14], the barrier height for shear flow for a given glass or liquid configuration is proportional to the shear modulus, G. Also, the viscosity of a metallic glass has a unique functional relationship with the shear modulus [9, 11]. This viscosity-shear modulus relationship implies that softening of metallic glass-forming liquids induced by either thermal excitation (by varying temperature) or mechanical deformation (by varying strain rate) is governed by the dependence of isoconfigurational shear modulus on configurational potential energy [9]. Thus, it can be said that the ability of the $Zr_{44}Ti_{11}Cu_{20}Be_{25}$ alloy to soften with increasing configurational energy is comparable to that of Pt-based BMG. Interestingly, the fracture toughness of the Pt-BMG is reported to be $K_Q \cong 80$ MPa·$m^{1/2}$ [15], that is, comparable to the $Zr_{44}Ti_{11}Cu_{20}Be_{25}$ alloy investigated here, which is found to have a fracture toughness of K_Q = 84.7 MPa·$m^{1/2}$. Since the fracture toughness is thought to be closely related to the ability of the BMG to undergo a certain amount of plasticity prior to failing by catastrophic fracture, as discussed in chapter 3, a correlation between $dG/d\Delta h$ and the fracture toughness is therefore conceivable.

Table 4-2. Relationship between calorimetric and ultrasonic data [9].

Metallic Glass-Forming Liquid	Specific Heat Capacity Change, Δc_p (MJ/m^3 K)	dG_e/dT (MPa/K)	$(dG/d\Delta h)\|_{th}$
$Pt_{57.5}Ni_{5.3}Cu_{14.7}P_{22.5}$	2.56	-80	-31.3
$Pd_{43}Ni_{10}Cu_{27}P_{20}$	2.5	-60	-24.0
$Zr_{46.25}Ti_{8.25}Ni_{10}Cu_{7.5}Be_{27.5}$	1.7	-35	-20.6
$Zr_{44}Ti_{11}Cu_{20}Be_{25}$	1.22	-42	-34.4

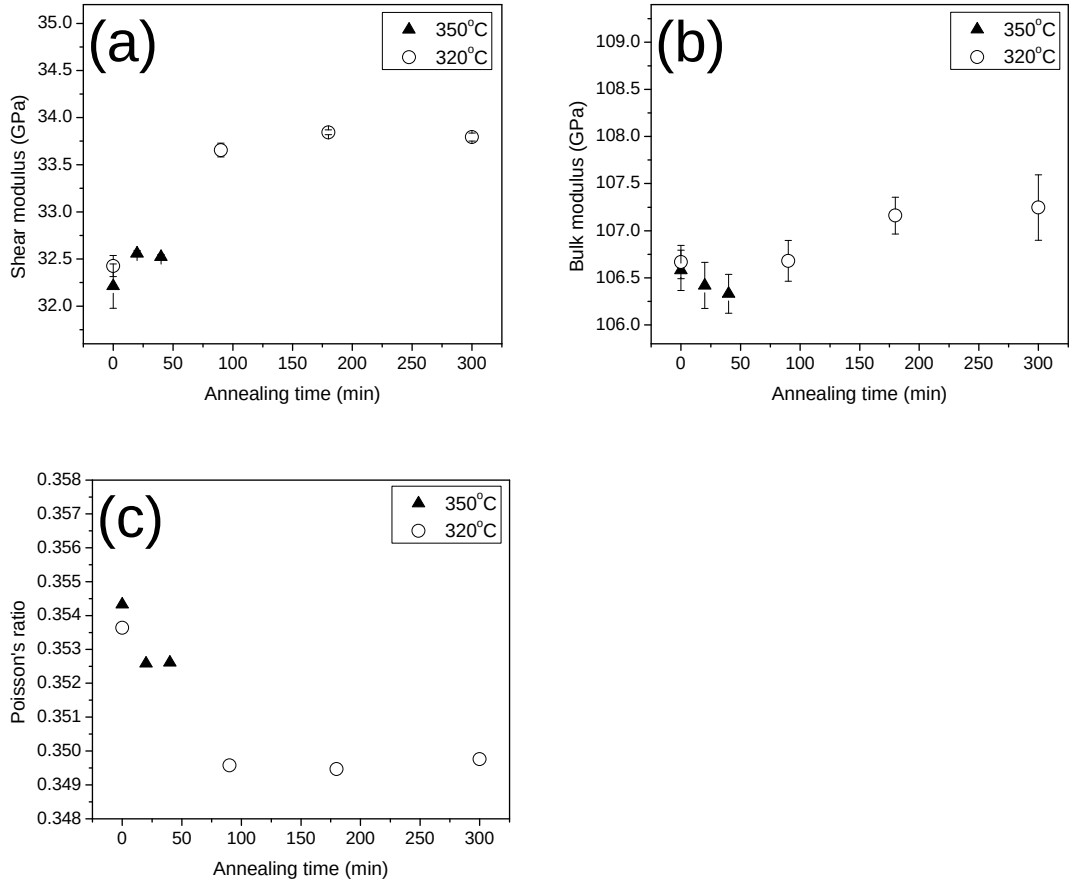

Figure 4-6. Change of elastic constants with annealing at 320 and 350°C.

4.5 Comment on the universal correlation between the energy of fracture and the Poisson's ratio (or the elastic modulus ratio, G/B)

An interesting observation regarding the fracture toughness of the BMG is the dependence of fracture toughness on Poisson's ratio suggested by Lewandowski et al [16]. They proposed a universal correlation between the energy of fracture and the Poisson's ratio (or the elastic modulus ratio G/B) for various metallic glasses. Most importantly, they argued that the fracture toughness data for annealed BMG's fit in the universal correlation perfectly. Their argument attracted a lot of interest because of its conceptual foundation, i.e., fracture process being a competition between plastic flow (determined by shear modulus, G) and fracture opening (determined by bulk modulus, B).

Simple extrapolation of the room temperature elastic properties to the annealed structure at 290°C yields G = 35.1, B = 108.1 GPa and $\nu = 0.346$. As plotted in Figure 4-7, the Poisson's ratio decreases as the annealing temperature decreases, while the bulk and shear moduli increase. Increase of bulk modulus by lowering the equilibration temperature was also observed by Lind et al [10]. The change of the Poisson's ratio (or G/B) in correlation with the fracture energy agrees with the proposed universal correlation. However, it is noteworthy that, as a liquid structure equilibrates to a lower energy state, G/B increases because shear modulus increases more than bulk modulus does, not because of the increase of shear modulus and decrease of bulk modulus. Thus, the embrittlement of a bulk metallic glass as a function of configurational energy state can be attributed to the dominance of the change of shear modulus, which is a direct measure of the barrier height for shear flow for a given glass or liquid configuration, rather than the competition between plastic flow (determined by shear modulus, G) and fracture opening (determined by bulk modulus, B). This argument also agrees with the observation of chapter 3 that the fracture

toughness of the BMG is closely related to the ability of the BMG to undergo a certain amount of plasticity prior to failing by catastrophic fracture.

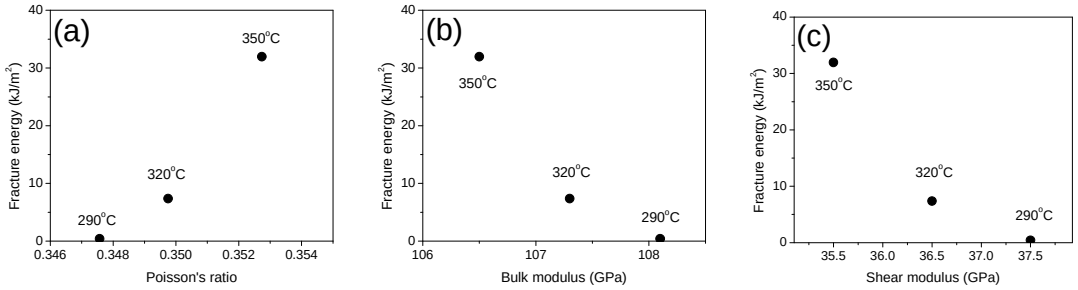

Figure 4-7. Effect of room temperature (a) Poisson's ration, (b) Bulk modulus, and (c) Shear modulus on measured fracture energy (Fracture Energy = $K^2/E/(1-\nu^2)$).

4.6 Conclusions

Fracture toughness decreases as the glass relaxes into lower energy configurations. As a BMG relaxes into lower energy state, shear modulus and bulk modulus increases while Poisson's ratio decreases. Fracture toughness variation in a set of specimens with the same composition can be attributed to the increase of shear modulus based on the cooperative shear model, because the fracture toughness is closely related to the ability of the BMG to undergo a certain amount of plasticity prior to failing by catastrophic fracture.

Acknowledgements

The authors would like to thank Prof. G. Ravichandran of GALCIT, Caltech for providing the MTS test system. This work was supported in part by the MRSEC Program of the National Science Foundation under Award Number DMR-0520565.

References

[1] C.A. Schuh, T.C. Hufnagel and U. Ramamurty, Acta Mater. 55 (2007) 4067.

[2] D. Suh and R.H. Dauskardt, Ann. Chim. Sci. Mat. 27 (2002) 25.

[3] D. Suh and R.H. Dauskardt, J. Non-Cryst. Solids 317 (2003) 181.

[4] U. Ramamurty, M.L. Lee, J. Basu and Y. Li, Scripta Mater. 47 (2002) 107.

[5] P. Murali and U. Ramamurty, Acta Mater. 53 (2005) 1467.

[6] M.E. Launey, R. Busch and J.J. Kruzic, Acta Mater. 56 (2008) 500.

[7] A. Peker, W.L. Johnson, Appl. Phys. Lett. 63 (1993) 2342.

[8] C.C. Hays, C.P. Kim, W.L. Johnson, Appl. Phys. Lett. 75 (1999) 1089.

[9] W.L. Johnson, M.D. Demetriou, J.S. Harmon, M.L. Lind and K. Samwer, MRS Bull. 32 (2007) 644.

[10] M.L. Lind, G. Duan and W.L. Johnson, Phys. Rev. Lett. 97 (2006) 015501.

[11] M.D. Demetriou, J.S. Harmon, M. Tao, G. Duan, K. Samwer and W.L. Johnson, Phys. Rev. Lett. 97 (2006) 065502.

[12] C.P. Kim, J.-Y. Suh, A. Wiest, M.L. Lind, R.D. Conner and W.L. Johnson, Scripta Mater. 60 (2008) 80.

[13] X.K. Xi, D.Q. Zhao, M.X. Pan, W.H. Wang, Y. Wu and J.J. Lewandowski, Phy. Rev. Lett. 94 (2005) 125510.

[14] W.L. Johnson and K. Samwer, Phys. Rev. Lett. 95 (2005) 195501.

[15] J. Schroers and W.L. Johsnon, Phys. Rev. Lett. 93 (2004) 255506.

[16] J.J. Lewandowski, W.H. Wang and A.L. Greer, Phil. Mag. Lett. 85 (2005) 77.

Chapter 5

Fracture toughness characterization of ductile phase containing in-situ BMG composite

Fracture toughness of ductile phase containing in-situ BMG composites is studied. Unlike monolithic BMG's, the composites show stable crack growth and crack arrest. Increasing the volume fraction of ductile dendrite phase with fully developed microstructure, produced by semi-solid processing, increases the amount of energy needed to advance pre-existing cracks. Although a standard evaluation of fracture toughness is not available at this point, due to sample geometry limitations, J-R curve evaluation of the composite reveals significant improvements in fracture toughness, having values that may exceed 136 $MPa \cdot m^{1/2}$.

5.1 Introduction

Although the bulk metallic glasses (BMG's) are known to have high fracture toughness, fracture behavior of monolithic BMG's is unstable. As described in Figure 5-1, a monolithic BMG fracture specimen shows linear behavior almost up to the critical load and, at the moment of crack-initiation, propagation occurs through the entire specimen, fracturing it. However, by introducing a ductile phase, formed homogeneously during cooling inside the BMG matrix [1,2], stable crack growth is achieved [3]. This is a result of the confinement effect of shear band propagation. The recent discovery of a high-toughness monolithic BMG with extremely large supercooled liquid region [4] and subsequent application of this BMG as the matrix for an in-situ composite with controlled microstructural characteristic length scale [5, 6] maximized the toughening effect. In order to characterize this highly-toughened BMG composite material, elastic-plastic fracture mechanics were used to describe the extensive plasticity before the initial crack propagation. In this chapter, fracture tests on the new composite were performed and the elastic-plastic fracture parameter (J) was evaluated.

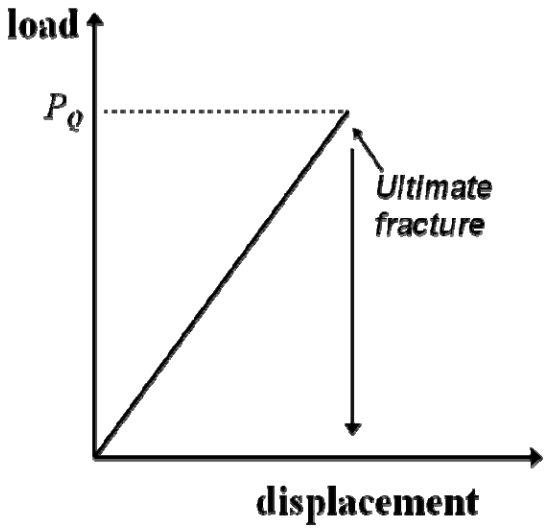

Figure 5-1. Typical fracture behavior of monolithic BMG.

5.2 Ductile phase containing in-situ BMG composite

Recently, significant improvements in the mechanical properties of ductile phase containing in-situ BMG composite have been achieved by Hofmann et al. [5, 6]. Compared to the previous in-situ composites developed by Kim et al. [1, 2], the new BMG composites have the following features:

(1) Increased Ti content and removal of Ni to reduce density. Removal of Ni is also known to enhance fracture toughness of the glass and suppress possible nucleation of brittle intermetallic crystalline phases during processing [4, 7, 8].

(2) A homogeneous and coarsened microstructure. Earlier composites had cooling rate dependent microstructures. Ingots cooled from above the alloy liquidus showed large variations in the overall dendrite length scale and interdendrite spacings. In order to produce a uniform microstructure, cooling from the molten state (T > 1100°C) is interrupted in the temperature of the semi-solid two-phase region (T~ 800-900°C) between the alloy liquidus and solidus temperature. The sample is held isothermally for several minutes in this region. The isothermal hold in the two-phase region allows the nucleation, growth, and coarsening of the ductile dendrite phase to approach thermodynamic equilibrium prior to final quenching. After the isothermal hold, the semi-solid mixture is cooled to vitrify the remaining liquid phase, and obtain a coarse and uniform dendrite distribution.

(3) The length scale of the dendritic phase is on the order of the length scale of deformation in the glass matrix. With softer dendrite phases deforming first and, subsequently initiating shear bands into the BMG matrix, interdendrite distance is limited to below a characteristic length scale [9, 10]. Matching of microstructural length scales to this characteristic length scale limits shear band extension, suppresses shear band opening, and avoids crack development. The composite

microstructure, with softer dendrites, creates short (stable) and dense shear bands rather than long (unstable) and sparse shear bands.

Details of material processing conditions can be found in Ref. 5.

5.3 Experimental (fracture property measurement)

Fracture toughness samples were prepared with various dimensions, limited by the lab-scale size of the water-cooled copper boat used to produce them. An initial notch was made in the middle of one side of the specimen using a wire saw. The diameter of the wire is ~ 170 μm. From the notched end, a pre-crack was generated by fatigue cracking with 5Hz of oscillating load (applied by an MTS hydraulic machine equipped with a 3 point bending fixture with adjustable span distance). The load level was kept at $\Delta K \cong 10 MPa \cdot m^{1/2}$, $K_{min}/K_{max} \cong 0.2$ and the pre-crack was generated until the crack length including the notch length, generated by the wire saw, reached half of the specimen width (45-55% of a specimen width). The pre-cracking process lasts approximately 40,000-100,000 cycles. With this pre-crack, a quasi-static compressive displacement of 0.3mm min^{-1} was applied and the load response of the pre-cracked sample was measured. Evaluation of J and of the J-R curve, by measuring unloading compliance and electrical resistance, were also performed during the test following the procedure described by ASTM E1820.

5.4 Basic concept for elastic and elastic-plastic fracture mechanics

The well known concept of Griffith energy balance was introduced in 1920. With an infinite plate under uniaxial tensile stress containing an interior sharp crack of 2a length (Figure

5-2), the conditions for crack growth will be determined by the following discussion; for an incremental increase in the crack area, potential (strain) energy decrease must be larger than the increase in surface energy by crack extension. This condition is expressed by Equation 5-1. Π, W_s and A refer to potential energy, surface energy and crack surface area, respectively.

$$\frac{dE}{dA} = \frac{d\Pi}{dA} + \frac{dW_S}{dA} = 0 \qquad \text{Equation 5-1.}$$

Potential (strain) energy can be defined as follows,

$$\Pi = \Pi_0 - \frac{\pi\sigma^2 a^2 B}{E} \qquad \text{Equation 5-2.}$$

Π_0 denotes potential (strain) energy of an uncracked plate. The strain energy released by the crack can be estimated by considering the release of strain energy a cylindrical element with diameter of crack length,2a, around the crack such that the energy release term is composed of the $\sigma^2/2E$ (strain energy per unit volume) and $\pi a^2 B$ (volume of cylindrical element around crack). With the formula for surface energy, $W_s=4aB\gamma_s$, Equation 5-1 gives the critical stress for crack growth in a brittle material (Equation 5-3) based on Griffith energy balance.

$$\sigma_f = \left(\frac{2E\gamma_S}{\pi a} \right)^{1/2} \qquad \text{Equation 5-3.}$$

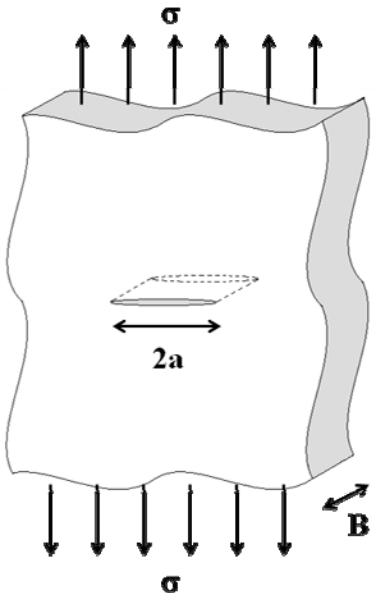

Figure 5-2. Infinite plate with interior crack for Griffith energy balance model.

In 1956, Irwin defined an energy release rate, G, which is a measure of the energy available for an increment of crack extension;

$$G = -\frac{d\Pi}{dA}$$ Equation 5-4.

The energy release rate (G) is the rate of change in potential energy with crack area. Since G is obtained from the derivative of a potential, it is also called the crack extension force or the crack driving force.

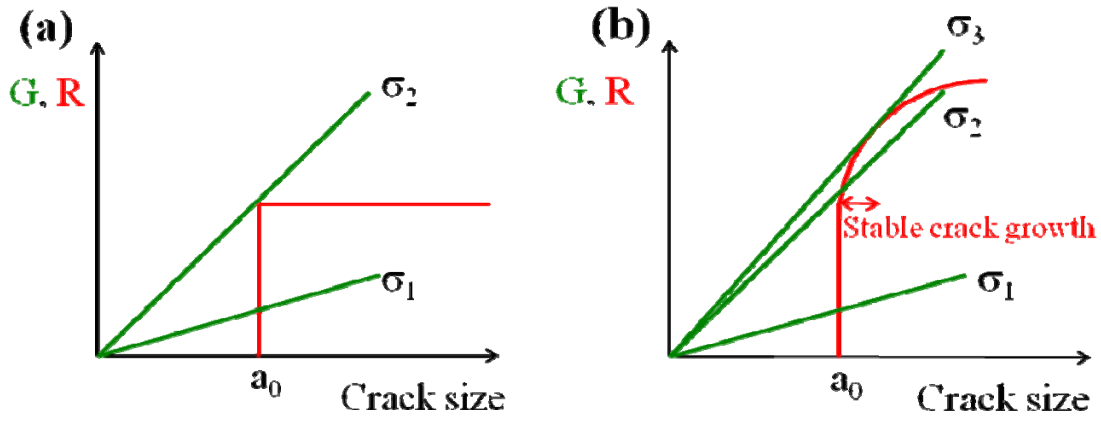

Figure 5-3. Simple resistance curve (R-curve) when (a) material resistance is constant with crack growth and (b) material has rising R-curve.

Figure 5-3 shows simplified fracture resistance curves. For a material having constant resistance with crack growth as shown in Figure 5-3(a), fracture occurs when the stress reaches σ_2. In this case, crack propagation is unstable because the driving force increases with crack growth, but the material resistance remains constant. On the other hand, Figure 5-3(b) shows a rising resistance curve. The crack starts growing when the stress reaches σ_2, but cannot grow further unless the stress increases. Instability occurs when the stress reaches σ_3.

In 1960, Rice introduced a path-independent contour integral for analysis of cracks. He then showed that the value of this integral, which he called J, is equal to the energy release rate (G) in a nonlinear elastic body that contains a crack. Laboratory measurement of J for a growing crack is defined by ASTM E1820. Figure 5-4 shows a typical J-R curve for a ductile material. During loading, crack blunting occurs at the early stage, and the crack starts growing at a critical point. J_{IC} is defined near the initiation of stable crack growth, but it is difficult to define the exact initiation point as in the case of yield stress of tensile testing. Therefore, a 0.2mm offset method

like a 0.2% offset yield stress is used for J_{IC} determination. Initiation toughness (J_{IC}) is important, but it should be also noted that the entire R curve gives a more complete description of fracture behavior.

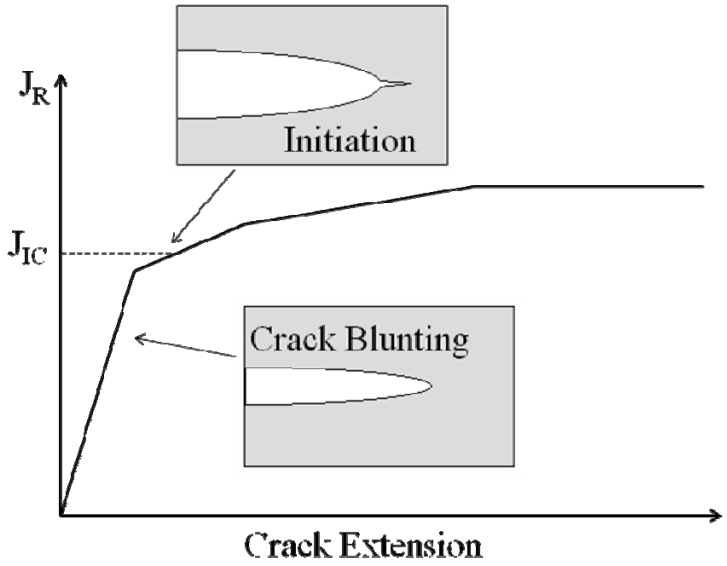

Figure 5-4. Typical J-R curve for a ductile material.

5.5 Load-displacement behavior of composites with different compositions

Figure 5-5 shows load-displacement curves of composites with different compositions. They look different from a typical load-displacement curve of a monolithic BMG introduced in Figure 5-1. Physical properties of these alloys are given in Table 5-1 [5]. The alloy $Zr_{36.6}Ti_{31.4}Nb_7Cu_{5.9}Be_{19.1}$ (DH1) still shows unstable (abrupt) crack propagation behavior, but $Zr_{38.3}Ti_{32.9}Nb_{7.3}Cu_{6.2}Be_{15.3}$ (DH2) and $Zr_{39.6}Ti_{33.9}Nb_{7.6}Cu_{6.4}Be_{12.5}$ (DH3) are different. The curves start to bend over when K= 55-73 $MPa{\cdot}m^{1/2}$, but they appear to have stable crack growth and

clearly have absorbed a large amount of energy. Thus, it is reasonable to consider different fracture parameter such as energy terms rather than the stress term, like stress intensity factor (K). A simple calculation of energy consumption for crack growth gives a rough idea of resistance of each composite against crack growth. As given in Table 5-2, overall energies dissipated during crack propagation process are 0.60, 1.06 and 1.38 Joules for DH 1, 2 and 3, respectively. Dividing these energy values by the areas of newly generated cracks (amount of crack propagation, 3.0, 2.3 and 1.6 mm) yields energy consumed per unit area of fracture surface, G = 77, 178 and 341 kJ/m^2. Although these are rough estimations, simple conversion to stress intensity factor (K) using relation for plane strain condition, $G= K^2/E \times(1-\nu^2)$, and elastic properties given in Table 5-1 calculates K values of 87, 124 and 173 $MPa \cdot m^{1/2}$, respectively. This estimation is not rigorous because it does not differentiate crack initiation stage from crack propagation stage. Moreover, the plane strain condition is not satisfied here, due to limitations in the sample's thicknesses, which will be discussed later. Nevertheless, the fracture behavior of DH 1, 2 and 3 composite alloys shows the clear toughening effect of the ductile dendrite phase.

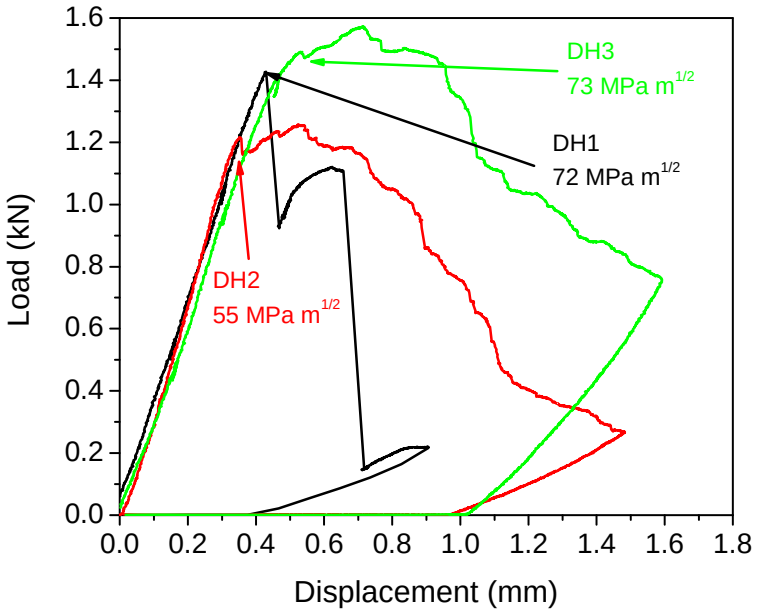

Figure 5-5. Load-displacement curves of composites with different compositions.

Table 5-1. Physical properties of different composites [5]. Dendrite volume fraction, yield stress, Young's modulus and Poisson's ratio.

Alloy	Dend. vol. frac. (%)	σ_y (MPa)	E (GPa)	ν
DH1 ($Zr_{36.6}Ti_{31.4}Nb_7Cu_{5.9}Be_{19.1}$)	42	1474	84.3	0.371
DH2 ($Zr_{38.3}Ti_{32.9}Nb_{7.3}Cu_{6.2}Be_{15.3}$)	51	1367	79.2	0.373
DH3 ($Zr_{39.6}Ti_{33.9}Nb_{7.6}Cu_{6.4}Be_{12.5}$)	67	1096	75.3	0.376

Table 5-2. Dimensions of fracture test specimens and fracture test results.

a_0 denotes initial pre-crack length (notch + pre-crack).

Typical 3-pt bending specimen is illustrated in Figure 3-1.

G = (Area of load-disp. curve)/(thick × Δa) and $G = K^2/E \times (1-\nu^2)$.

Alloy	thick (mm)	a_0 (mm)	width (mm)	span (mm)	Area of load-disp. curve (J)	crack extension Δa (mm)	G (kJ/m^2)	K ($MPa \cdot m^{1/2}$)
DH1 ($Zr_{36.6}Ti_{31.4}Nb_7Cu_{5.9}Be_{19.1}$)	2.58	4.5	8.3	31.75	0.6	3	77	87
DH2 ($Zr_{38.3}Ti_{32.9}Nb_{7.3}Cu_{6.2}Be_{15.3}$)	2.63	3.8	7.8	31.75	1.06	2.3	178	124
DH3 ($Zr_{39.6}Ti_{33.9}Nb_{7.6}Cu_{6.4}Be_{12.5}$)	2.5	4.4	8.3	31.75	1.38	1.6	341	173

5.6 Comparison of two composites with different compositions

5.6.1 Crack growth estimation by unloading compliance

$Zr_{39.6}Ti_{33.9}Nb_{7.6}Cu_{6.4}Be_{12.5}$ (DH3) and $Zr_{37.5}Ti_{32.2}Nb_{7.2}Cu_{6.1}Be_{17}$, an alloy with a composition that falls in between DH1 and DH2 (this alloy is denoted as DH2* hereafter), are compared. DH1-3 alloys are designed based on the formula $(Zr_{45.2}Ti_{38.8}Ni_{8.7}Cu_{7.3})_{100-X}Be_X$ with x=19.1, 15.3 and 12.5 for DH1, DH2 and DH3, respectively. As the Be content, x, decreases, one obtains an increasing volume (or molar) fraction of dendrite phase in a glass matrix, as shown in Table 5-1. DH1-3 alloys partition by volume fraction into 42%, 51% and 67% dendritic phase in a glass matrix, respectively [5]. DH2* has x=17, which places in between 15.3 and 19.1. Therefore, DH2* is expected to have a dendrite fraction between 42 and 51%.

Since the fracture properties estimated by the overall energy consumption cannot differentiate different stages of crack initiation and propagation, it is necessary to monitor the crack growth behavior (position of the crack tip or crack length) during loading. Practical and well known methods are ‘unloading compliance’ and ‘potential drop’ methods [11]. The

'unloading compliance' method was used for this discussion and 'potential drop' method using typical 4-point probe electrical resistance measurement will be used and discussed in the latter part of this chapter. Unloading lines are used for estimating 'crack length' based on the formula given by ASTM E1820 (section A1.4.3):

$$a/W = 0.999748 - 3.9504u + 2.9821u^2 - 3.21408u^3 + 51.51564u^4 - 113.031u^5$$

Equation 5-5.

where :

$$u = \frac{1}{\left[\frac{BWEC}{S/4}\right]^{1/2} + 1}$$

Equation 5-6.

$C = (\Delta v_m/\Delta P)$ on an unloading/reloading sequence,

v_m= crack opening displacement at notched edge (in this study, ram displacement is used instead of crack opening displacement).

a = crack length, B = specimen thickness, W = specimen width, E = Young's modulus, and S = span distance of 3-pt bending fixture.

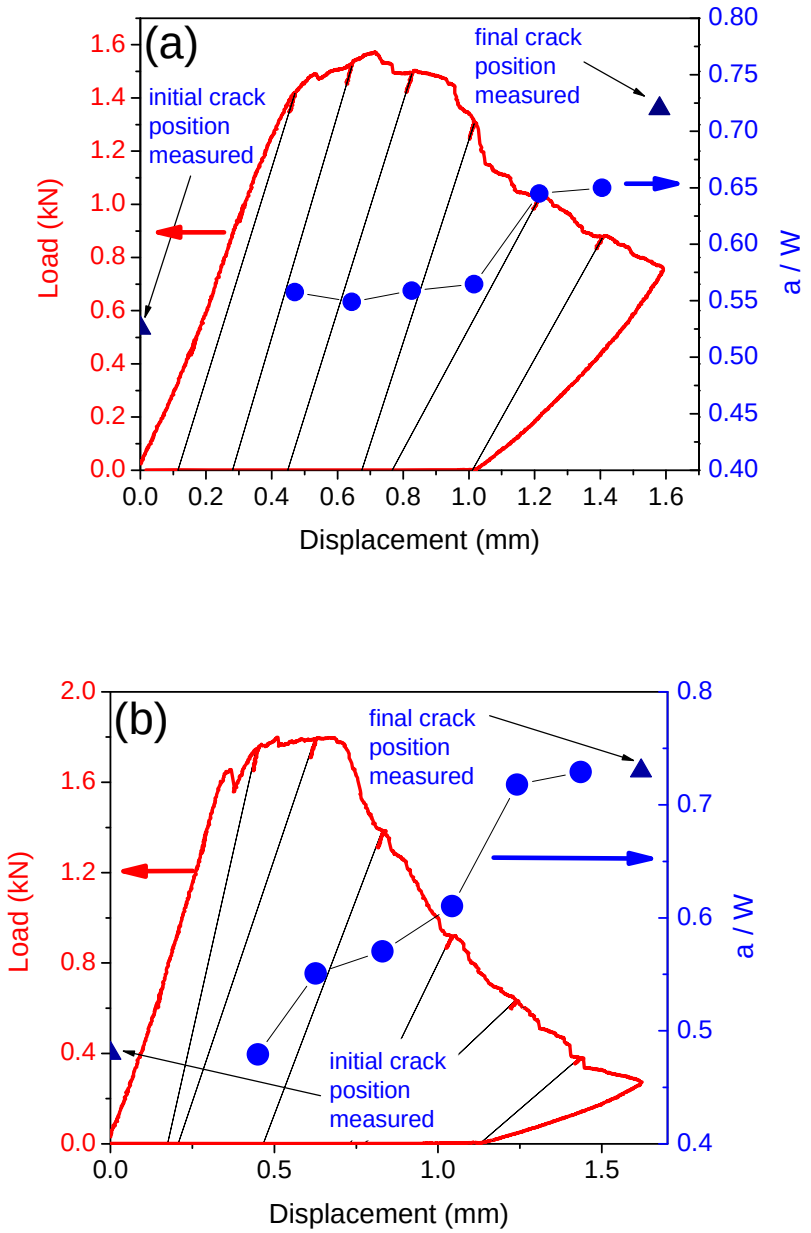

Figure 5-6. Crack length estimation by unloading compliance on (a) DH3 and (b) DH2*. Triangles show crack position measured before and after fracture test.

Figure 5-6 shows results of crack length estimation using the formula given by Equation 5-5 and 5-6. Compared to the actual crack propagation measured before and after fracture test (shown by triangles in the figures), it underestimates the crack propagation of DH3 as shown in Figure 5-6(a), but shows relatively good agreement for DH2* specimen shown in Figure 5-6(b).

The slopes of unloading lines decrease as the crack front advances. A prominent difference between these two specimens is the initiation of slope change. The slope of DH3 starts decreasing later than DH2* does which implies that the crack starts to grow much later than the bending-over point in load-displacement curve in DH3. Since it appears that the bending-over of the load-displacement curve is not from crack advancing but from crack blunting, elastic-plastic fracture mechanics is required to characterize the fracture behavior of these composites. Although the number of unloading lines used for these specimens are not enough to satisfy ASTM 1820 for J-R curve method, a rough estimation of initiation J_Q (J_{IC} in case of plane strain condition) using this unloading compliance method gives ~≥260 kJ/m^2 for DH3 and ~120 kJ/m^2 for DH2*, which can be converted to stress intensity factor (K) for comparison purpose, K~≥ 151 and ~105 MPa·m$^{1/2}$, respectively. These numbers are similar to the numbers calculated from the concept of overall energy consumption. In order to confirm the high toughness of the composites, a more refined evaluation of J is necessary.

5.6.2 Difference in the microstructure

Microstructures of both specimens also agree with the observation stated above. Figure 5-7 compares low magnification images of two fractured specimens: DH3 and DH2*. It is clear that the crack advances more in DH2* than in DH3. Figure 5-8 shows areas where the advancing cracks are arrested (indicated by an arrow on the top of each image). Heavy deformation around

the crack appears to make the specimen's surface look significantly rough. Apparently, the microstructure of DH2* (Figure 5-8(b)) has larger dendrites and larger interdendrite spacing. Small crack openings are also observed in DH2*, which are not observed in DH3. The difference looks more apparent in Figure 5-9. Both Figure 5-9(a) and (b) look almost identical in dendrite size and interdendrite spacing, but they have different magnification: 6000× for DH3 in Figure 5-9(a) and 3000× for DH2* in (b). So the shear bands in DH2* run about twice as far as those in DH3 specimen. Moreover, a shear band located on center of Figure 5-9(b) runs particularly longer than the others and appears to develop into a crack. This observation is fairly consistent with the designing strategy, "matching characteristic length scale", introduced by Hofmann et al. [5].

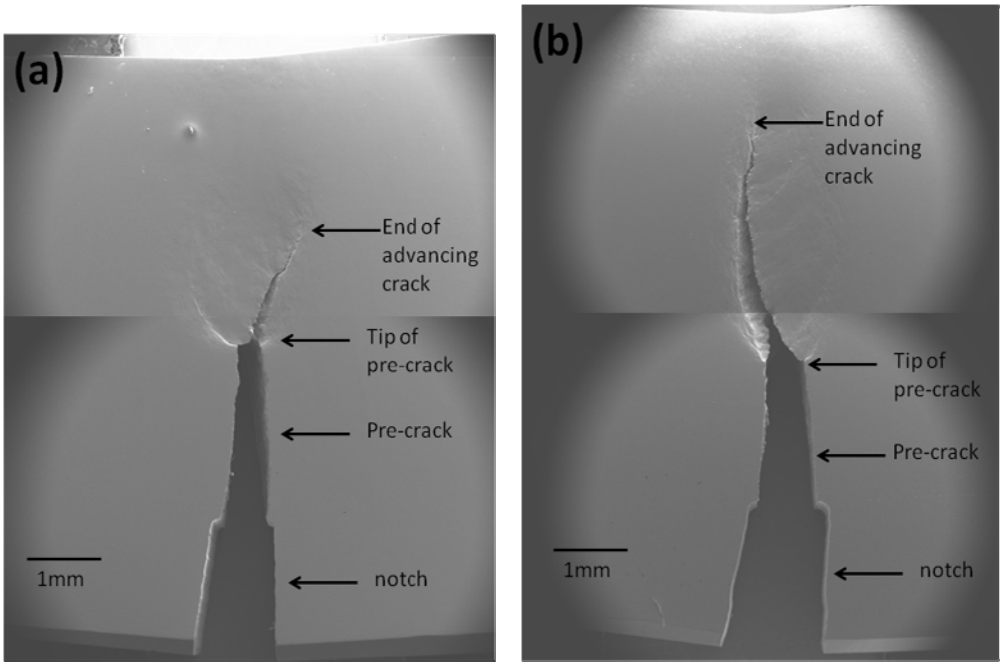

Figure 5-7. Low magnification images of fracture specimens. (a) DH3 and (b) DH2*.

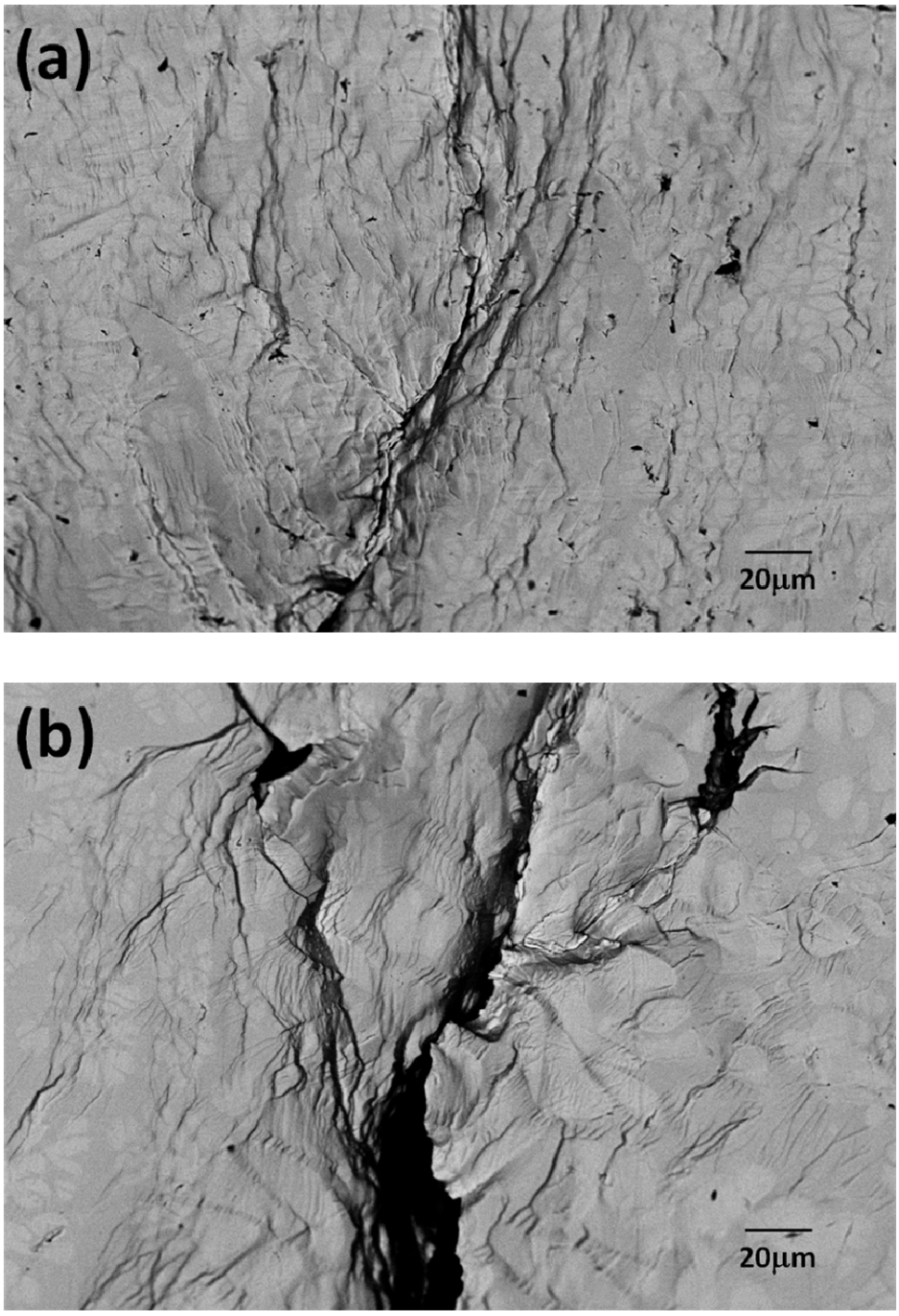

Figure 5-8. Back-scattered electron images of the surfaces of fracture specimens near the crack arresting point. (a) DH3 and (b) DH2*. Both images are taken by 1000× magnification.

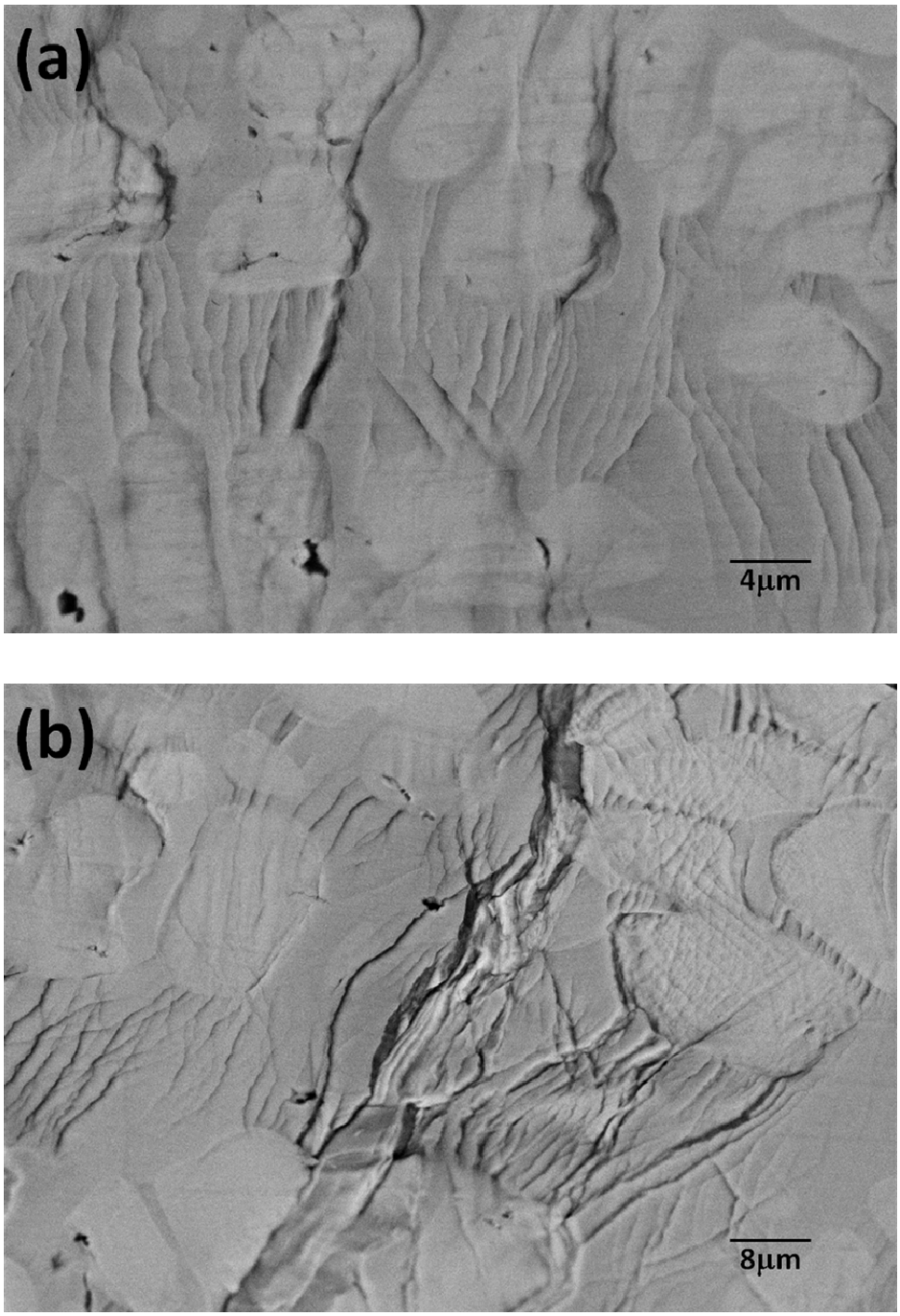

Figure 5-9. Magnified back-scattered electron images of the surfaces of fracture specimens near crack arresting point. (a) DH3 with 6000× magnification and (b) DH2* with 3000× magnification.

5.7 J-R curve evaluation with thicker specimens

It is apparent that the fracture tests performed above do not satisfy the standard requirement for specimen size. However, the current equipment for material production limits specimen size to below 5 mm in thickness. (A new setup for larger specimen production has been completed recently and additional fracture toughness evaluation is ongoing by a fracture mechanics research group in Lawrence Berkeley Laboratory.) Although the current 5 mm thickness is not enough to support a case that the material has fracture toughness of 170 $MPa \cdot m^{1/2}$, it's still worth exploring the fracture toughness of specimens with varying thicknesses. In addition to the 2.5 mm thick specimen measured above, 4.18, 4.86 and 5.21 mm thick specimens of DH3 ($Zr_{39.6}Ti_{33.9}Nb_{7.6}Cu_{6.4}Be_{12.5}$) have been evaluated. Both 4.18 and 4.86 mm thick specimens have been prepared by arc-melting and semi-solid processing in a copper boat, but due to the size limitation of the copper boat equipment, a 5.21 mm thick specimen was created directly from the arc-melter, without additional processing.

J-R curve measurement for these specimens is performed following the guideline given by the ASTM standard. As a verification tool for the crack length estimation by unloading compliance, electrical resistance measurement (potential drop) is utilized. Electrical resistance increases as cracks grow since the crack growth reduces the effective area through which electric current flows. Figure 5-10 shows a schematic diagram of potential drop measurement.

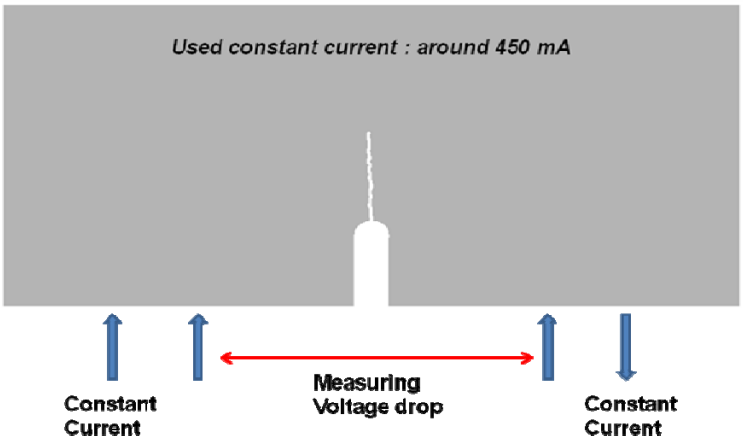

Figure 5-10. Potential drop (electrical resistance) measurement setup for fracture specimen.

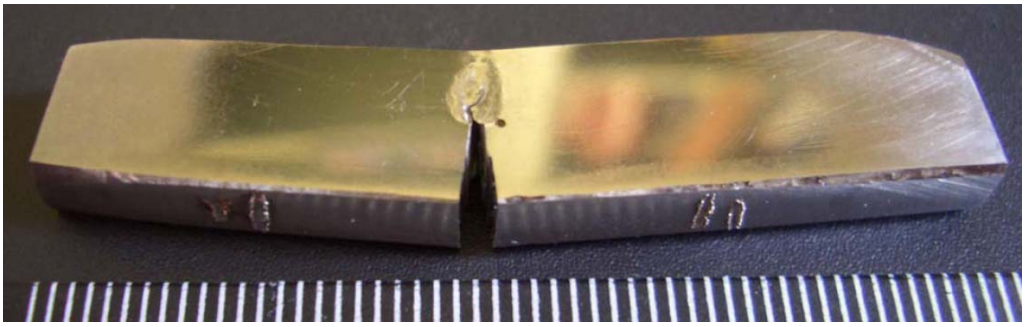

Figure 5-11. 5.21 mm thick specimen of DH3 ($Zr_{39.6}Ti_{33.9}Nb_{7.6}Cu_{6.4}Be_{12.5}$) after test.

5.7.1 Evaluation procedure for 5.21 mm thick specimen

Figure 5-11 shows the overall deformation of a 5.21 mm thick specimen of DH3 ($Zr_{39.6}Ti_{33.9}Nb_{7.6}Cu_{6.4}Be_{12.5}$) after fracture testing. The specimen width (W) was 9.3 mm and initial crack length (a_0) was 4.85 mm, thus the initial ligament size was $b_0 = W-a_0 = 9.3-4.85 = 4.45$ mm. The span distance for the 3-pt bending fixture is 38.1 mm. This specimen is too thick for the copper boat so semi-solid processing was not done. In other words, this is a specimen directly

from the arc-melter. As shown in Figure 5-11, about 2 mm of crack opening is obtained by the fracture test and large area of plastic zone is observed. It should be noted that, in spite of the large amount of deflection in this specimen, the crack advanced only about 2.5 mm before stopping.

Figure 5-12 is a load-displacement curve with unloading lines. The slope of the unloading lines decreases as the crack advances. In Figure 5-13, the crack position estimated by unloading compliance is shown by a curve connected with circles and voltage drop through the specimen under constant current flow is shown by a line. Crack length curves acquired by unloading compliance method and voltage drop method appear identical in shape. Additionally, the estimated crack position is close to the numbers measured by calipers before and after the test, which are shown by triangles in the plot. Therefore, it is reasonable to use these estimated numbers for the following J-calculation.

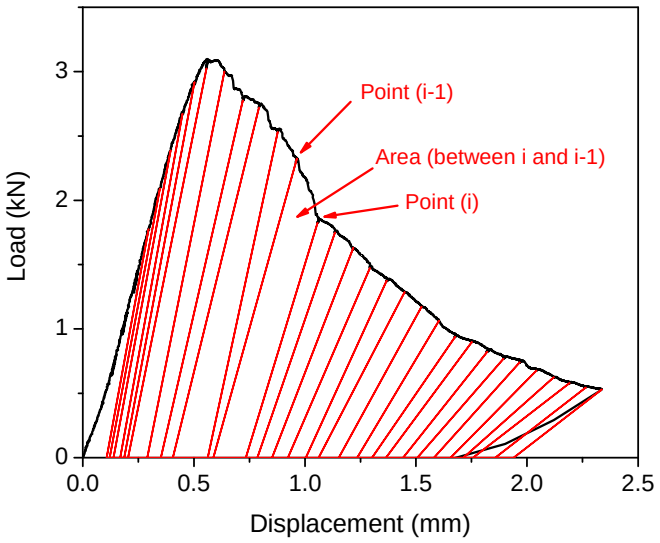

Figure 5-12. Load-displacement curve and unloading compliance lines from 5.21 mm thick specimen.

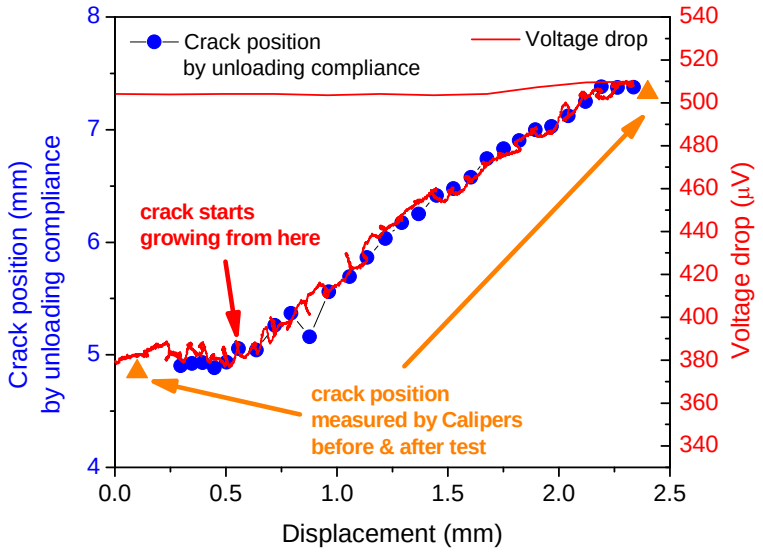

Figure 5-13. Crack position estimation by unloading compliance which is agreeing with crack position before and after test measured by calipers and potential drop line in overall shape.

Using the incremental formula given by Equations 5-7, 8 and 9, elastic and plastic component of the J parameter is calculated. Definitions of point (i) and point (i-1) are given in Figure 5-12.

$$J_{(i)} = J_{elastic\,(i)} + J_{plastic\,(i)}$$ Equation 5-7.

$$J_{elastic\,(i)} = \frac{\left(K_{(i)}\right)^2\left(1-\nu^2\right)}{E}$$ Equation 5-8.

$$J_{plastic\,(i)} = \left[J_{plastic\,(i-1)} + \left(\frac{2}{w-a_{(i-1)}} \right)\left(\frac{Area(between\ \ i\ and\ i-1)}{B} \right) \right] \cdot \left[\frac{w-a_{(i)}}{w-a_{(i-1)}} \right]$$

Equation 5-9.

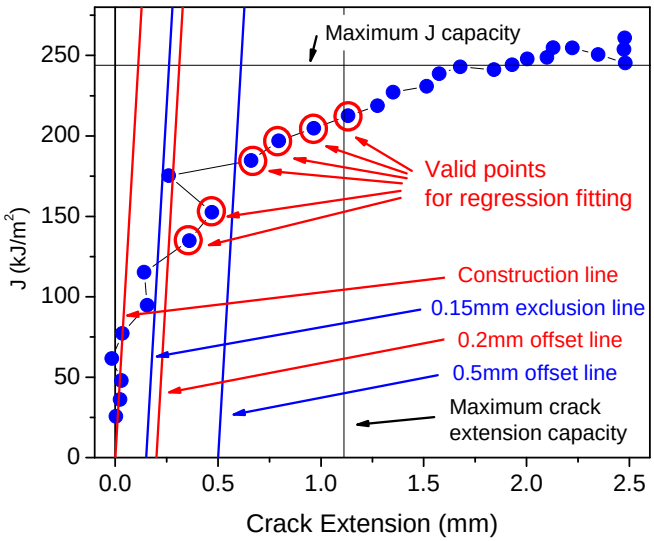

Figure 5-14. J-R curve for 5.21 mm thick specimen.

The calculated J parameter is plotted in Figure 5-14 as a function of crack extension ($\Delta a = a - a_0$).The following conditions limit the validity of J-R curve acquired.

(1) The unload/reload sequences should be spaced with the displacement interval not to exceed 0.01 W. This condition is satisfied for this specimen and the following 4.18 and 4.86 mm thick specimens.

(2) The maximum J-integral capacity for a specimen is given by the smaller of the following:

$$J_{max} = \frac{b\sigma_Y}{20} \quad \text{or} \quad \text{Equation 5-10.}$$

$$J_{max} = \frac{B\sigma_Y}{20} \quad \text{Equation 5-11.}$$

For this specimen, Equation 5-10 applies with J_{max} = 244 kJ/m^2 (indicated in Figure 5-14).

(3) The maximum crack extension capacity for a specimen is given by the following Equation 5-12.

$$\Delta a_{\max} = 0.25 \cdot b_0 \qquad \text{Equation 5-12.}$$

The maximum crack extension capacity for this specimen is 1.11 mm (shown in Figure 5-14).

With the restrictions given above, the following procedure is taken to determine J_Q using the acquired J-R curve shown in Figure 5-14.

(1) Plot a construction line in accordance with the following equation: (plotted in Figure 5-14)

$$J = 2\,\sigma_Y\,\Delta a \qquad \text{Equation 5-13.}$$

(2) Then draw an exclusion line parallel to the construction line intersecting the abscissa at 0.15 mm (drawn in Figure 5-14). Draw a second exclusion line parallel to the construction line intersecting the abscissa at 1.5 mm. This 1.5 mm exclusion line is not shown in Figure 5-14 because Δa_{max} (= 1.11 mm) is less than 1.5 mm. Data points that don't fall inside the area enclosed by these two exclusion lines capped by J_{max} (Equation 5-10 or 11) should be thrown away.

(3) At least one point shall lie between the 0.15 mm exclusion line and a parallel line with an offset of 0.5 mm from the construction line. The 5.21 mm thick specimen has 2 points in this region (Figure 5-14).

(4) At least one point shall lie between this 0.5 mm offset line and 1.5 mm exclusion line. The 5.21 mm thick specimen has 4 points in this region (Figure 5-14).

(5) Using the data points which conform to the requirement stated above (6 data points for this specimen), determine a linear regression line of the following form:

$$\ln J = \ln C_1 + C_2 \ln\left(\frac{\Delta a}{k}\right)$$ Equation 5-14.

where k=1.0 mm.

(6) The intersection of the regression line (Equation 5-14) with the 0.2 mm offset line defines J_Q.

122.2 kJ/m^2 is acquired for this specimen as shown in Figure 5-15.

Qualification of J_Q as J_{IC}, a size independent value of fracture toughness, requires following three conditions to satisfy.

(1) Thickness B > 25 J_Q/σ_Y.

For this specimen, 25 J_Q/σ_Y = 2.79 mm, and the specimen thickness 5.21 mm is larger than 2.79 mm, thus this condition is satisfied.

(2) Initial ligament, b_0 > 25 J_Q/σ_Y.

Initial ligament size, 4.45 mm is also larger than 2.79 mm, thus this condition is satisfied.

(3) Regression line slope – the slope of the power law regression line, dJ/da, evaluated at Δa_Q should be less than σ_Y. For this specimen, slope of regression line at Δa_Q is 187 MPa which is smaller than σ_Y, 1096 MPa. This condition is satisfied.

Therefore, the measured J_Q can be regarded as J_{IC}: J_{IC} = 122.2 kJ/m^2. And, the stress intensity factor converted from J_{IC} is, K_{JIC} = 103.5 MPa·m$^{1/2}$.

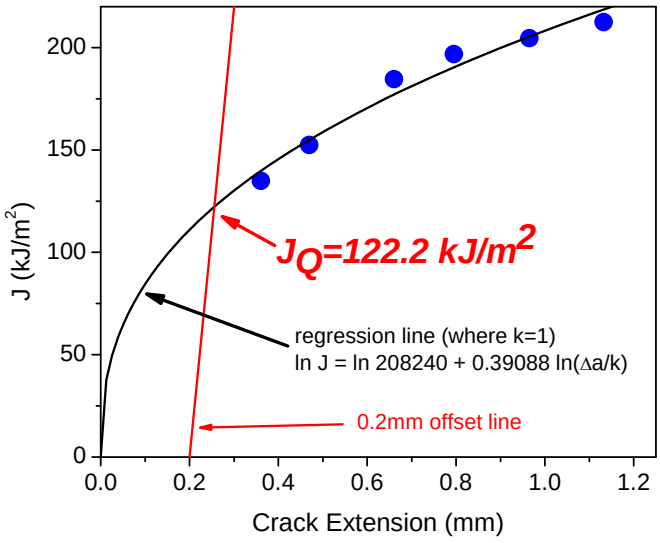

Figure 5-15. Regression curve fitting for J_Q determination of 5.21 mm thick specimen.

5.7.2 Evaluation with 4.18 and 4.86 mm thick specimens

Figure 5-16 shows an overall image of 4.18 and 4.86 mm thick DH3 ($Zr_{39.6}Ti_{33.9}Nb_{7.6}Cu_{6.4}Be_{12.5}$) specimens after testing. Both specimens are prepared by arc-melting and semi-solid processing in a copper boat. The 4.18 mm thick specimen has 34.925 mm of span distance (S), 9.19 mm of specimen width (W) and 4.30 mm of initial crack length (a_0). For this sample, S = 38.1 mm, W= 9.38 mm and a_0 = 5.13 mm. About 2 mm of crack opening is obtained by each fracture test and a large area of plastic zone is observed like that of the 5.21 mm thick specimen. The cracks advance only about 1.8 and 1.5 mm, respectively for the 4.18 and 4.86 mm thick specimens.

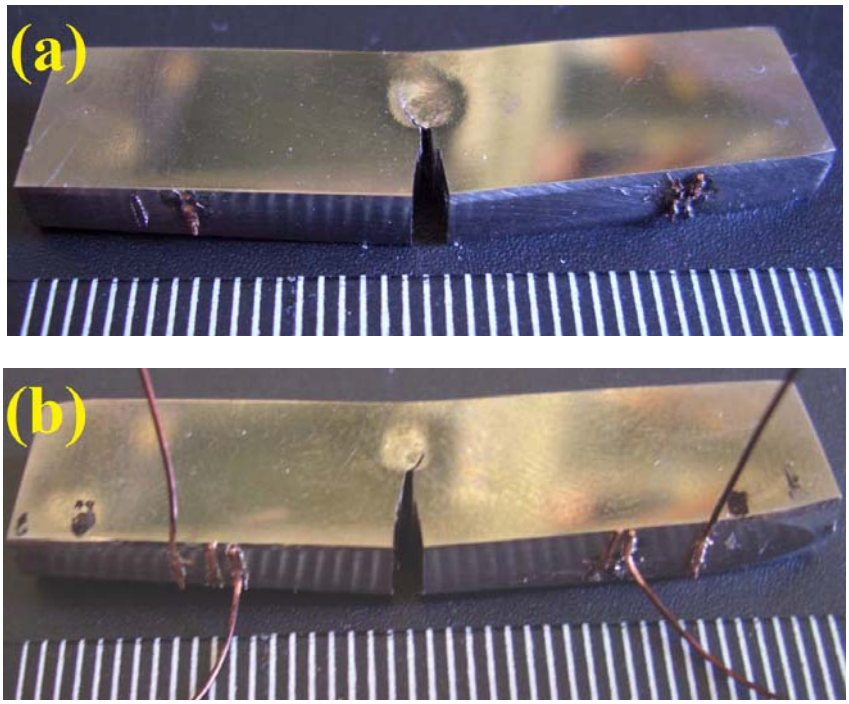

Figure 5-16. (a) 4.18 and (b) 4.86 mm thick DH3 ($Zr_{39.6}Ti_{33.9}Nb_{7.6}Cu_{6.4}Be_{12.5}$) specimens after testing.

Crack length curves acquired by the unloading compliance method and voltage drop method look identical in overall shape, as shown in Figure 5-17. Additionally, the estimated crack positions are close to the numbers measured by calipers before and after test.

J-R curves are shown in Figure 5-18 for both specimens. Due to the extensive deformation before crack extension, J curves show a steep increase passing the maximum J capacity (J_{max}) at the early stage of deformation. J_{max} is defined to be 229 and 266 kJ/m^2 for the 4.18 and 4.86 mm thick specimens, respectively. The critical J (J_Q) may be approximated by intersecting point with 0.2 mm offset line: 326 and 321 kJ/m^2. These two J_Q values are almost identical and represent 170 and 168 MPa·m$^{1/2}$ of stress intensity factors. But, these are not valid numbers for standard plane strain J_{IC}.

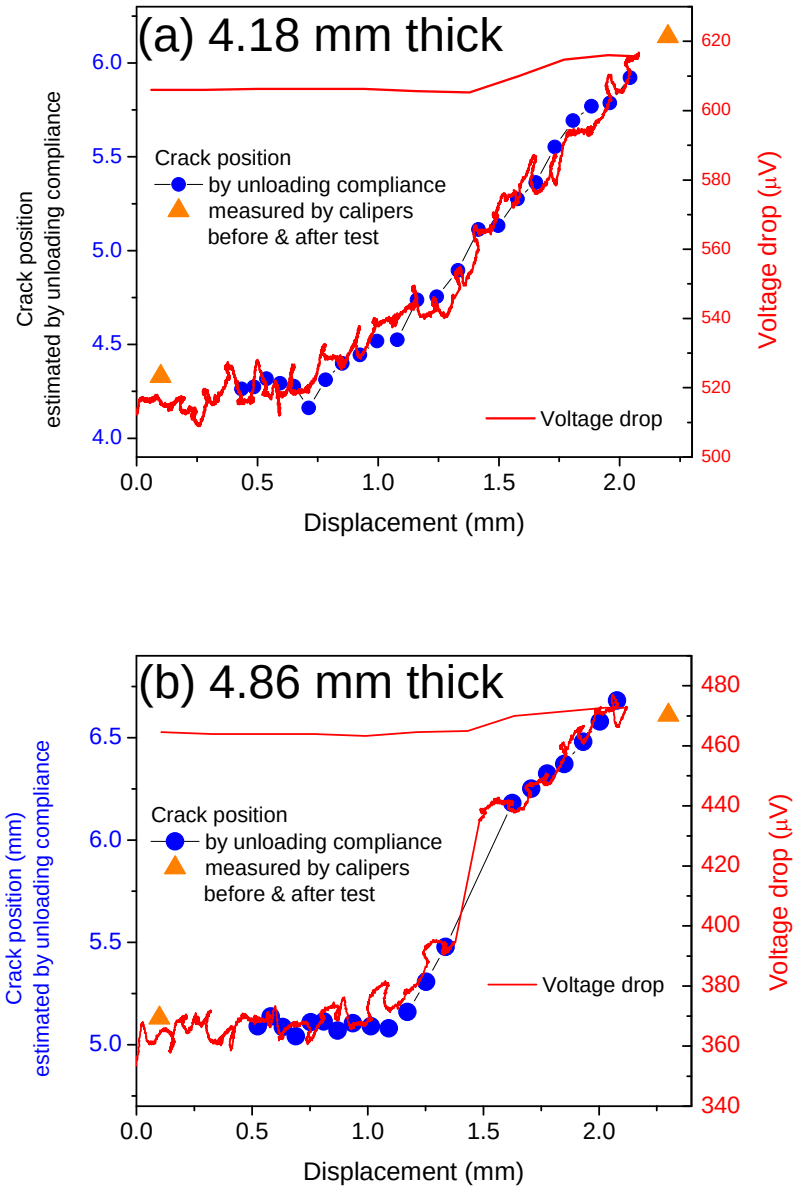

Figure 5-17. Crack position estimation for (a) 4.18 and (b) 4.86 mm thick specimens by unloading compliance which agrees with crack position before and after the test, as measured by calipers and potential drop line in overall shape.

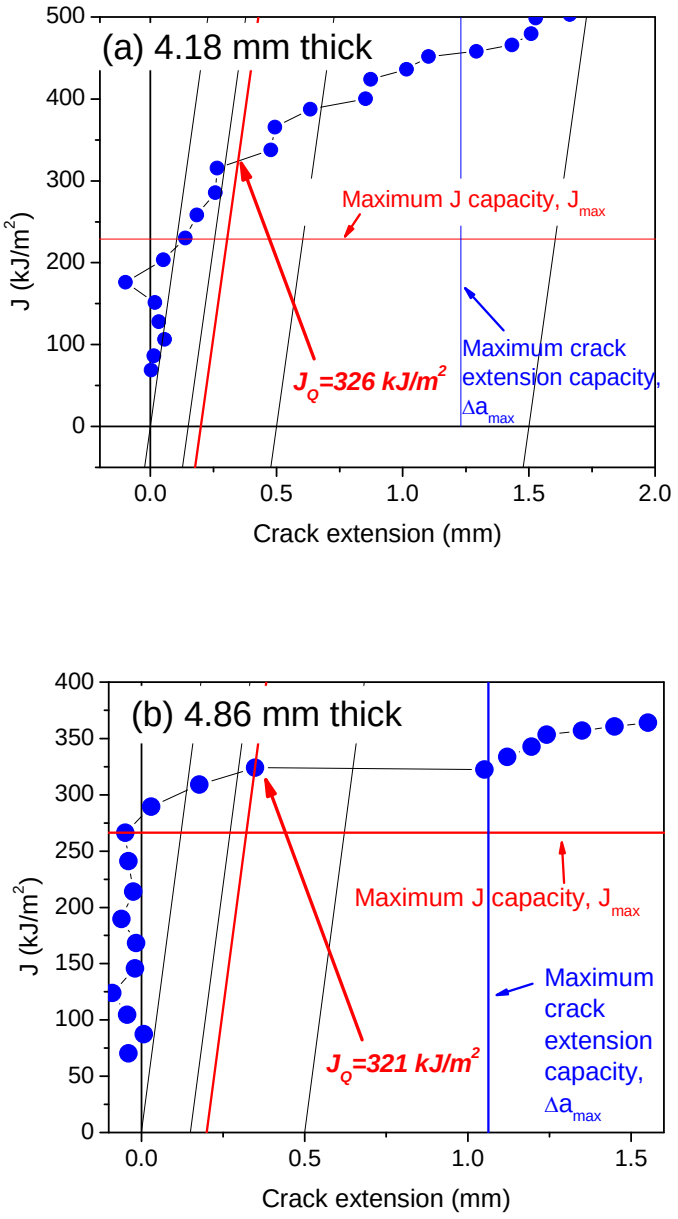

Figure 5-18. J-R curve for (a) 4.18 and (b) 4.86 mm thick specimens.

5.7.3 Effect of semi-solid processing

Load-displacement curves of DH3 ($Zr_{39.6}Ti_{33.9}Nb_{7.6}Cu_{6.4}Be_{12.5}$) specimens with different thickness are compared in Figure 5-19. As pointed out earlier, the 5.21 mm thick specimen is machined directly from an arc-melted ingot. The others are prepared by arc-melting and semi-solid processing in a copper boat. It is important to notice that the 5.21 mm thick specimen does not show a 'flat' area around the maximum load point. Unlike the others, the load-displacement curve of the 5.21 mm thick specimen starts decreasing right after it reaches maximum point. It appears that the 'flat' region of load-displacement curve is due to the heavy plastic deformation around crack tip area rather than crack growth. Crack growth induces a steeper decrease of the load-displacement curve.

The earlier composites without semi-solid processing [1,2] had cooling rate dependent microstructure and likely had large variations in the overall dendrite length scale and interdendrite spacings. The aim of semi-solid processing is to fully develop the microstructure and homogenize it. Compared to other compositions, like DH1 and 2, DH3 ($Zr_{39.6}Ti_{33.9}Nb_{7.6}Cu_{6.4}Be_{12.5}$) has higher volume fraction of ductile dendrite phase. With fully developed dendrite structure, DH3 has the minimum interdendrite distance among the three different compositions. This interdendrite distance of DH3 appears to match the characteristic length scale so that shear band extension is limited and transition into a crack is prohibited while the metallic glass part, comprising a significant fraction of the whole material, keeps the strength unusually high. Without semi-solid processing, there is no guarantee of uniform microstructure. Even with the composition of DH3, an undeveloped microstructure can cause transition of shear bands into cracks at the early stages of deformation as shown in Figure 5-9(b).

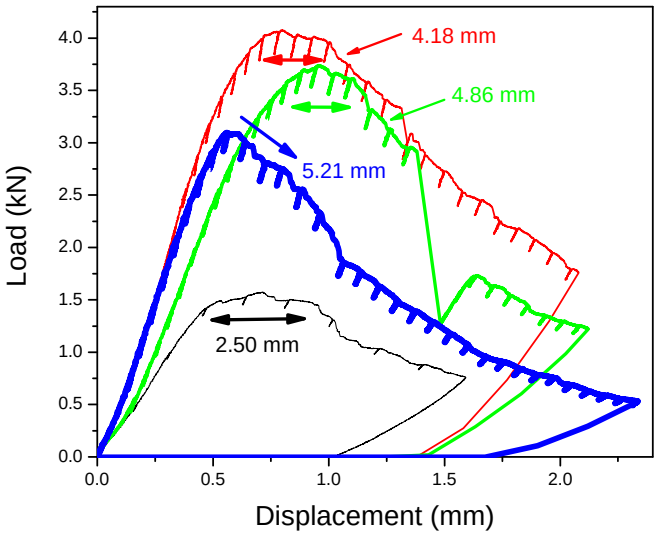

Figure 5-19. Load-displacement curves of four specimens with different thicknesses.

5.7.4 Effect of specimen thickness

Figure 5-20 shows four data points of fracture toughness expressed in terms of stress intensity factor. The curved line defines the dimensional restriction for valid fracture toughness given for a specific stress intensity factor (K) calculated from B, $b_0 > 25\ J_Q/\sigma_Y$ and a relation between energy term and stress intensity factor, $G= K^2/E \times(1-\nu^2)$. The relation means that, for a given converted stress intensity factor to be regarded as an outcome of a valid J_{IC} measurement, both thickness and ligament size ($b_0 = W – a_0$) of a fracture specimen have to be larger than a number defined by this curve. In other words, the data points should be located to right of the curve in Figure 5-20. According to the curve, the 4.86 mm thick specimen is valid for a measurement of fracture toughness up to 136 MPa·$m^{1/2}$. On the other hand, in order to measure a valid fracture toughness of 170 MPa·$m^{1/2}$, a sample thickness of at least 7.5 mm is needed. However, based on the information currently available, the critical value (J_Q) does not seem to be

affected by the specimen thickness. Although J_Q could possibly decrease rapidly at higher thicknesses, the trend seems to be along the extrapolation line given in Figure 5-20. This will be reinvestigated when new equipment with larger material production capacity becomes available.

It should be noted that even when the material is not semi-solidly processed, K_{JIC} is still as high as 104 MPa·$m^{1/2}$. Since it is known that tensile ductility goes from ~3% to ~13% with semi-solid processing [5], it makes sense that K_{IC} increases as well.

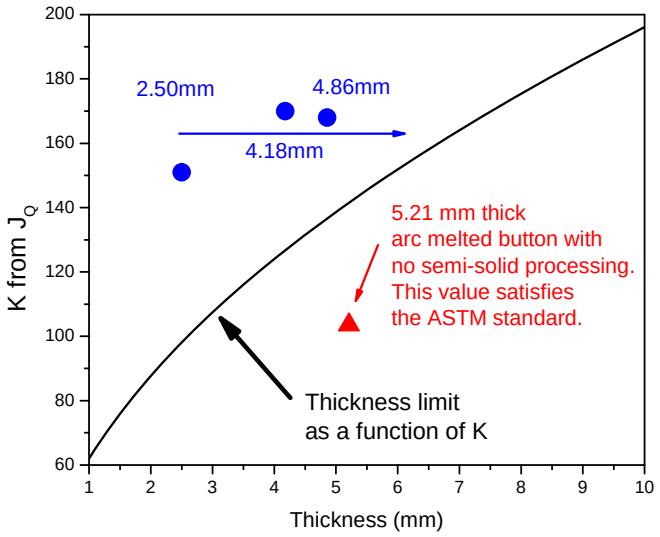

Figure 5-20. Fracture data of four specimens with different thickness expressed in stress intensity factor (K) and a curve showing limitations of specimen dimension for valid J_{IC} evaluation.

5.8 Conclusion

Unlike monolithic BMG's, BMG composites show stable crack growth and crack arrest. Enhanced fracture properties of the composite can be attributed to earlier deformation of the

ductile phase, subsequent activation of shear bands in the BMG matrix and confinement of those shear bands to keep them from developing into cracks. Increasing the volume fraction of ductile dendrite phase with fully developed microstructure increases amount of energy needed to advance existing cracks. This tendency is consistent with the designing concept of “matching the characteristic length scale”.

J-R curve evaluation of the composites reveals significant improvement in fracture toughness, having values perhaps larger than 136 $MPa \cdot m^{1/2}$. Current efforts to improve specimen production will provide a full understanding of fracture behavior of the composites and standard J_{IC} and K_{JIC} values.

Acknowledgements

The authors would like to thank Prof. G. Ravichandran of GALCIT, Caltech for providing theh MTS test system. This work was supported in part by the MRSEC Program of the National Science Foundation under Award Number DMR-0520565. We also acknowledge the Office of Naval Research for partial support of this work.

References

[1] C.C. Hays, C.P. Kim and W.L. Johnson, Phys. Rev. Lett. 84 (2000) 2901.

[2] F. Szuecs, C.P. Kim and W.L. Johnson, Acta Mater. 49 (2001) 1507.

[3] K.M. Flores, W.L. Johnson and R.H. Dauskardt, Scripta Mater. 49 (2003) 1181.

[4] G. Duan, A. Wiest, M.L. Lind, J. Li, W.-K. Rhim and W.L. Johnson, Adv. Mater. 19 (2007) 4272.

[5] D.C. Hofmann, J.-Y. Suh, A. Wiest, G. Duan, M.L. Lind, M.D. Demetriou and W.L. Johnson, Nature 451 (2008) 1085.

[6] D.C. Hofmann, J.-Y. Suh, A. Wiest and W. Johnson, Scripta Mater. 59 (2008) 684.

[7] R.D. Conner, W.L. Johnson, Scripta Mater. 55 (2006) 645.

[8] C.P. Kim, J.-Y. Suh, A. Wiest, M.L. Lind, R.D. Conner and W.L. Johnson, Scripta Mater. 60 (2008) 80.

[9] R.D. Conner, W.L. Johnson, N.E. Paton and W.D. Nix, J. Appl. Phys. 94(2) (2003) 904.

[10] R.D. Conner, Y. Li, W.D. Nix and W.L. Johnson, Acta Mater. 52 (2004) 2429.

[11] T.L. Anderson, Fracture Mechanics: Fundamentals and Applications, 1st ed. (CRC Press, 1991) p.425.

Appendix 5-A Machine compliance correction for MTS test machine

It is important to have this additional information about machine compliance correction because all of the experiments described in this chapter are performed without any crack opening gauge or strain gauge, such as a Linear Variable Differential Transformer (LVDT).

In order to evaluate machine compliance, the testing machine ram movement is recorded without any load (without the specimen installed) while attached LVDT is recording ram displacement at the same time. Based on an assumption that the testing machine ram movement without load is correct to within 1% error, the LVDT output and ram displacement are correlated as shown in Figure 5A-1. The LVDT has linear relationship with actual ram displacement: LVDT (V) = -0.01064 + 2.30393 × ram displacement (mm).

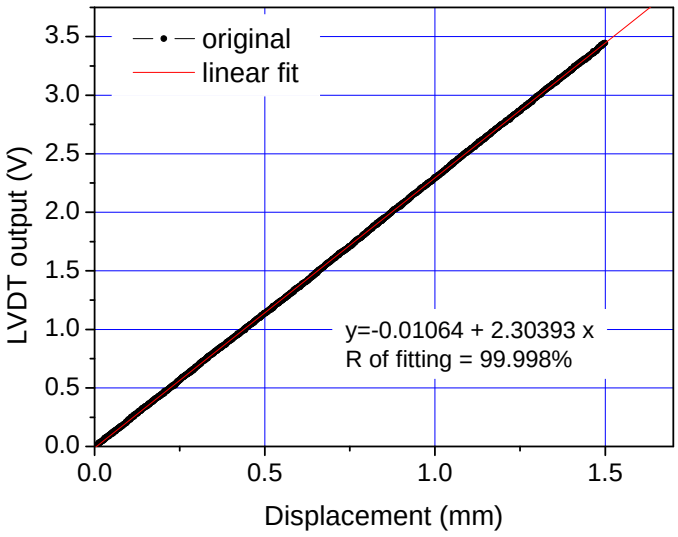

Figure 5A-1. Correlation between ram displacement and LVDT output voltage.

Then, loading is performed with the same set-up as the actual fracture test. As shown in Figure 5A-2, machine and fixture compliance exists. The difference between the ram movement reading and the LVDT reading is shown in Figure 5A-3: d_{mts}-d_{LVDT} = 0.0644 × load (kN). Applying the correction function to the actual load-displacement curve produces change shown in Figure 5A-4.

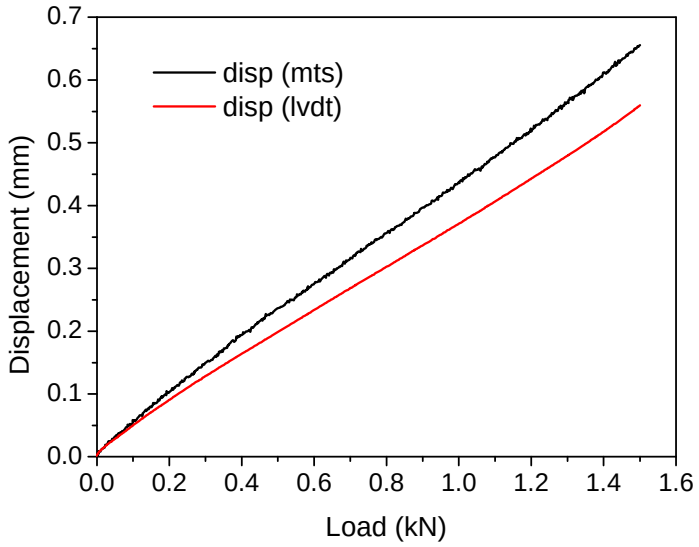

Figure 5A-2. Difference between ram displacement reading and LVDT displacement reading as a function of load applied.

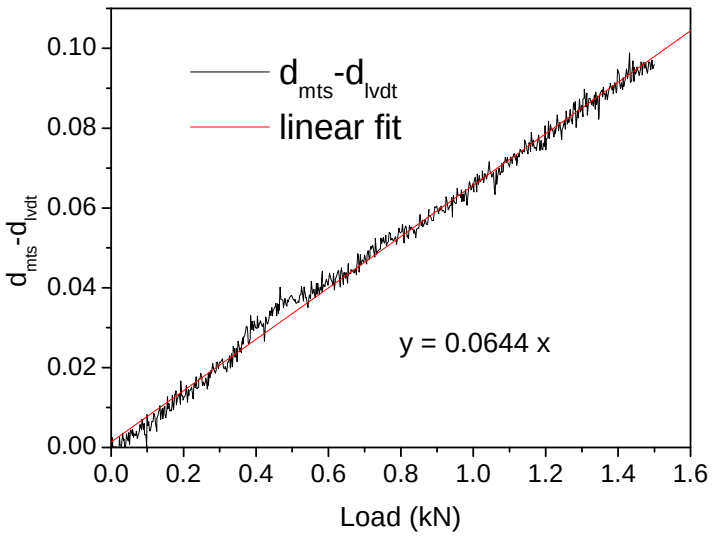

Figure 5A-3. A linear function to correct the machine and fixture compliance.

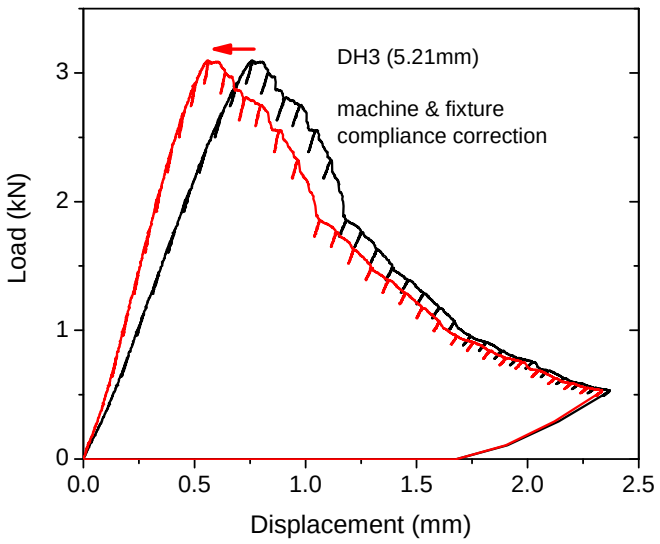

Figure 5A-4. Effect of machine and fixture compliance correction on load-displacement curve.

Chapter 6

Novel thermoplastic bonding using bulk metallic glass solder

A novel thermoplastic bonding concept is demonstrated based on the unique rheological behavior and pattern-replication ability of bulk metallic glass forming liquids. In this approach, the bulk metallic glass is heated above T_g to the “supercooled liquid” region while a small normal force is applied to the joint. This results in liquid reflow, wetting and a strong bond. Complete wetting between copper substrates and a layer of platinum based bulk metallic glass leads to an atomistically intimate void-free interface.

6.1 Introduction

One of the characteristics of Bulk Metallic Glass (BMG) is the existence of a supercooled liquid region between glass transition (T_g) and crystallization (T_x) temperatures on heating. In the supercooled liquid state, the atomic configuration of the BMG easily rearranges to accommodate plastic flow. Supercooled liquids, depending on their fragility, can have sufficient fluidity to flow under small applied pressure. The viscosity of supercooled liquids of BMGs is known to be as low as 6×10^4 Pa·s, similar to that of viscous polymer melts [1]. The fluidity of a supercooled BMG forming liquid also makes micron-sized pattern replication possible [2]. Thus it is reasonable to expect that the supercooled BMG forming liquid can wet and bond to another metal surface during this configurational rearrangement process. In this chapter, a series of bonding experiments were performed to demonstrate this new concept of thermoplastic bonding using BMG alloys. Interfacial integrity and fracture behavior are also studied.

6.2 Motivations and possible application to microelectronics industry

Solders have been extensively used in microelectronics industry because of their desirable properties such as low melting temperature (T_m) and high ductility which permits flow and reduces stress on adjacent components. Solders also exhibit good wetting on high-conductivity metal contacts like copper. Despite these attractive properties, conventional soldering has fundamental limitations. First, soldering is mainly based on reactive wetting and the reaction by-product is often a brittle intermetallic compound (IMC). The deleterious effect of IMC formation on long-term reliability of solder joints has been well documented [3-6]. Second, soldering temperature is fundamentally coupled with T_m of the solder. As a result, low-T_m solders must typically be used for low-temperature assembly where heat-sensitive devices (such as

ferroelectric polymers or liquid crystals) are to be assembled. However, such low-T_m solders are inevitably subject to high homologous temperatures (T_{hom}) in final service. Therefore they suffer extensive creep, strength loss and poor thermal stability over time. In turn, this limits their long-term reliability [7].

In this study, a novel joining/bonding concept, "thermoplastic soldering" is reported based on the unique rheological behavior [1,8] and pattern-replication ability of Bulk Metallic Glasses (BMG) [2]. BMG thermoplastic soldering provides a novel way to achieve metallurgical joining/bonding according to the following considerations:

1. On heating, BMG becomes a supercooled liquid between glass transition (T_g) and crystallization (T_x) temperatures. In the thermoplastic soldering approach, wetting takes place in the supercooled liquid state as opposed to molten state above T_m in the case of conventional soldering (see Figure 6-1). Supercooled liquids, depending on their fragility, can have sufficient fluidity to reflow under minor pressure. The fluidity of supercooled liquids of bulk metallic glasses is comparable to thermoplastics during plastic injection molding [1]. Therefore bulk metallic glass solders can be viewed as thermoplastic solders.

2. In thermoplastic soldering, the soldering temperature (~T_g) is "decoupled" from T_m. Therefore low temperature thermoplastic soldering can be achieved at relatively low process temperature compared to T_m. This potentially leads to superior reliability. After bonding, a wide variety of nano-/micro-structures from fully amorphous to partially-crystallized, to fully-crystallized structures can be obtained as a final state by controlling crystallization via post-bonding annealing to tailor the optimum electrical conductivity, creep resistance and fatigue properties for a given application. Considering the ultimate tensile strength of current Sn-based solders is around 50 MPa [9, 10], even embrittled or crystallized BMG solder could be considered for such applications. This leads to a lower homologous temperature (T_{hom}) in final service.

Therefore, joints fabricated using this method would be more resistant to creep, electromigration, strength loss and poor thermal stability over time.

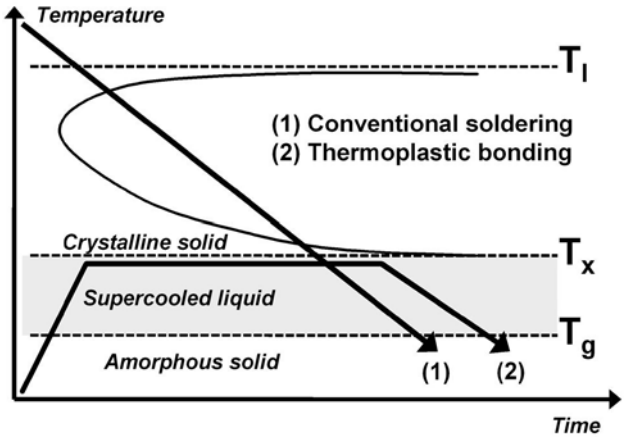

Figure 6-1. Schematic diagram showing the concept of "*Thermoplastic bonding.*"

6.3 Proof of concept experiment (Effect of processing condition)

6.3.1 Experimental

In order to demonstrate this novel bonding concept, a platinum based BMG [11] was selected because of its oxygen inertness and low T_g. A fully amorphous strip of $Pt_{57.5}Cu_{14.7}Ni_{5.3}P_{22.5}$ [11] with thickness of about 0.46 mm was prepared with T_m, T_g and T_x of 499, 226.1 and 299.2°C, respectively (measured by a Netzsch 404C DSC at a scan rate of 20°C-min^{-1}.). Copper cylinders of 6.35mm diameter, 6.35mm length and purity of 99.996% (produced by Alfa Aesar) were used as substrates. Machining reduced the diameter at the bonding surface to 3mm by having the surface outside this 'contact zone' slightly slanted to about 2-3 degrees from horizontal line, as shown in the inset in Figure 6-2. The cylinders were dipped into nitric acid to

remove any surface oxide on the copper. The glassy solder strip was stacked between two copper cylinders without flux, and the assembly was placed in a loading fixture inside a vacuum chamber equipped with a Radio Frequency (RF) heating coil. Temperature was monitored via a K-type thermocouple spotwelded to one of the copper cylinders. The bonding process was performed in a high vacuum of order 10^{-6} mbar to minimize any oxidation. The assembly stack was heated to the process temperature at a heating rate of approximately 100°C-min^{-1}, held at the process temperature under load for 2 minutes, then cooled. Figure 6-2 shows a joint formed by the BMG supercooled liquid bonding process.

After bonding, the electrical resistance of each joint was measured using the 4-point probe method with an approximately 5mm inner probe spacing. The bond strength was measured mechanically using an Instron 5500R frame with a constant crosshead speed of 0.2mm-min^{-1}. Fracture surfaces were examined using a Leo 1550 VP Field Emission SEM.

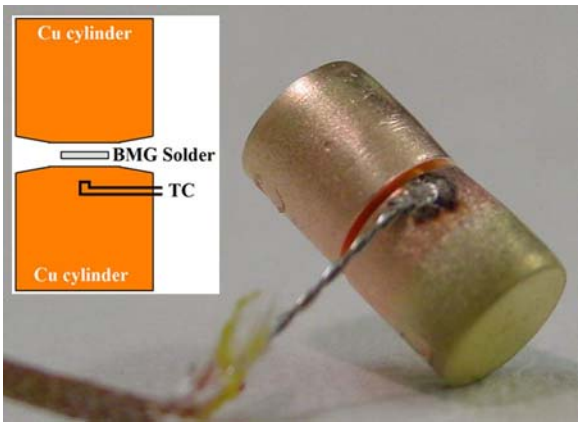

Figure 6-2. Copper-solder-copper stack with thermocouple after processing. Inset: schematic diagram showing experimental configuration.

6.3.2 Results and Discussions

Three different process loads were used for bonding: 5.4, 14.2 and 36.5N, respectively. With the 7.065mm^2 bonding area (area of the 'contact zone' with 3mm diameter), this correlates to an applied pressure of 0.76, 2.0 and 5.2 MPa. And, two different temperatures, 290 and 300°C, were used for the process. A stable, homogeneous joint was not formed at the lowest load, 5.4N. Thus, it is evident that a minimum process load is necessary for joint formation. Once the process load exceeds this critical threshold, the effect of additional load on joint integrity appears to be insignificant. Failure load of joints generated at process loads of 14.2 and 36.5N are shown in Table 6-1. The failure loads of joints formed at 290°C with 14.2 and 36.5N preload are 152 and 122N, respectively. Failure loads for joints formed at 300°C are 319 and 354N.

Table 6-1. Bonding process condition and experimental results.

Process load (N)	Process temp (°C)	Solder weight (mg)	Solder dia. after process (mm)	Solder thickness after process (μm)	Fracture load (N)	Stress with 3mm-dia. bonding area (MPa)	Stress with actual dia. of sample after process (MPa)
14.2	290	25.34	4.35	95.04	151.9	21.5	10.2
14.2	300	19.35	4.43	64.07	318.5	45.1	20.7
36.5	290	13.83	3.99	62.45	121.5	17.2	9.7
36.5	300	15.01	4.28	53.14	353.8	50.0	24.6

The final thickness of BMG solder after process is calculated using solder weight, solder diameter measured after process (given in Table 6-1) and solder density (15.3 g/cc) [12] taking the slope of the surface outside the 'contact zone' into account. Initially 460μm thick solders

were squeezed down to between 50 and 100μm indicating significant flow in each solder during process.

The fracture surfaces examined using SEM back-scattered images of separated joints processed with 36.5N load are shown in Figure 6-3. The samples in Figure 6-3(a-1) and (a-2) were formed at 290°C and Figure 6-3(b-1) and (b-2) at 300°C. Circles in each micrograph indicate the 3mm diameter ‘contact zone’. From compositional contrast, the copper surface appears dark and the platinum based BMG surface bright. Comparing the surfaces in figures (a) and (b), we see that the failure mode transitions from Cu/BMG interfacial fracture to fracture within the BMG solder as the process temperature increases. For the joint produced at 290°C, only a small fraction of the ‘contact zone’ has BMG solder residue on the copper surface (Fig. 6-3(a-1)). On the other hand, for the joint processed at 300°C, most of the ‘contact zone’ is covered by BMG solder residue (Fig. 6-3(b-1)).

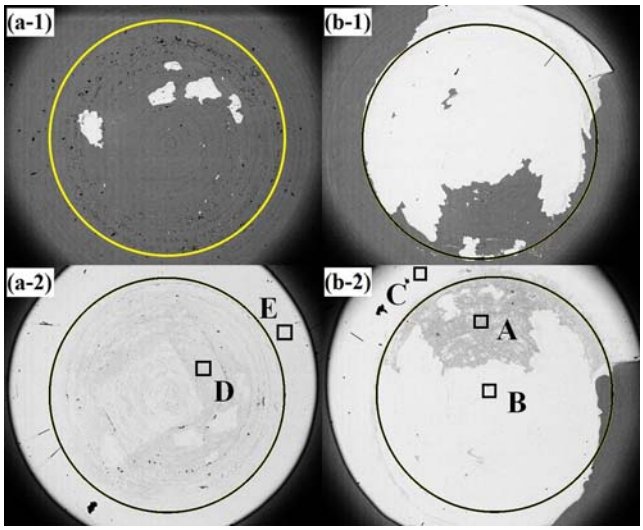

Figure 6-3. Back scattered images of both fracture surfaces of joints produced with 36.5N at (a) 290°C and (b) 300°C. By the compositional contrast, copper surface looks dark and platinum based BMG surface looks bright. The circle marks show ‘contact zone’ with 3-mm diameter. Squared areas marked as from A to E indicate where EDS scans were performed. (listed in Table 6-2.)

Table 6-2. Compositional information by Energy Dispersive Spectroscopy (in at.%).

Area	Pt	Cu	Ni	P
A	20.8	72.8	1.5	4.9
B	60.3	19.9	5.5	14.3
C	57.5	19.7	5.9	16.9
D	37.7	51.1	3	8.2
E	58.1	18.8	4.9	18.2

Energy Dispersive Spectroscopy (EDS) data acquired from squared areas defined in Figure 6-3 are summarized in Table 6-2. For the sample processed at 300°C, as expected from the contrast given by back-scattered electron image, the shaded area (around square A in Figure 6-3(b-2)) has a significantly high concentration of copper. This area was in contact with copper substrate before fracture. The large amount of copper residue on the detached BMG solder surface must be related to the strong bond formation. Bright area (around square B) is a fracture surface of BMG solder. Because this part was distant from the interface with copper, EDS shows almost identical composition with known composition of the solder used. The area outside the circle (around square C) shows that concentration of copper was not increased thereby indicating that the area outside the 'contact zone' did not form a strong bond interface. The same tendency was acquired from the sample processed at 290°C (squares D and E in Figure 6-3(a-2)). This is also confirmed by the fact that the shaded area in both Figure 6-3(a-2) and (b-2) is limited inside the 'contact zone'. This is because the fluid pressure squeezed between parallel plates is decreasing as a function of r, distance from center [13]. And, the slope outside the 'contact zone' should cause an additional pressure drop which could result in poor bonding quality in this area. Thus, it might be reasonable to evaluate the fracture stress of the joints based on the area of the 'contact zone'. As shown by Table 6-1, failure stress of joints formed at 290°C with 14.2 and 36.5N preload, calculated based on 7.065mm^2 contact area, are 21.5 and 17.2MPa, respectively. Failure stress for joints formed at 300°C are 45.1 and 50.0MPa. Also, stress calculated by the whole surface area of each solder, which is the lowest limit value for bonding stress, is given in Table 6-1.

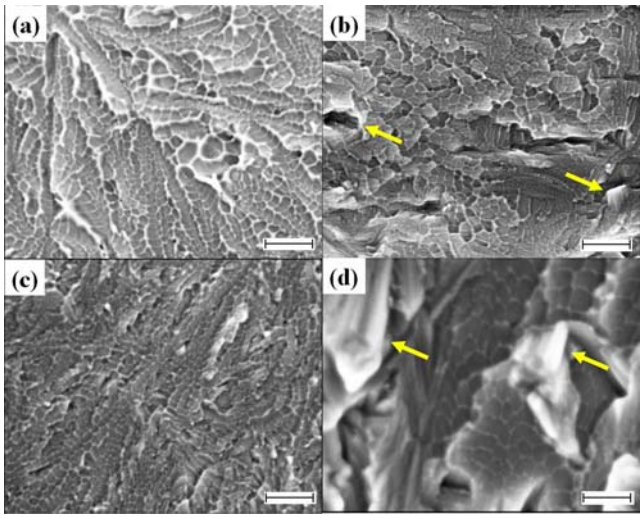

Figure 6-4. High resolution fractography on BMG solder residues produced by (a) 36.5N at 290°C, (b) 36.5N at 300°C, (c) 14.2N at 290°C and (d) 14.2N at 300°C. Scale bars in (a-c) for 200 nm (100,000× magnification) and (d) for 100 nm (200,000× magnification).

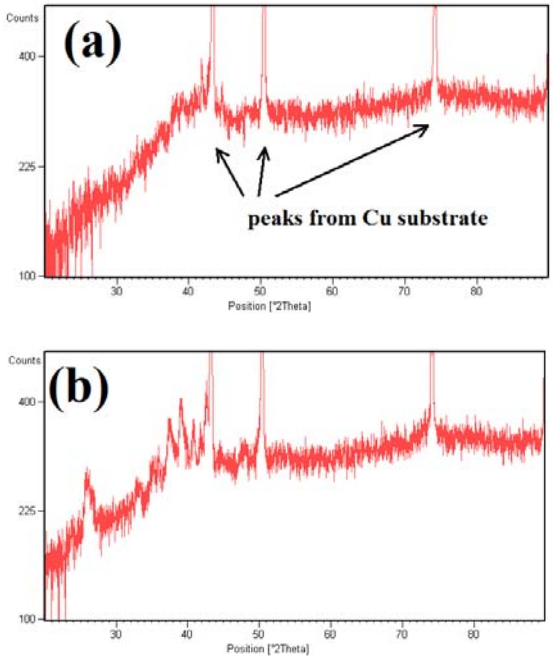

Figure 6-5. X-ray diffraction patterns of fracture surface of joints produced with 36.5N at (a) 290°C (surface shown in Figure 6-3(a-2)) and (b) 300°C (surface shown in Figure 6-3(b-2)).

High resolution fractography of the BMG solder residues reveals a dimple pattern (Figure 6-4). This dimple pattern is typical for fracture surfaces of BMGs [14, 15] and confirms that fracture is through the BMG and not along the interface. For both joints, the areas with BMG solder residue are thought to have formed an intimate interface between the copper and BMG solder. It is also notable that the size of dimple is less than 100 nm for both samples processed at 290 and 300°C. According to an empirical relationship regarding the dimple size [15], small dimple size correlates with poor fracture toughness. In addition, small crystallites growing with a columnar shape are shown in the sample processed at 300°C (indicated by arrows in Figure 6-4(b) and (d)). This crystallization also can be confirmed by X-ray diffraction pattern shown in Figure 6-5. Figure 6-5(a) is taken from a surface shown in Figure 6-3(a-2) which is formed at 290°C and Figure 6-5(b) from Figure 6-3(b-2) at 300°C. Except for the peaks from Cu substrates, the pattern taken from the solder surface processed at 290°C (Figure 6-5(a)) appears glassy. On the other hand, the surface processed at 300°C, shown in Figure 6-5(b), shows many crystalline peaks. Generally crystallization of a BMG is known to accompany embrittlement. Due to the process temperatures being as high as the crystallization temperature, crystallization to a certain extent during processing appears to be inevitable for the current Pt-based BMG and copper system. Thus, additional study is required to understand the details of the bonding mechanism. A better understanding of the bonding mechanism could lead to enhanced wettability of BMG solders at lower temperature, improved interfacial integrity and increased control over the final structure of the BMG solder.

As shown in Table 6-1, the final thickness of the BMG solders ranges from 50 to 100 μm. The measured electrical resistance of the joints is reasonably small, ranging from 21 to 27μΩ for the joints formed at 290°C and from 13 to 15μΩ for those at 300°C. For the joints formed at 300°C, an ideal resistance is estimated for a 50μm thick BMG solder with an area of 7.065mm^2 to

be 13.1μΩ based on the resistivity of the platinum based glass (1850nΩ·m). The measured resistance values are close enough to claim formation of an intimate interface.

6.4 Cross-sectional Transmission Electron Microscopy (TEM) study

For cross-sectional TEM work, joints were sectioned via ultramicrotomy and examined using an FEI Tecnai F30UT high resolution TEM operated at 300kV.

Figure 6-6 shows TEM images of the specimen shown in Figure 6-3(b), which is processed at 300°C with 36.5 N. The BMG solder is partially crystallized as seen in Figure 6-4 and 6-5. The spot pattern shows amorphous ring and many tiny dots on the amorphous hollow, which suggests the existence of small crystalline particles (Figure 6-6(a)). A pair of bright field and dark field images (Figure 6-6(b) and (c)) shows nano-meter sized crystalline particles inside the BMG solder. Although most of the BMG solder is partially crystallized, an intimate interface between copper substrate and BMG solder can be found as shown in Figure 6-7.

An interface processed at temperature lower than 300°C is also observed. Cross-sectional TEM observations of the interface shown in Figure 6-8(a) and (b) shows that the BMG solder completely replicates microscopic details of the copper surface and forms a void-free interface. High resolution imaging of the interface (Figure 6-8(c)) provides evidence that the BMG solder forms an intimate atomistic scale bond with the copper. No interfacial reaction product is observed along the interface between BMG and copper within the resolution of the TEM.

Stepwise EDS spectrum scan performed from the interface to about 1.5 μm deep into the Pt-BMG with a 0.1 μm step size does not find any evidence of preferred diffusion of specific constituting element.

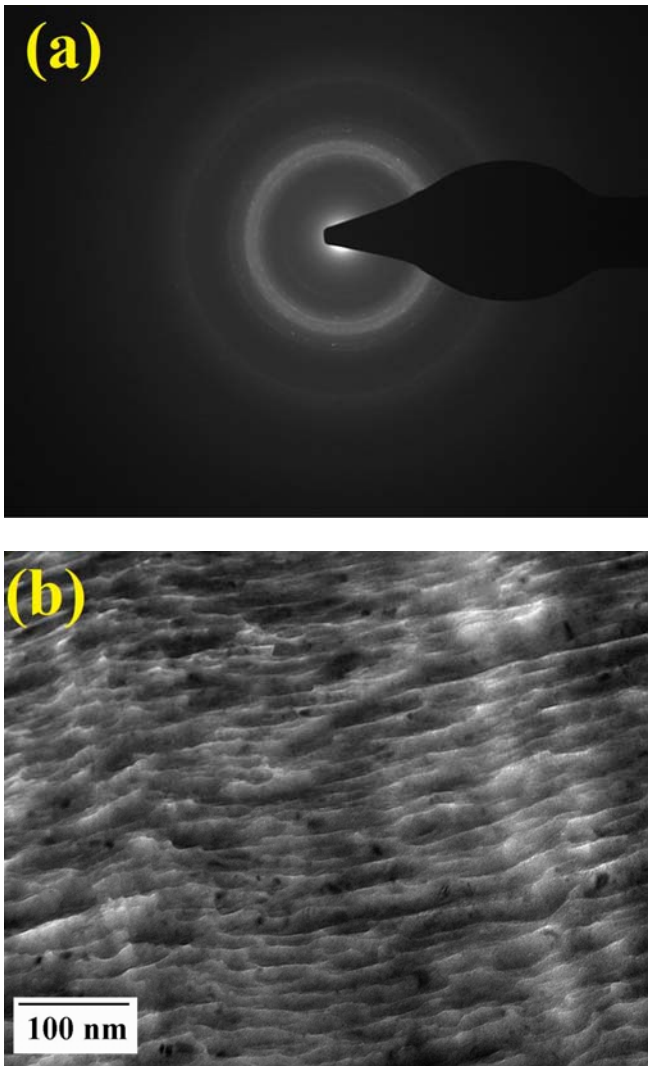

(Figure 6.6. continued)

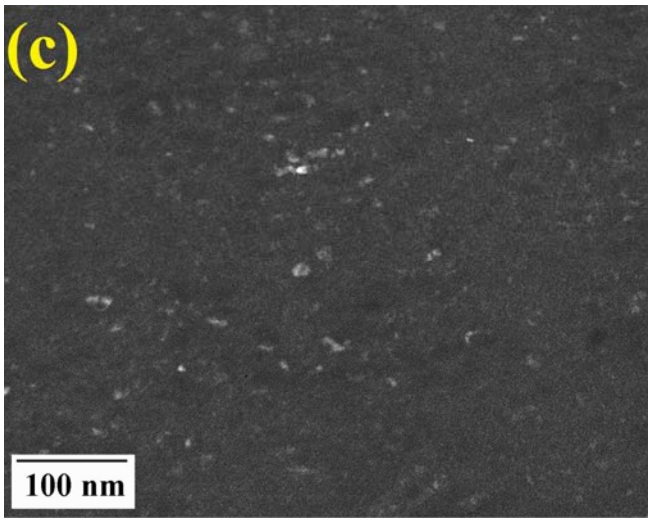

Figure 6-6. TEM images of BMG solder part processed at 300°C, with load of 36.5 N, specimen shown in Figure 6-3(b). (a) spot pattern, (b) bright field image and (c) dark field image of the same place shown in (b). (Magnification: 220,900×)

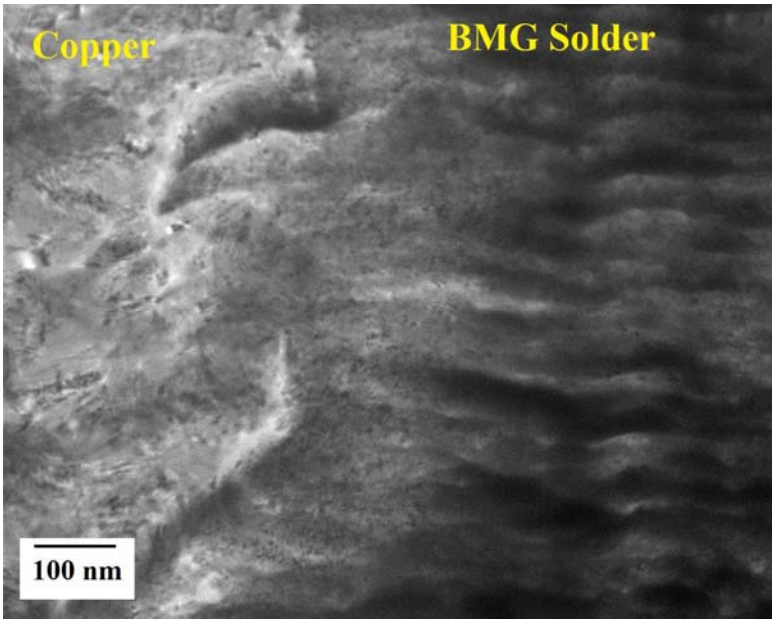

Figure 6-7. Interface between copper substrate and BMG solder in specimen processed at 300°C with 36.5 N load.

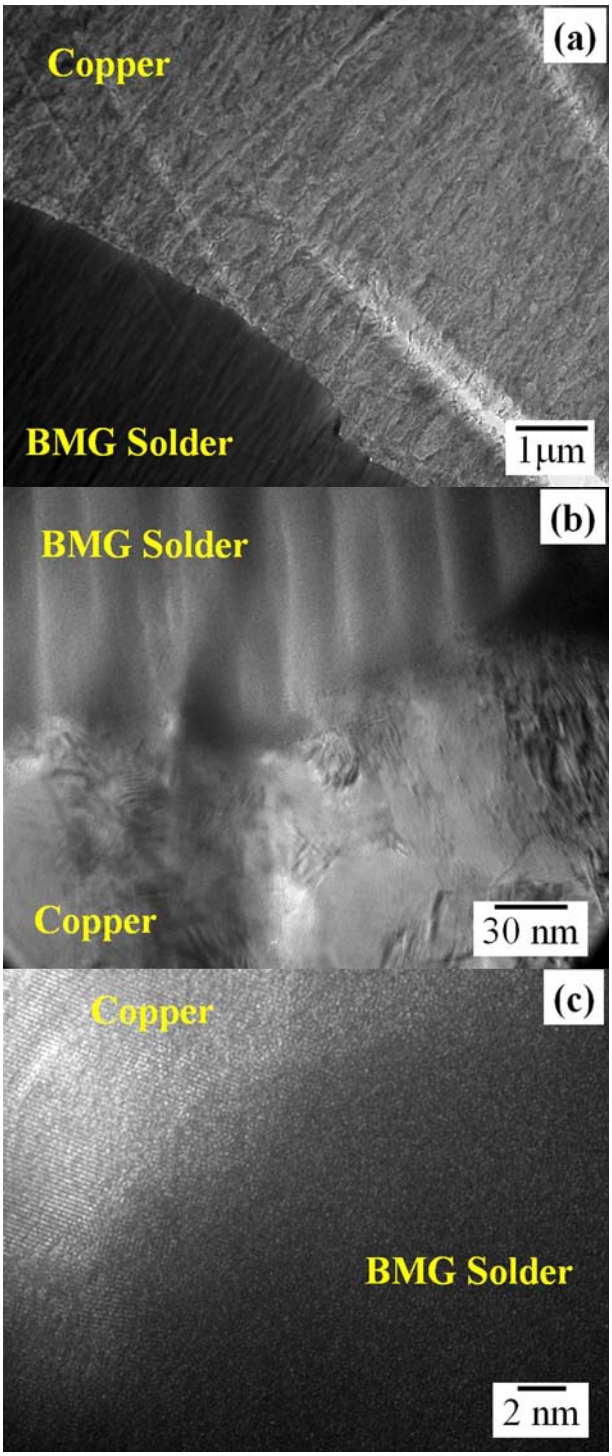

Figure 6-8. The solder-copper interface shown at (a) low magnification (15,400×), (b) high magnification (523,000×) and (c) high resolution (5,335,000×)

6.5 Effect of pressure distribution

Although the viscosity of supercooled liquid can be as low as 6×10^4 Pa·s, similar to that of viscous polymer melts [1], the viscosity of supercooled liquid is still much higher than that of molten tin around the melting point, which is about 2×10^{-3} Pa·s [16]. As a result, pressure needs to be applied during the joining process to assist the supercooled liquid to spread out and wet on other metal surfaces. Pressure dependence on joint quality could exist. However, the fluid pressure squeezed between parallel plates is decreasing as a function of r, distance from center, as described in Equation 6-1 [13].

$$p = -\frac{3\eta}{h^3}\frac{dh}{dt}\left(R^2 - r^2\right) + \Pi \qquad \text{Equation 6-1.}$$

η denotes liquid viscosity, h liquid thickness, t time, R outermost distance of liquid from center and Π constant pressure.

This pressure distribution seems to affect the bonding quality. Figure 6-9 shows cross-sectional image of the rim part of the specimen shown in Figure 6-3(b-2), which is processed at 300°C with 36.5 N of load. Inset of Figure 6-9 is the overall specimen cross-sectional image. Figure 6-9 is taken from the square inside the inset. From the overall cross-sectional image, the machined area which is slanted about 2-3 degree angle to the horizontal and central ‘contact zone’ is clearly seen. At the point where this inclination begins, the boundary between bonding and no-bonding surface exists as can be seen from the magnified image. Thus, the previous observation that the slope outside the ‘contact zone’ causes an additional pressure drop and results in poor bonding quality in this area is confirmed again.

Systematic study carried out in section 6.3 of this chapter shows the existence of required minimum process load for a joint formation. However, the effect of additional load on joint integrity appears to be insignificant once the process load exceeds this critical threshold. The

insensitivity to pressure after exceeding the critical threshold could be due to the open nature of the squeezing geometry. In other words, pressure dependence could exist and be detectable if the flow of the supercooled liquid could be confined. Further refined experiments are required to confirm the effect of pressure.

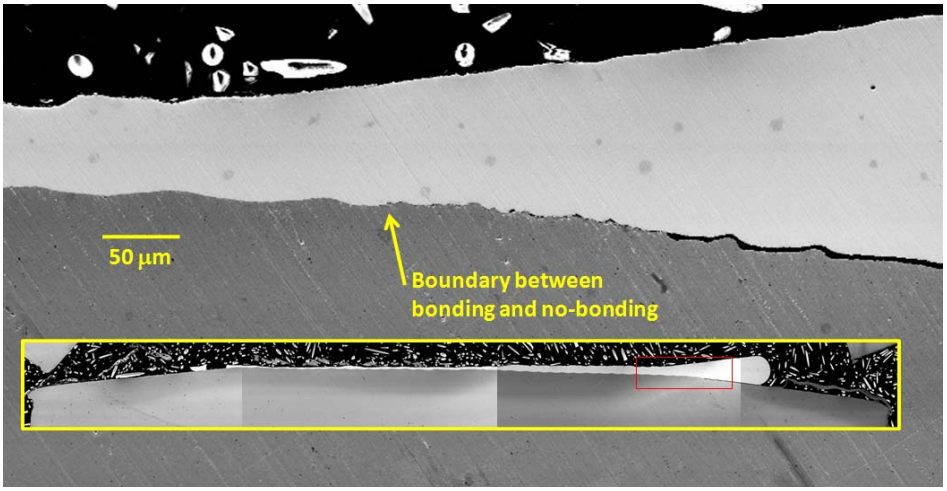

Figure 6-9. Rim part of the specimen shown in Figure 6-3(b-2). Inset: Overall specimen cross-section having small square mark on the right side. This small square is where this figure is taken from.

6.6 Interfacial reaction and fracture behavior

The interface formed by 300°C with a load of 36.5N is magnified in Figure 6-10. The left column of the figures is from the upper part, the boundary between Pt-BMG solder and the molding compound as shown in Figure 6-9, and the right column is from the lower part, the boundary between Pt-BMG solder and the copper substrate. The upper row of the figures is taken by secondary electron detector and the lower row by back-scattered electron (BSE) detector.

Compositional contrast by BSE detector reveals a different phase formed between Pt-BMG and copper substrate, indicated by arrows in Figure 6-10(a-2) and (b-2). This ‘reaction layer’ is also found in the interface formed at 290°C, but is not as pronounced as that of 300°C, as shown in Figure 6-11. This reaction layer makes a clear distinction between the interfaces formed at 290 and 300°C. Temperature appears to be an important factor for formation of the reaction layer. The existence of reaction layer has not been confirmed by TEM yet. But, it should be recalled that this reaction layer is not a necessary condition for intimate bonding interface formation as proven by TEM work shown by Figure 6-8 for a specimen processed under 300°C.

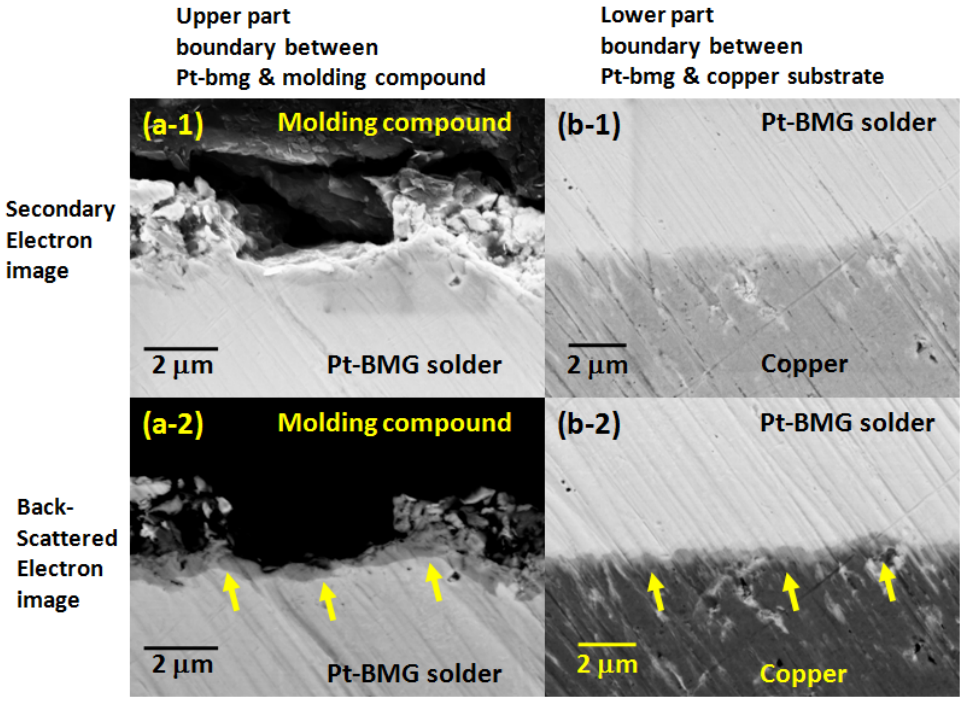

Figure 6-10. Magnified images of interface shown in Figure 6-9 and Figure 6-3(b-2), produced at 300°C with a load of 36.5N. (a) Upper part of the specimen. Boundary between the Pt-BMG solder and molding compound. (b) Lower part of the specimen. Boundary between the Pt-BMG solder and copper substrate. (a-1) and (b-1) are secondary electron images. (a-2) and (b-2) are back-scattered electron images.

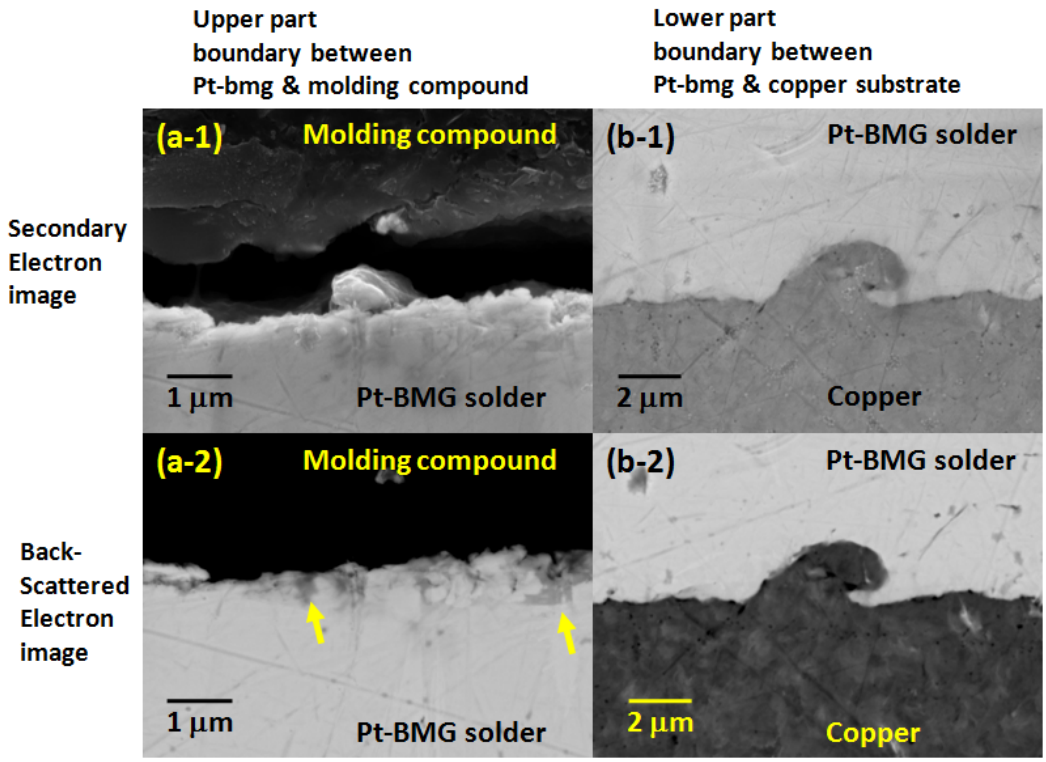

Figure 6-11. Magnified images of interface of the specimen shown in Figure 6-3(a-2), produced at 290°C with a load of 36.5N. (a) Upper part of the specimen. Boundary between the Pt-BMG solder and molding compound. (b) Lower part of the specimen. Boundary between the Pt-BMG solder and copper substrate. (a-1) and (b-1) are secondary electron images. (a-2) and (b-2) are back-scattered electron images.

The interface between the Pt-BMG and the copper substrate of a specimen after a tension test is carefully observed and cavities like the ones shown in Figure 6-12 are found. These cavities appear to be expanded by plastic deformation of the copper substrate following their nucleation. The cavity shown in Figure 6-12(b) in particular, has wedged shape on both the Pt-BMG surface and the copper substrate and the distance between them widens from the tensile load applied to this interface. Some of the cavities have compositional contrast on top, implying

that the top is richer in copper than other parts of the BMG. This suggests a high temperature diffusion process called ‘Kirkendall voiding’ as a possible candidate for void nucleating mechanism. Kirkendall voids are defined as voids induced by a diffusion couple between two different metals that have different interdiffusion coefficients. As shown in Figure 6-3 and Table 6-2, fracture at the interface between the Pt-BMG and copper leaves copper residue on the Pt-BMG surface. This copper residue could be either pure copper pieces pulled from copper substrate or copper atoms diffusing into the Pt-BMG solder. Thus, it is reasonable that such Kirkendall voids nucleate during or after bonding process. However, EDS analysis confirms that interfacial fracture leaves little Pt-BMG residue on the copper surface. Therefore, copper appears to be the only candidate for the possible diffusion process in this system.

The fracture surface of Pt-BMG with high copper concentration (like the area ‘A’ defined in Figure 6-3(b-2)) is observed at higher magnification and compared to matching surface of copper. Figure 6-13 is a direct comparison of two matching fracture surfaces with high magnification. An island full of dimples surrounded by Pt-BMG fracture surface exists. In other words, fracture occurred through Pt-BMG, not along the interface, except for the island area. In the island area, fracture occurred through the interface between Pt-BMG and copper surface. Figure 6-13(a) is a back-scattered electron image and (b) is a secondary electron image. In Figure 6-13(a), Pt-BMG surface underneath the copper residues pulled out by tension loading looks darker than the surrounding Pt-BMG, probably due to higher copper concentration. Dimple patterns in (a) and (b) match in shape, which suggests that the dimple patterns form following the bonding process. If the dimple patterns on the copper surface in Figure 6-13(b) existed before bonding, the Pt-BMG would have generated a negative replication of the dimples during bonding. Thus, it is apparent that the dimple patterns on the copper surface have formed either by Kirkendall void diffusion right after bonding or by heavy deformation during the tension test. In

this sense, Figure 6-13 can be connected to Figure 6-12 in describing possible fracture mechanism of the interface. Figure 6-14 provides the same comparison for another specimen processed at the same temperature, 300°C. Figure 6-14(a) and (b) are matching surfaces but they do not look like matching surfaces. Like Figure 6-13, Pt-BMG solder does not replicate the copper surface, which suggests that both fracture surfaces have formed after the bonding process. It is noteworthy that a magnified view of the Pt-BMG surface in Figure 6-14(c) has distributed compositional contrast. The contrast may have originated from the mixture of original Pt-BMG (white, arrow 'B'), copper diffused Pt-BMG (bright gray, arrow 'A') and copper residue (dark, arrow 'C'). Based on these observations, it is rather clear that the higher copper concentration on the surface of Pt-BMG detached from the copper substrate is a combination of pure copper pieces pulled from copper substrate and copper atoms diffusing into the Pt-BMG solder.

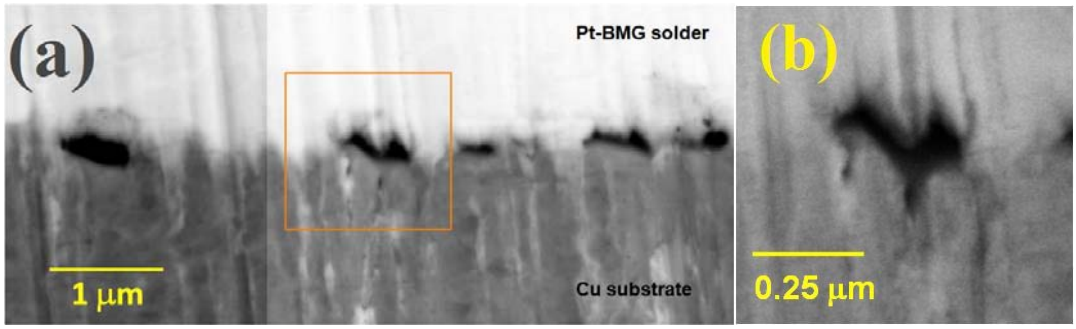

Figure 6-12. (a) Back-scattered electron image of interface between Pt-BMG solder and Cu substrate after tension test, showing cavities nucleated and expanded. (b) magnified secondary electron image of the cavity squared in (a).

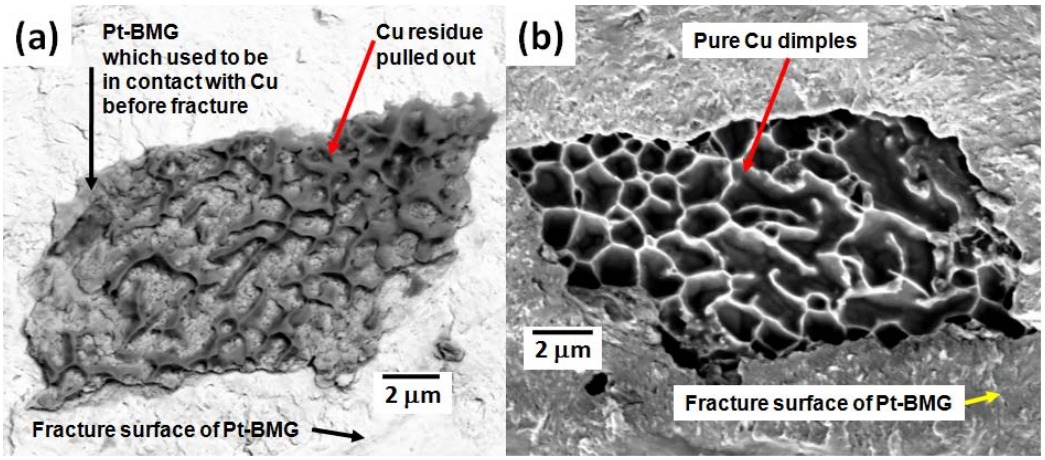

Figure 6-13. Matching fracture surfaces of a joint processed at 300°C. (a) Fracture surface of Pt-BMG side. Central area has copper residue pulled out by tension (b) Exposed pure copper surface surrounded by Pt-BMG residue still sticking to the copper surface.

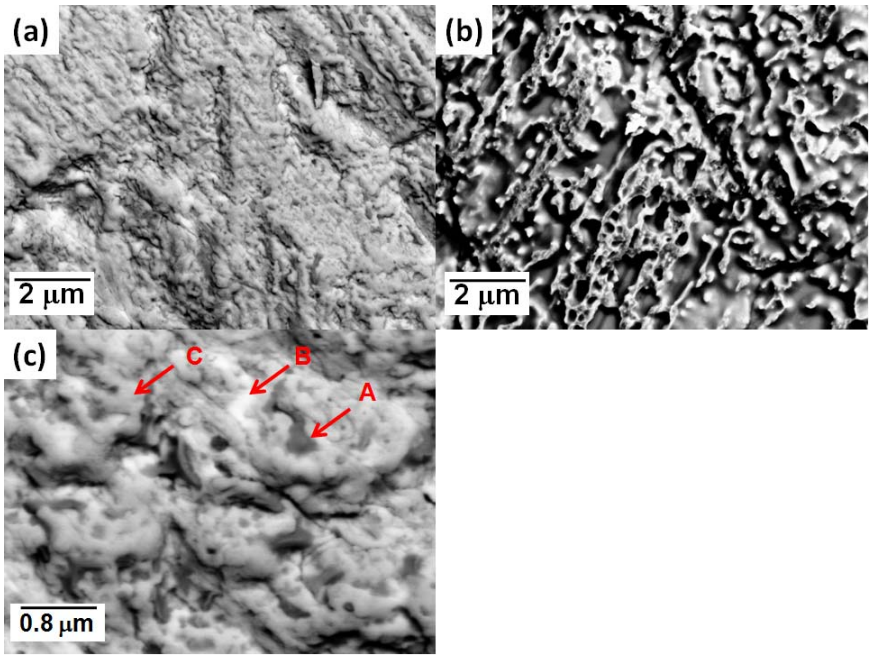

Figure 6-14. Fracture surface of a joint processed at 300°C. All images are taken by back-scattered electron detector. (a) Pt-BMG solder and (b) copper substrate. (c) higher magnification image of Pt-BMG surface showing compositional contrast.

6.7 Applicability of other BMG's

Although Pt-BMG has low glass transition temperature (T_g) comparable to the reflow temperature of conventional soldering in microelectronics industry and is proven successfully to work as a thermoplastic "solder", its optimum process temperature is much higher than T_g, close to the crystallization temperature (T_x). Thus, the next step is to search for other BMG's with lower process temperature available for the thermoplastic joining process. Possible candidate BMG's are Au-based [17], Mg-based [18] and La-based [19] alloys. In this study, $Au_{49}Ag_{5.5}Pd_{2.3}Cu_{26.9}Si_{16.3}$, a variant of $Au_{49}Ag_{5.5}Pd_{2.3}Cu_{26.9}Si_{16.3}$ with Ti addition and $La_{57.6}Al_{17.5}Cu_{12.45}Ni_{12.45}$ alloys are produced and processed for thermoplastic joining. Table 6-3 shows basic data of the alloys used in this study. The addition of Ti has little effect on ΔT or the heat of crystallization. The $Au_{49}Ag_{5.5}Pd_{2.3}Cu_{26.9}Si_{16.3}$ and $Au_{48}Ag_{5.5}Pd_{2.3}Cu_{26.9}Si_{16.3}Ti_1$ alloys do not bond with the pure copper surface. A possible reason is based on the thermal stability. Figure 6-15 shows DSC scans of the $Au_{48}Ag_{5.5}Pd_{2.3}Cu_{26.9}Si_{16.3}Ti_1$ alloy specimens processed at different temperatures for 2 minutes. Specimens processed at 160 and 170°C have almost the same DSC curves as that of an as-cast specimen, which means there is no significant crystallization. These specimens are not fully squeezed out during joining process which implies that the solder does not have enough fluidity. But, once the temperature reaches a critical temperature causing enough fluidity to result in the BMG solder forming a bond, the BMG solder crystallizes. There is no evidence of remaining glass from the specimens processed at 175 and 180°C. This abrupt crystallization behavior contrasts with Pt-BMG solder which still has significant fraction of glass even after a long exposure and deformation around its crystallization temperature. Time-temperature-transformation (TTT) diagram of both BMG's supports the huge difference in thermal stability. As shown in Figure 6-16, the crystallization kinetics of the $Au_{49}Ag_{5.5}Pd_{2.3}Cu_{26.9}Si_{16.3}$ is much faster than that of $Pt_{57.5}Cu_{14.7}Ni_{5.3}P_{22.5}$. Therefore, it is necessary

to have robust glass forming ability and thermal stability to be used as a thermoplastic solder. On the other hand, $La_{57.6}Al_{17.5}Cu_{12.45}Ni_{12.45}$ has higher T_g, T_x and ΔT than Au-based BMG's. A joint processed at 230°C for 2 minutes with 14.2 N of load has about 3 kgf (kilogram-force) of fracture load. Figure 6-17 shows the joint after a tension test. Although the strength of the joint is much smaller than the fracture loads of Pt-BMG joints, 3 kgf of bonding strength suggests a bond formation on a limited area of the contact surface. Further study is required.

Table 6-3. Thermal properties of Au-based and La-based BMG's.

composition (at %)	T_g (°C)	T_x (°C)	ΔT	d_c (mm)	ref.
$Au_{49}Ag_{5.5}Pd_{2.3}Cu_{26.9}Si_{16.3}$	128	186	58	5	[17]
$Au_{48}Ag_{5.5}Pd_{2.3}Cu_{26.9}Si_{16.3}Ti_1$	125.4	182.1	56.7	-	-
$La_{57.6}Al_{17.5}Cu_{12.45}Ni_{12.45}$	162	237	75	8	[19]

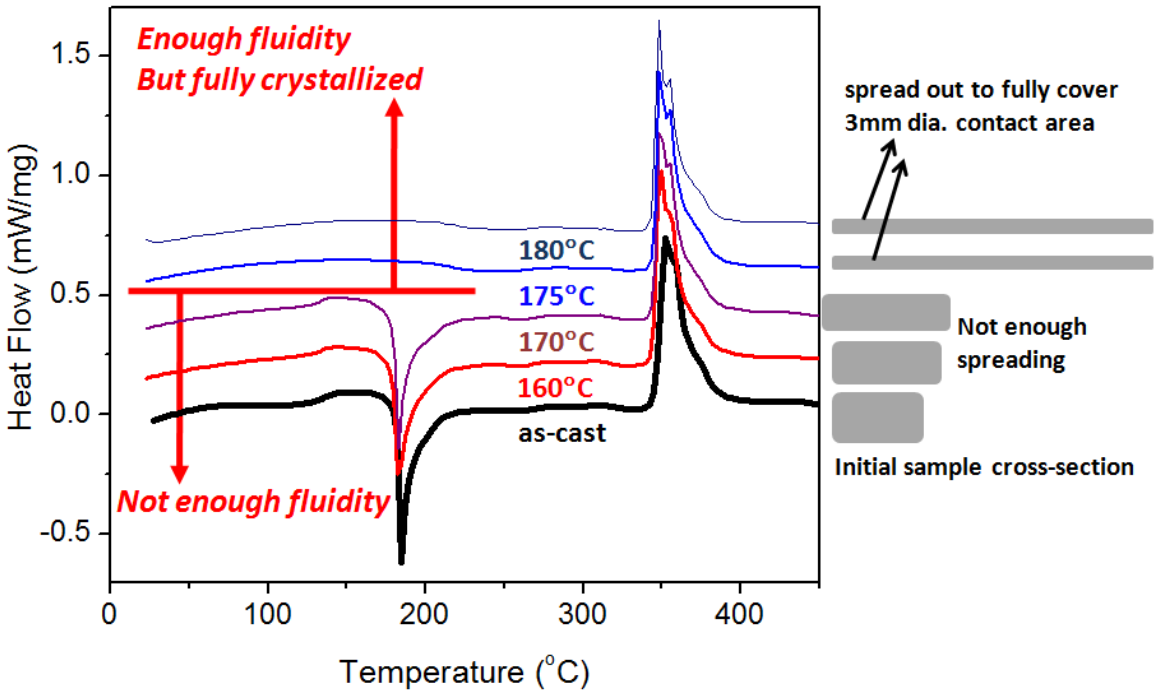

Figure 6-15. DSC scans of the $Au_{48}Ag_{5.5}Pd_{2.3}Cu_{26.9}Si_{16.3}Ti_1$ alloy solder pieces after joining process. Right side of the figure shows cross-sectional shape change of each solder specimen by the process.

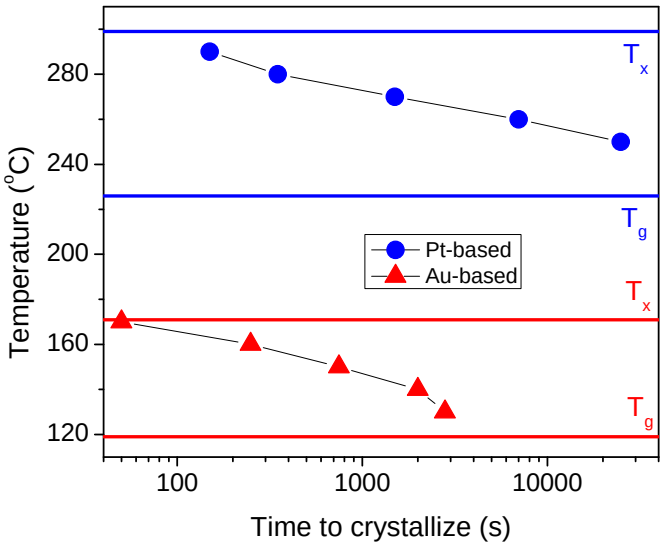

Figure 6-16. Time-temperature-transformation (TTT) diagram of Pt-based and Au-based glasses. Data for Au-based BMG is from Ref. 20 and data for Pt-BMG is from Ref. 21.

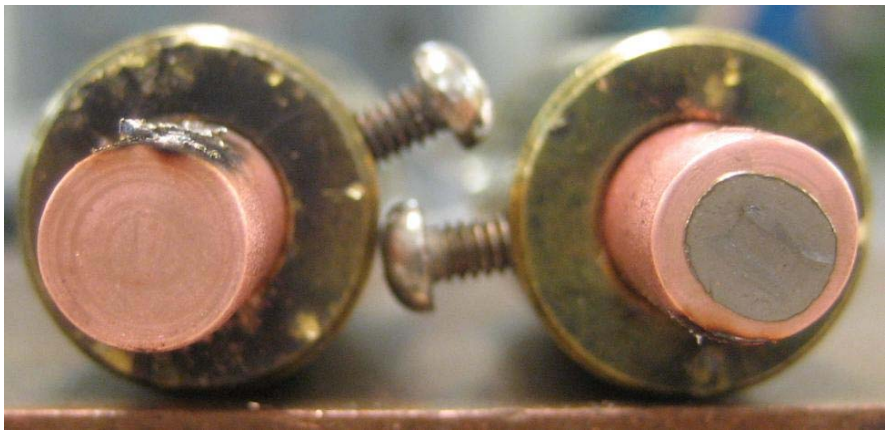

Figure 6-17. La-based BMG joint after tension test (diameter of the copper cylinders is 6.35mm).

Experimental results with Au-, La- and Pt-BMG suggest thermally activated bond formation during atomic configuration rearrangement in the supercooled liquid state. An intimate bond interface between a Pt-BMG and pure copper can be achieved without producing a reaction phase as proven by SEM and TEM work. The bonding mechanism does not appear to require any specific constituent element. Although there is evidence of the diffusion of copper into the Pt-BMG solder, this diffusion process may not be a necessary step; in other words, copper diffusion could be a by-product of the high temperature soldering process, not a crucial process to assist bond interface formation. More study is required to understand the bond forming behavior between pure metal (copper) and BMG.

6.8 Conclusion

In summary, a novel thermoplastic bonding concept was demonstrated using the supercooled liquid region of BMG. With the assistance of a small applied load, the $Pt_{57.5}Cu_{14.7}Ni_{5.3}P_{22.5}$ glassy solder wets a copper surface to form an atomistically-intimate interface. Although there is an evidence of copper diffusion into the Pt-BMG solder by the thermoplastic soldering process, the diffusion is not a necessary condition for bond formation. Fracture of bonding interface proceeds with deformation and subsequent dimple formation of copper. In order to be applicable as a thermoplastic solder, a BMG is required to have a robust glass forming ability and high thermal stability.

Acknowledgements

The authors acknowledge the support from the INTEL Corporation under award No.27940. This work benefited from use of the Caltech KNI and Mat Sci TEM facilities supported by the MRSEC Program of the National Science Foundation under Award Number DMR-0520565.

References

[1] G. Duan, A. Wiest, M.L. Lind, J. Li, W.-K. Rhim and W.L. Johnson, Advan. Mater. 19 (2007) 4272-4275.

[2] J. Schroers, Q. Pham and A. Desai, J. MEMS 16 (2007) 240-247.

[3] T. Laurila, V. Vuorinen and J.K. Kivilahti, Mater. Sci. Eng. R 2005; 49: 1-60.

[4] K. Zeng and K.N. Tu, Mater. Sci. Eng. R 2002; 38: 55-105.

[5] M. Abtew and G. Selvaduray, Mater. Sci. Eng. R 2000; 27: 95-141.

[6] D.W. Kim, D. Suh, T. Millard, H. Kim, C. Kumar, M. Zhu, Y. Xu, Proceedings of IEEE Electronic. Components and Technology Conference 2007; 1614-1619.

[7] D. Suh, C.-w. Hwang, M. Ueshima, J. Sugimoto, Mater. Lett. 2008; 62: 2017-2020.

[8] W.L. Johnson, MRS Bull. 1999; 24(10): 42-56.

[9] F. Ren, J.-W. Nah, K.N. Tu, B. Xiong, L. Xu and J.H.L. Pang, Appl. Phys. Lett. 89 (2006) 141914.

[10] G.Y. Li, B.L. Chen, X.Q. Shi, S.C.K. Wong and Z.F. Wang, Thin Solid Films 504 (2006) 421-425.

[11] J. Schroers and W.L. Johnson, Appl. Phys. Lett. 84 (2004) 3666-3668.

[12] J. Schroers, B. Lohwongwatana, W.L. Johnson and A. Peker, Mater. Sci. Eng. A 449 (2007) 235-238.

[13] G.J. Dienes and H.F. Klemm, J. Appl. Phys. 17 (1946) 458-471.

[14] D. Suh and R.H. Dauskardt, Ann. Chim. Sci. Mat. 27 (2002) 25-40.

[15] X.K. Xi, D.Q. Zhao, M.X. Pan, W.H. Wang, Y. Wu and J.J. Lewandowski, Phys. Rev. Lett. 94 (2005) 125510.

[16] V.H. Stott, Proc. Phys. Soc. 45 (Part1), 530 (1933)

[17] J. Schroers, B. Lohwongwatana, W.L. Johnson and A. Peker, Appl. Phys. Lett. 87 (2005) 061912.

[18] H. Ma, L.L. Shi, J. Xu, Y. Li and E. Ma, Appl. Phys. Lett. 87 (2005) 181915.

[19] H. Tan, Y. Zhang, D. Ma, Y.P. Feng and Y. Li, Acta Mater. 51 (2003) 4551.

[20] Unpublished data of Boonrat Lohwongwatana.

[21] J. Schroers, B. Lohwongwatana, W.L. Johnson and A. Peker, Mat. Sci. Eng. A 449-451 (2007) 235.

Appendix 6-A Coefficient of Thermal Expansion (CTE) of BMG's

Joining two different materials together always accompanies problems caused by the mismatch of Coefficient of Thermal Expansion (CTE). Since the thermoplastic soldering aims microelectronic application, it is required to have knowledge on the CTE of various BMG's to be compared with many other conventional metallic materials. In the Appendix 6-A, the evaluation procedure of CTE of various BMG's are described and discussed.

Thermal expansion measurement is carried out using Perkin Elmer Thermomechanical Analyzer (PE-TMA). Figure 6A-1 is a schematic diagram of the measurement setup. With a probe made of quartz (diameter is 3mm), specimens with diameter larger than that of the quartz probe and with height ranging between 5 and 10 mm are pressed with a small load of 5 or 10 mN. Thermocouple and furnace calibrated with melting of Sn and Pb standard samples surround the specimen and probe. The quartz probe is connected to a Linear Variable Differential Transformer (LVDT) which is calibrated with zero point and 9.36 mm standard sample. Figure 6A-2 shows heating and cooling cycles repeated three times on a high purity copper cylinder with 6.35 mm diameter and 6.09 mm height. Heating and cooling rate is 5 K/min and applied load is 10 mN. Except the first heating curve, all heating and cooling curves are matching, as shown in Figure 6A-2(b). So the five curves except the first heating curve are used for evaluating thermal expansion of each specimen. Derivative of the probe position with temperature is shown in Figure 6A-3. The derivative appears almost constant as temperature increases. With linear fitting of five curves in Figure 6A-2(b), simple estimation of CTE with a reference specimen height at room temperature (25°C) is about 16.5×10^{-6} K^{-1}, which is identical to the known value of pure copper, 16.5×10^{-6} at 25°C [1].

Thermal expansion of various BMG alloys are carried out in the same way. Table 6A-1 and Figure 6A-4 show the linear CTE of various BMG's. Linear CTE's of BMG's are varying

from 9.2 to 19.7×10^{-6} K^{-1} showing large difference between them. Two different Zr-based BMG's have almost identical CTE values. This suggests that thermal expansion of BMG is mainly determined by major alloying element. Indeed, as shown by Table 6A-2 and Figure 6A-5, linear CTE of BMG and major constituting pure metal has a rough linear relationship although there is a difference in how far each alloy deviates from the linear relationship. Also, it is noteworthy that the BMG's thermally expand more than major constituting pure metals.

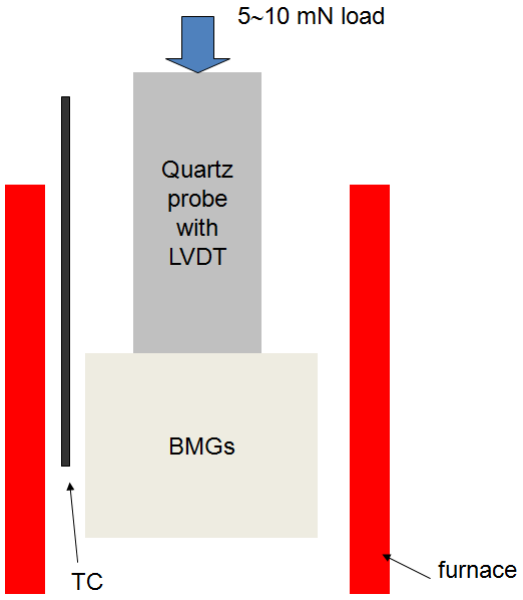

Figure 6A-1. Schematic diagram of CTE measurement setup.

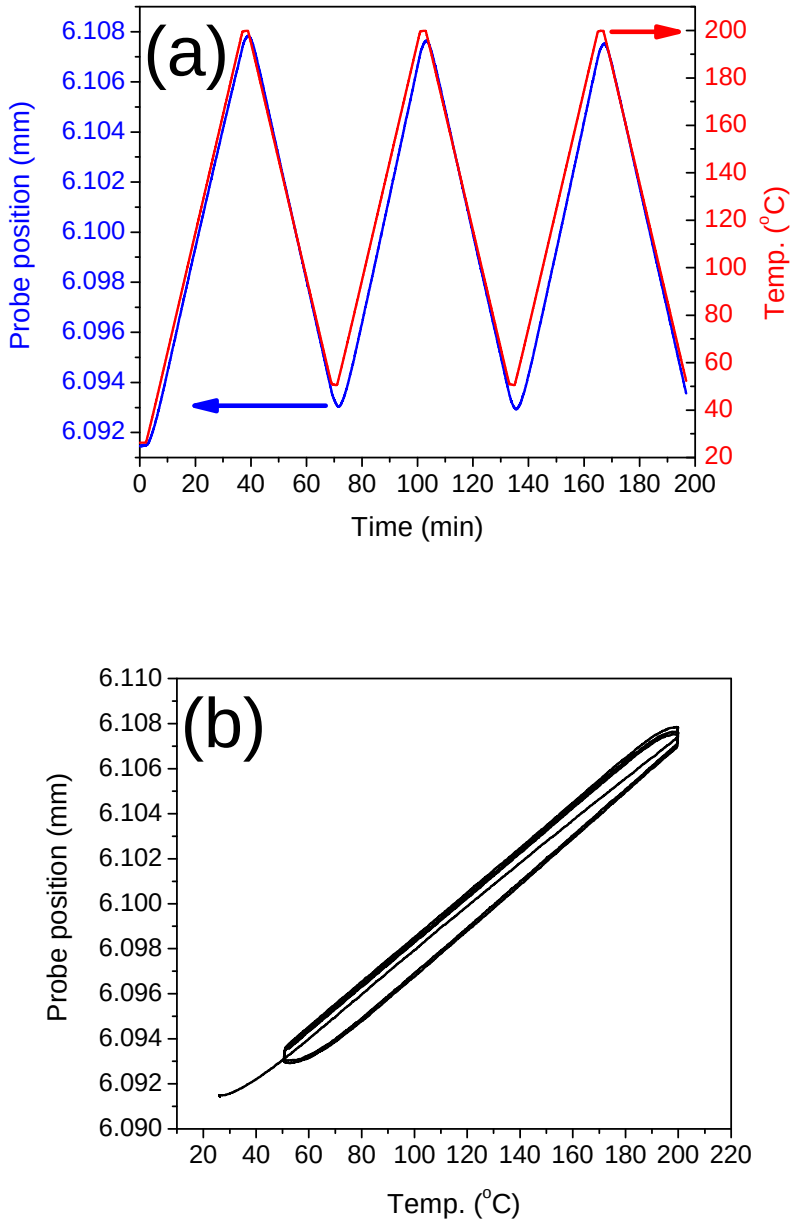

Figure 6A-2. Heating and cooling cycles repeated three times on a high purity copper cylinder with 6.35 mm diameter and 6.09 mm height. (a) Probe position and temperature plotted as a function of time and (b) Probe position as a function of temperature.

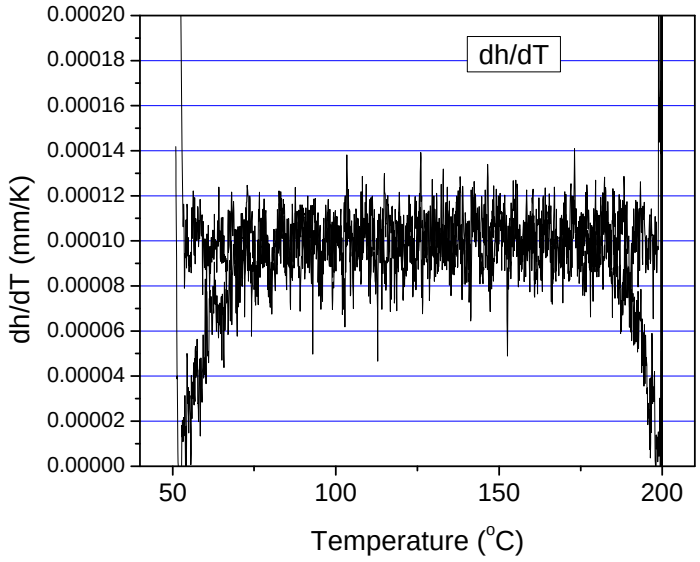

Figure 6A-3. Derivative of probe position by temperature.

Table 6A-1. Linear coefficient of thermal expansion (CTE) of BMG's.

Alloy	Linear CTE (10^{-6} K^{-1})
$Zr_{46.75}Ti_{8.25}Cu_{7.5}Ni_{10}Be_{27.5}$ (Vitreloy 4)	9.2
$Zr_{35}Ti_{30}Cu_{8.25}Be_{26.75}$ (GHDT)	9.3
$Pt_{57.5}Cu_{14.7}Ni_{5.3}P_{22.5}$	10.4
$Pd_{43}Ni_{10}Cu_{27}P_{20}$	14.1
$Au_{49}Ag_{5.5}Pd_{2.3}Cu_{26.9}Si_{16.3}$	19.7

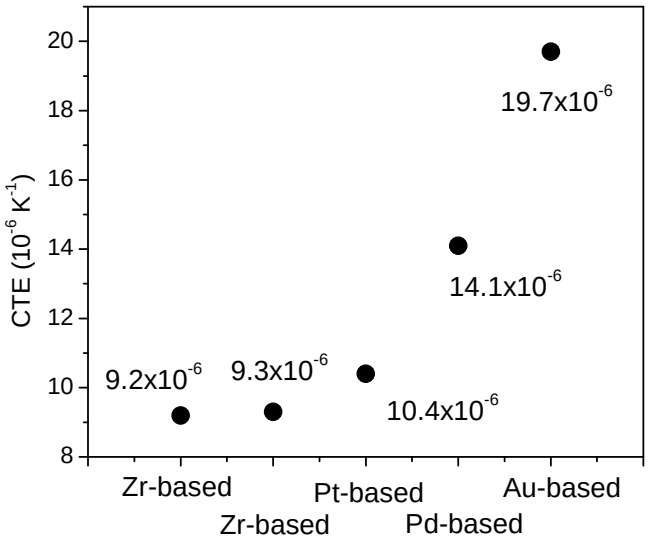

Figure 6A-4. Linear coefficient of thermal expansion (CTE) of BMG's.

Table 6A-2. Linear CTE of pure metals at 25°C [1].

Pure Metal	Linear CTE (10^{-6} K^{-1}) at 25°C
Zr	5.7
Pt	8.8
Pd	11.8
Au	14.2

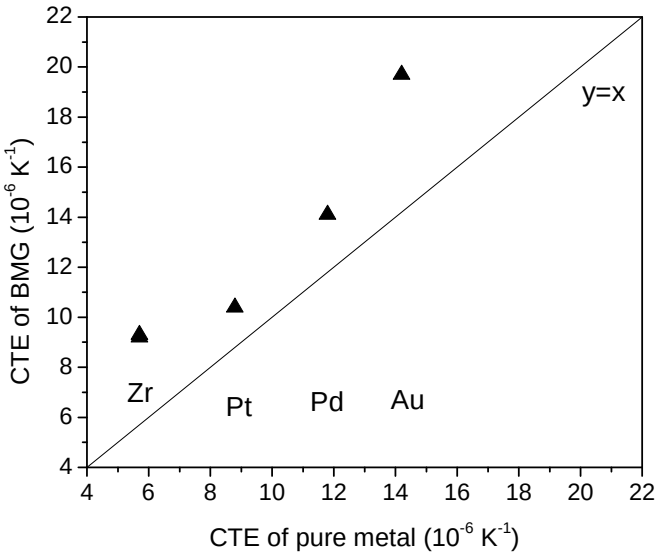

Figure 6A-5. Relationship of CTE's between pure metal and BMG.

Reference for Appendix 6-A

[1] Copper from http://www.wikipedia.org

Appendix 6-B Electrical resistance measurement of BMG's and solder joints

Electrical resistance is used in this chapter as an evaluation parameter on the solder joint interface as shown in Figure 6B-1, because the electrical resistance can provide a sense of how good the interface is as well as the bonding strength does. We can compare the measured resistance value with the ideal resistance of joint calculated by assuming that there is no contact resistance ($R = R_{Cu} + R_{BMG} + R_{Cu}$). In order to evaluate the robustness of a joint, we need to know the electrical resistivity of BMG's first. HP 3468A multimeter and HP 6177 DC current source are used for the typical four point probe setup. A Ni wire with 1mm diameter and 19.5 mm distance between two electrodes for voltage drop measurement is used for verification of the setup. Mean resistance calculated from the data points in Figure 6B-2 is 1.674 mΩ. And the resistivity calculated is $\rho = R\,A/\ell$ =67.4 nΩ·m, which is close to the known value, 69.3 nΩ·m. For a Zr-based BMG (Vitreloy 1, $Zr_{41.2}Ti_{13.8}Cu_{12.5}Ni_{10}Be_{22.5}$), specimen thickness is 2.3 mm and specimen width is 7.88 mm. The distance between two electrodes for voltage drop measurement is 7.7 mm. Mean value for resistance calculated from the data shown in Figure 6B-3 is 0.746 mΩ. And the calculated resistivity is 1756 nΩ·m. In the same way, Pt-based BMG ($Pt_{57.5}Cu_{14.7}Ni_{5.3}P_{22.5}$, 2.32 mm thick × 8.07 mm wide, 6.0 mm distance between two electrodes) has 0.592 mΩ of resistance. Calculated resistivity is 1850 nΩ·m, which is not much different from that of Vitreloy 1.

For the joint shown in Figure 6-3(b-2) and 6-9, the thickness of the squeezed Pt-BMG solder is estimated to be 53 μm in Table 6-1. Actual thickness measured from Figure 6-9 ranges from 46 to 61 μm, having average of about 50 μm at central area. As shown in Figure 6-9, the actual contact area appears almost same as the designed 'contact zone' area. Thus, it looks reasonable to assume the contact area is 7.065 mm^2. Inner probe distance is about 5 mm. Resistance calculated using resistivity of Pt-BMG, 1850 nΩ·m, is 13.1 μΩ. With the contribution

of copper substrate estimated to be around 2.7 μΩ, the total resistance of the joint is 15.8 μΩ. Since there could be a decrease of resistivity of Pt-BMG by partial crystallization, this calculation is likely to underestimate the ideal resistance of the joint. However, the proximity of the measured electrical resistance, 14.7 μΩ, and estimated value, 15.8 μΩ, implies that the formed bonding interface between copper and Pt-BMG has strong intimacy.

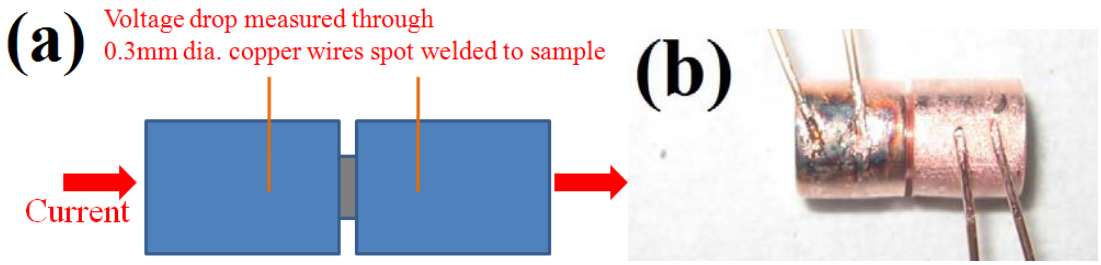

Figure 6B-1. (a) Schematic diagram of electrical resistance measurement performed in this chapter and (b) actual specimen setup.

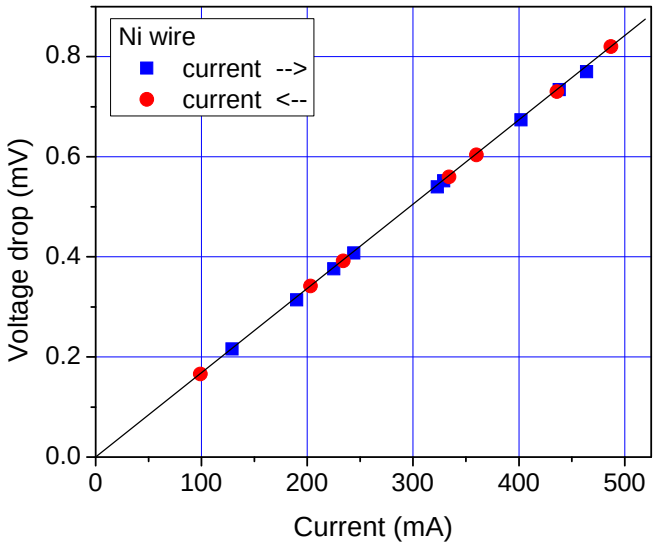

Figure 6B-2. Electrical resistance (Voltage drop) measurement for a Ni wire for verification.

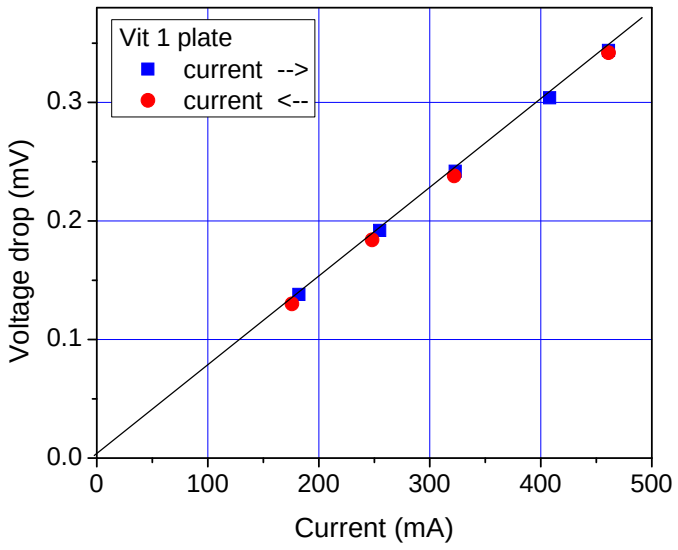

Figure 6B-3. Electrical resistance (Voltage drop) measurement for a Vitreloy 1 plate.

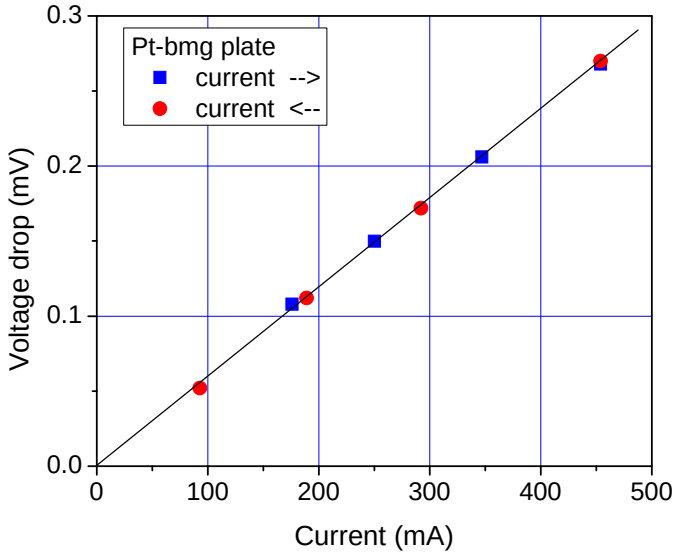

Figure 6B-4. Electrical resistance (Voltage drop) measurement for a Pt-BMG plate.